

JEEES

Journal of
Electromagnetic
Engineering and
Science

ISSN 2671-7255 (print)
ISSN 2671-7263 (online)

<http://www.jees.kr>

Volume 22, No. 5
September 2022

KIEES



JEEES Journal of Electromagnetic Engineering and Science

EDITOR-IN-CHIEF

Jungsuek, Oh (Seoul Nat'l University, Korea)
e-mail : jungsuek@snu.ac.kr

ASSOCIATE EDITORS

Nader Behdad (University of Wisconsin, Madison, USA)
Gangil Byun (UNIST, Korea)
Sangjo Choi (University of Ulsan, Korea)
Jae-Young Chung
(Seoul Nat'l University of Science and Technology, Korea)
Sun Hong (Soongsil University, Korea)
Kyung-Young Jung (Hanyang University, Korea)
Jae Hee Kim (KOREA TECH, Korea)
Jingook Kim (UNIST, Korea)
Youngwook Kim (Sogang University, Korea)
Haeng-Seon Lee (Sogang University, Korea)
Sungho Lee (Korea Electronics Technology Institute, Korea)
Yongshik Lee (Yonsei University, Korea)
Sungjoon Lim (Chung-Ang University, Korea)
Youngcheol Park (Hankuk University of Foreign Studies, Korea)
Kunio Sakakibara (Nagoya Institute of Technology, Japan)
Eakhwan Song (Kwangwoon University, Korea)
Sang-Hyuk Wi (Samsung Research, Korea)
Youngoo Yang (Sungkyunkwan University, Korea)
Ick-Jae Yoon (Chungnam Nat'l University, Korea)
Jong Won Yu (KAIST, Korea)

INTERNATIONAL ADVISORY BOARD

Ikuo Awai (Ryutech Corporation, Japan)
Bumman Kim (POSTECH, Korea)
Dong Chul Park (Chungnam Nat'l University, Korea)
John Volakis (Ohio State University, USA)
Huei Wang (National Taiwan University, Taiwan)
Robert Weigel
(Friedrich-Alexander-Universität, Erlangen-Nürnberg, Germany)
Ke Wu (Polytechnique Montréal, Canada)
Richard Ziolkowski (University of Arizona, USA)

EDITOR MEMBERS

ANTENNAS

Andrey K. Sarychev
(Moscow Institute of Physics and Technology, Russia)
Bierng-Chearl Ahn (Chungbuk Nat'l University, Korea)
Gyu-Je Sung (Hankyong Nat'l University, Korea)

Hae-Won Son (Chonbuk Nat'l University, Korea)
Junho Yeo (Daegu University, Korea)

PASSIVE COMPONENTS AND CIRCUITS

Dal Ahn (Soonchunhyang University, Korea)
Juseop Lee (Korea University, Korea)
Kang Wook Kim (Kyungpook Nat'l University, Korea)
Truong Vu Bang Giang (Vietnam National University, Vietnam)
Cheng-Wei Qiu (National University of Singapore)

ACTIVE DEVICES AND DEVICE MODELING

Kris Kong (TriQuint Semiconductor, USA)
Shigeo Kawasaki (Japan Aerospace Exploration Agency, Japan)
Kyung Whan Yeom (Chungnam Nat'l University, Korea)
Tae-Yeoul Yun (Hanyang University, Korea)
Chan-Wang Park (Université du Québec à Rimouski, Canada)

RF/WIRELESS SYSTEM AND APPLICATIONS

Chun Sik Chae (NASA Jet Propulsion Laboratory, USA)
Pavel Nikitin (Intermec Technologies Corporation, USA)
Joong-Soo Lim (Baekseok University, Korea)
Sang-Min Han (Soonchunhyang University, Korea)
Seung Yeop Rhee (Chonnam Nat'l University, Korea)

THEORY AND NUMERICAL METHODS

Jay Kyoong Lee (Syracuse University, USA)
Seung-Yeup Hyun (Jeju Nat'l University, Korea)
Yong-Heui Cho (Mokwon University, Korea)

ELECTROMAGNETIC INTERFERENCE/ COMPATIBILITY/ENVIRONMENT/MEASUREMENT

Tzong-Lin Wu (National Taiwan University, Taiwan)
Ic-Pyo Hong (Kongju Nat'l University, Korea)
Jae-Yong Kwon (KRISS, Korea)
Seungyoung Ahn (KAIST, Korea)
Tae Weon Kang (KRISS, Korea)

ETHICAL EDITOR

Dongho Kim (Sejong University, Korea)

STATISTICAL EDITOR

Youngje Sung (Kyonggi University, Korea)

MANUSCRIPT EDITOR

Il-Suek Koh (Inha University, Korea)

Aims and Scope

The Journal of Electromagnetic Engineering and Science (JEES) is an official English-language journal of the Korean Institute of Electromagnetic and Science (KIEES). This journal was launched in 2001 and has been published quarterly since 2003. It is currently registered with the National Research Foundation of Korea and also indexed in Scopus, CrossRef, EBSCO, DOI/Crossref, Google Scholar, and Web of Science Core Collection as Science Citation Index Expanded (SCIE) journal. The objective of JEES is to publish academic as well as industrial research results and discoveries in electromagnetic engineering and science. The particular scope of the journal includes electromagnetic field theory and its applications; high frequency components, circuits, and systems; antennas; electromagnetic wave environments; and relevant industrial developments. In addition to the regular stream of contributed papers, the journal occasionally publishes special issues on specific topics of current interest, to promote a focused coverage of the selected topics. In addition, JEES regularly posts invited review papers by leading researchers in the relevant fields, which will provide an overview of various subjects from their own perspectives. The editors of JEES are aware of the importance of rapid publication for the delivery of new research results to its readers with minimum delay, and fully recognize the need for a short turnaround time. Manuscripts submitted to JEES take about 3–5 months from the initial submission to publication. This rapid process applies to all three types of manuscripts that JEES publishes: regular papers, letters, and invited papers. The publication of submitted manuscripts is subject to blind peer review, and the final decision by the Editor-in-Chief is regularly made based on three reviews from experts in the relevant area. This journal actively promotes research in electromagnetic wave-related engineering and sciences, and its ultimate aim is to benefit the global electromagnetic engineering and science community.

Subscription Information

JEES is published bimonthly in January, March, May, July, September, and November. Full text PDF files are available at the official website (<http://www.jees.kr>).

The annual subscription rates for this journal are USD 230 for organization members, USD 55 for Full members, USD 37 for associate members, and USD 28 for student members.

Published by
The Korean Institute of
Electromagnetic Engineering and Science

#706 Totoo Valley, 217 Saechang-ro, Yongsan-gu, Seoul,
04376, Korea
Tel : +82-2-337-9666
Fax : +82-2-6390-7550
<https://www.kiees.or.kr>
E-mail : kees@kiees.or.kr

Printed September 25, 2022
Published September 30, 2022

Printed by
Guhmok Publishing Company / Guhmok Info
Tel : +82-2-2277-3324
Fax : +82-2-2277-3390
E-mail : guhmok@guhmok.com

This is an Open-Access article distributed under the terms of the Creative Commons Attribution Non-Commercial License (<http://creativecommons.org/licenses/by-nc/4.0>) which permits unrestricted non-commercial use, distribution, and reproduction in any medium, provided the original work is properly cited.

@This paper meets the requirements of KS X ISO 9706, ISO 9706-1994 and ANSI/NISO Z.39.48-1992 (Permanence of Paper).

©Copyright The Korean Institute of Electromagnetic Engineering and Science.

 KOFST

This journal was supported by the Korean Federation of Science and Technology Societies Grant funded by the Korean Government (Ministry of Education).

REGULAR PAPERS

Conical Ground Helical Antenna with Feed-Through Insulator for High-Power Microwave Applications Seung Hun Cha · Jin Soo Choi · Jiheon Ryu · Hae-ok Kwon · Sang-min Lee · Dong-Hee Son · Young Joong Yoon	537
Development of a Numerical Tablet Model in WLAN Band for SAR Study Jisu Lee · Ae-Kyoung Lee · Seon-Eui Hong · Hyung-Do Choi · Kyung-Young Jung	544
A Wideband Doherty Combiner with Phase Variation Compensation Using LTCC Applicable for High Power Transmission Youna Jang · Kwanhun Jeong · Jiwon Kim · Daeung Lee · Dal Ahn	550
Free-Space Unknown Thru Measurement Using Planar Offset Short for Material Characterization Jin-Seob Kang	555
Reduced-Size Series-Fed Two-Dipole Endfire Antenna Heesu Wang · Yong Bae Park · Ikmo Park	563
Omega-K Algorithm Using Plane Wave Approximation for Forward-Looking Imaging Radar Byunglae Cho · Sungwon Hong · Kichul Yoon	571
A Neural Network-Based Microwave Imaging Method for Object Localization Wonhyung Son · Won-Kwang Park · Seong-Ho Son	576
Spatial Delay Line Canceler-Based Sidelobe Blanking for Low Radar-Cross-Section Target Youn-Hui Jang · Donghyeon Cho	580
GPR Image Recovery Effect on Faster R-CNN-Based Buried Target Detection Deniz Kumlu	591
A Compact Dual-Band MIMO Antenna for Sub-6 GHz 5G Terminals Guiting Dong · Jianlin Huang · Simin Lin · Zhizhou Chen · Gui Liu	599

Conical Ground Helical Antenna with Feed-Through Insulator for High-Power Microwave Applications

Seung Hun Cha¹ · Jin Soo Choi² · Jiheon Ryu² · Hae-ok Kwon³ · Sang-min Lee³ ·
Dong-Hee Son³ · Young Joong Yoon^{1,*}

Abstract

In this paper, a novel helical antenna for high-power microwave is proposed. The proposed antenna is intended to demonstrate improved power handling capacity without any deterioration in matching characteristics, gain, and axial ratio. The proposed antenna with a long helix structure is investigated in order to achieve high gain and a relatively wide impedance bandwidth. By increasing the distance between the helix and the ground plane, an improved power handling capacity is obtained, and the impedance matching problem caused by the proposed method is addressed with the use of a feed-through insulator. In addition, a conical-shaped ground is used to compensate for the gain reduction by increasing the distance between the helix and the ground plane. As a result, the proposed antenna exhibits a gain exceeding 11 dBi and an axial ratio of less than 2 dB within the frequency range of 0.86–1.09 GHz. In addition, its power handling capacity exceeds 50 MW for a 0.7-ns input pulse length in air conditions.

Key Words: Circular Polarization, Helical Antenna, High-Power Microwaves.

I. INTRODUCTION

In recent years, there has been an increasing demand for high-power microwave (HPM) systems and antennas capable of transmitting gigawatt-level power. Various types of antennas for HPM systems, such as impulse radiating antenna (IRA) [1], radial line slot antenna [2], TEM horn antenna [3], and helical antenna [4–7], have been described in the literature. Helical antennas are widely used in HPM systems owing to their advantages, including their compact structure, simple radiating circularly polarized wave, and wide bandwidth. The most important consideration in designing an antenna suitable for

HPM applications is its increased power handling capacity, which can be achieved in two ways. The first method aims to improve the critical electric field strength with the use of an SF₆ gas or a vacuum pump [4–6]. The second method aims to reduce the maximum E-field on the antenna through the modification of the antenna structure [6, 7]. In [6], the E-field reduction method involving branching the helix radiator is proposed. However, such an antenna has a narrow impedance bandwidth due to the branched wire. In [7], in order to reduce the maximum E-field, the wire at the feed point is smoothly bent, and the diameter increases gradually. However, additional methods are needed to further reduce the maximum E-field in recently

Manuscript received July 15, 2021 ; Revised April 13, 2022 ; Accepted July 21, 2022. (ID No. 20210715-080J)

¹Department of Electrical and Electronic Engineering, Yonsei University, Seoul, Korea.

²The 4th Research and Development Institute, Agency for Defense Development, Daejeon, Korea.

³Development Team 3, Hanwha Corporation, Gumi, Korea.

*Corresponding Author: Young Joong Yoon (e-mail: yjyoon@yonsei.ac.kr)

This is an Open-Access article distributed under the terms of the Creative Commons Attribution Non-Commercial License (<http://creativecommons.org/licenses/by-nc/4.0>) which permits unrestricted non-commercial use, distribution, and reproduction in any medium, provided the original work is properly cited.

© Copyright The Korean Institute of Electromagnetic Engineering and Science.

developed high power sources. In this paper, a design technique for improving the antenna power handling capacity based on the method described in [7] with additional modification of the feeding structure is proposed. To reduce the E-field on the helical antenna, the wire diameter is extremely increased, and the height of the connecting part is extended. Accordingly, this approach causes an impedance mismatch because the connecting part between the coax waveguide and the helix radiator cannot operate as an impedance transformer. Consequently, the matching method with a feed-through insulator is proposed for helical antennas with extremely large wire diameters. The proposed antenna is verified with respect to its gain and matching characteristics by performing low-power tests. Its power handling capacity is also investigated by performing high-power tests.

II. ANTENNA DESIGN

1. Power Handling Capacity of Conventional Helical Antenna

The geometry of the conventional helical antenna is presented in Fig. 1(a). The configuration of the helical antenna can be divided into four sections. Section A consists of an RG-218 coaxial cable. Section B consists of a coaxial waveguide filled with a dielectric (PET-100, $\epsilon_r = 2.9$). Section C consists of a horizontal wire conductor over the ground plane, which operates as a quarter-wave transformer with a characteristic impedance of 75Ω . Section D consists of the helix defined by the pitch angle and diameter.

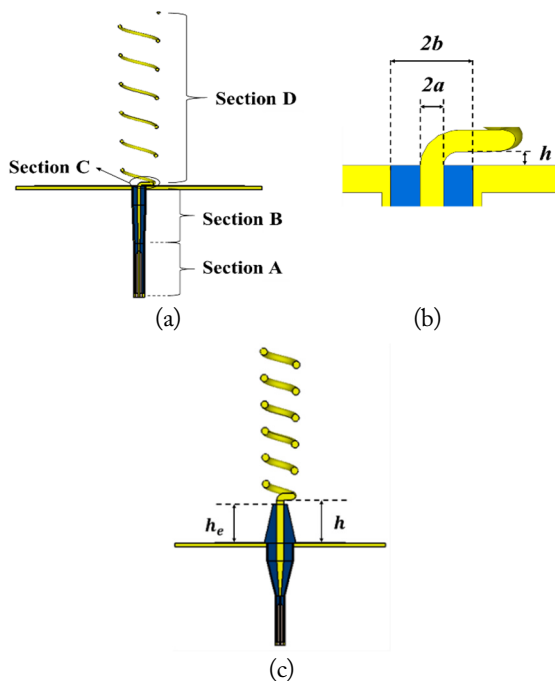


Fig. 1. Geometry of the helical antenna: (a) conventional helical antenna, (b) connecting part of the conventional helical antenna, and (c) proposed helical antenna with a feed-through insulator.

For HPM applications, the electric field strength should be taken into account to avoid electrical breakdown in each section. The E-field can be reduced if the wire of the helix is made of a thick copper tube [5]. However, as the wire diameter becomes thicker, the input impedance of the helical antenna decreases [8]. Thus, the wire diameter of a helical antenna designed for HPM applications is typically about $0.005\text{--}0.05\lambda$ [8]. The simulated maximum E-field of the conventional helical antenna for various wire diameters and distances (b) between the ground and the helix is presented in Fig. 2, for an input power of 0.5 W. As the wire diameter and the distance between the ground and the helix increases, the maximum E-field decreases, as shown in Fig. 2.

The relationship between the maximum E-field and the power handling capacity of the antenna is

$$P (W) = (E_b/E_{Max@0.5W})^2/2, \quad (1)$$

where, P is power handling capacity, E_b is critical peak electric field strength (3 MV/m for continuous wave), and $E_{Max@0.5W}$ is maximum E-field on antenna when the input power is 0.5 W. According to Eq. (1) and to the simulated maximum E-field in Fig. 2, the power handling capacity of the conventional helical antenna is improved by extending the distance between the ground and the helix.

The input impedance of the conventional helical antenna for various wire diameters is presented in Fig. 3. As the wire diameter increases, reducing the maximum E-field, the impedance bandwidth is restricted by the cutoff frequency of the coaxial waveguide in section B. Also, the horizontal wire conductor in section C can no longer operate as a quarter-wave transformer due to the enlarged dielectric of section B in order to maintain a $50\text{-}\Omega$ characteristic impedance of the coaxial waveguide. Therefore, the wire diameter is chosen to be $2a = 20$ mm for a wide input impedance bandwidth and relatively low E-field intensity. The input impedance of the conventional helical antenna for different b , when $2a = 20$ mm, is presented in Fig. 4. As b increases, the reactance becomes capacitive, although the input

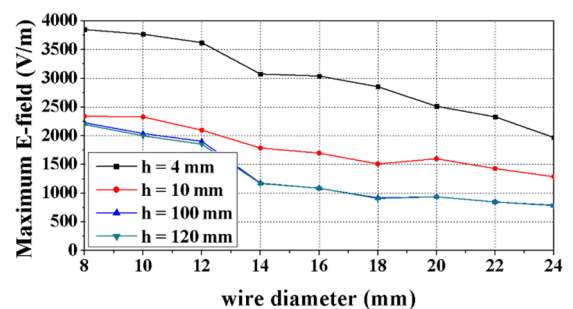
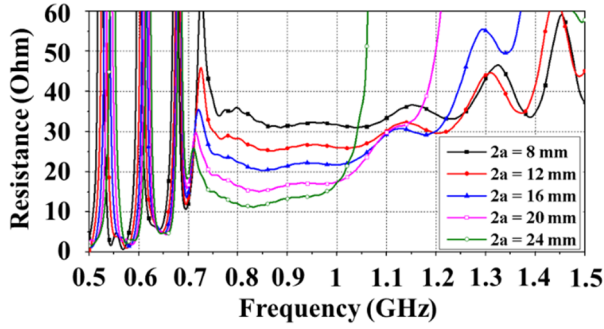
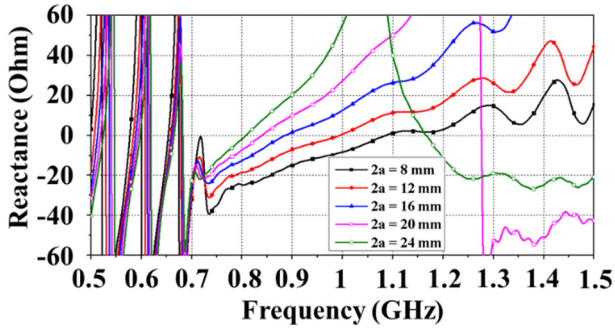


Fig. 2. Maximum E-field of the conventional helical antenna for different wire diameters ($2a$) and distances (b) between the ground and the helix.



(a)



(b)

Fig. 3. Input impedance of the conventional helical antenna for different wire diameters when $h = 4$ mm: (a) resistance and (b) reactance.

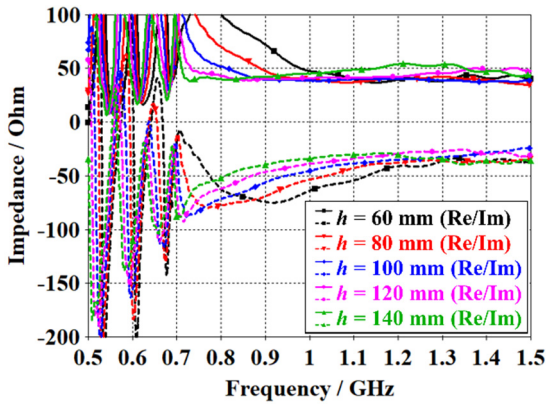


Fig. 4. Input impedance of the conventional helical antenna for different h values when $2a = 20$ mm.

resistance is saturated to 50Ω .

Therefore, to provide better impedance matching to the helical antenna, the capacitive reactance must be compensated by modifying the feeding structure.

2. Helical Antenna with a Feed-Through Insulator

To compensate for the capacitive reactance of the helical antenna, a conical-shaped feed-through insulator (HAFI) is proposed, as shown in Fig. 1(c). The feed-through insulator is extended from the dielectric (PET-100) of the coaxial waveguide of section B, with a height of h_e . The E-field distribution and the equivalent circuit of the HAFI are presented in Fig. 5.

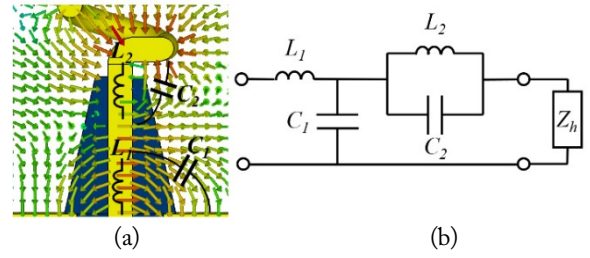


Fig. 5. (a) E-field distribution and (b) equivalent circuit of the HAFI.

C_1 is the shunt capacitance between the vertical wire and the ground plane. C_2 is the parasitic capacitance between the vertical wire and the horizontal wire. L_1 and L_2 are the inductances corresponding to the length of the vertical wire. As the height of the insulator (h_e) increases, the shunt capacitance (C_1) and the parasitic capacitance (C_2) also increase. Similarly, the effective length of the vertical wire section increases.

The input impedance of the HAFI for different insulator heights (h_e) is presented in Fig. 6. The distance between the ground and the helix is 120 mm. As h_e increases, the input resistance decreases until $h_e = 50$ mm, because C_1 is the dominant parameter. Then, the input resistance increases due to the increase in C_2 , as presented in Fig. 6. The input reactance also increases due to the increase in C_2 and due to the vertical wire electrical length. Therefore, the impedance bandwidth is enlarged to a lower frequency band, as presented in Fig. 7. The insulator height is set at 110 mm.

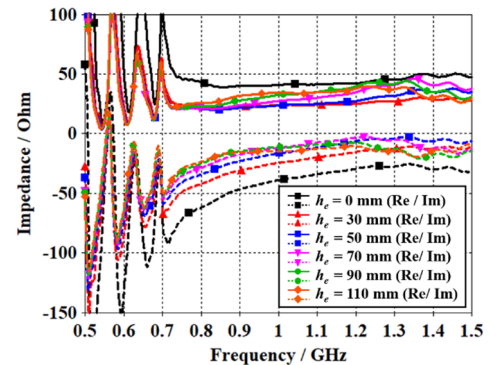


Fig. 6. Input impedance of the HAFI for different insulator heights.

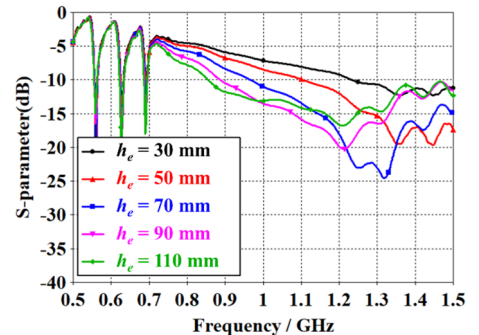


Fig. 7. S-parameter of the HAFI for different insulator heights.

The E-field distributions of the conventional helical antenna and of the HAFI are presented in Fig. 8. The maximum E-field occurs at the horizontal wire conductor, and the corresponding values are 2990 V/m and 942 V/m. Hence, in air conditions, the power handling capacity for each antenna type is calculated from the equation given in [6], that is, $(E_i/2990)^2 = 1 \text{ MW}$ and $(E_i/942)^2 = 10 \text{ MW}$, respectively. Thus, the power handling capacity is improved by 10 times.

3. Gain Compensation with Ground Modification

Due to the increased height of the helix from the ground plane, a phase difference between the radiated field in the forward direction and the field reflected by the ground plane is generated. Therefore, the side-lobe level increases, and the gain of the HAFI is 1.4 dB lower than that of the conventional helical antenna, as shown in Fig. 9. To improve the gain of the HAFI, the ground plane is modified into a conical shape, as shown in

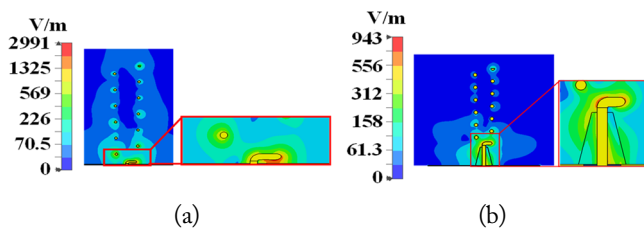


Fig. 8. E-field distribution: (a) conventional helical antenna and (b) HAFI.

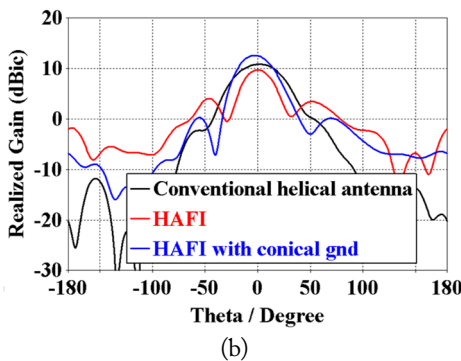
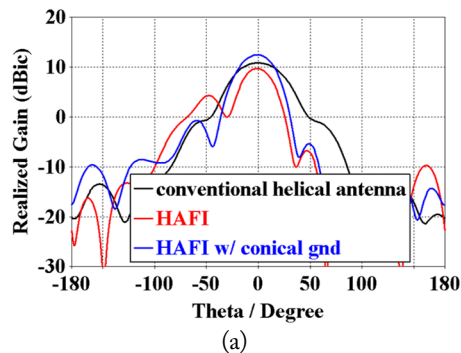


Fig. 9. Radiation pattern of helical antennas at 1 GHz: (a) $\phi = 0^\circ$ and (b) $\phi = 90^\circ$.

Fig. 10(a). The slope of the conical ground is 45° , and its height is h_c . The gain of the HAFI with a conical ground for a different h_c is presented in Fig. 11, which shows that the gain increases with the increase in h_c . The maximum gain of the proposed antenna is 12.8 dBic for $h_c = 60 \text{ mm}$, as presented in Fig. 9. The gain of the HAFI with a conical ground is enhanced by 3.2 dB compared with that of the HAFI. This is due to the reduction in the side-lobe level. Meanwhile, the simulated maximum E-field is 1253 V/m, which is higher than that of the HAFI with planar ground. This is because the E-field reflected by the conical ground is concentrated on the horizontal wire. The E-field distribution of the HAFI with a conical ground is presented in Fig. 12. Thus, the power handling capacity for air propagating a

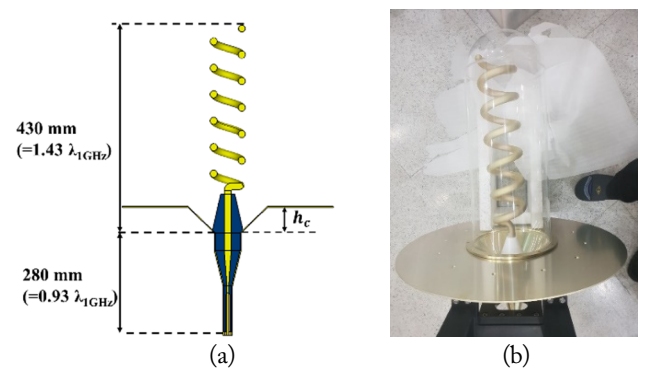


Fig. 10. Geometry of the proposed antenna: (a) HAFI with a conical ground and (b) the fabricated proposed antenna.

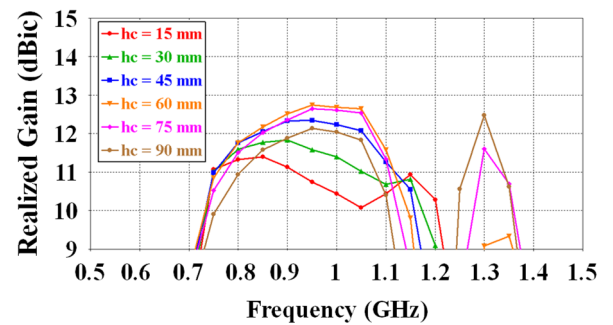


Fig. 11. Gain of the HAFI with a conical ground for different conical ground heights.

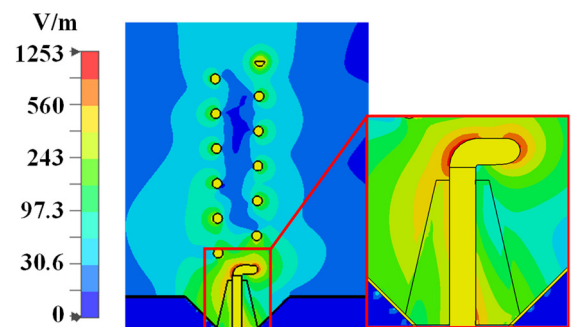


Fig. 12. E-field distribution of the HAFI with a conical ground.

continuous wave is $(E_b/1253)^2 = 5.74$ MW. This result shows that the power handling capacity is improved by 5.74 times compared with that of the conventional helical antenna and is higher than that reported in [6], which is 4.96 times that of the conventional antenna. Moreover, the antenna in [6] has a narrower impedance bandwidth (15.2%) than ours (0.86–1.09 GHz, approximately 23.5%), because the proposed method is applicable only to short helical antennas. In addition, the proposed antenna can be adapted for a longer helix, resulting in a high gain.

When the pulse generator is used as a source of high power, the power handling capacity can be determined by Eq. (1) and by the critical peak electric field strength. The critical peak electric field strength can be calculated from the equation in [9]:

$$\begin{aligned} E_{b,peak} &= \sqrt{2}E_{b,RMS} \\ &= \sqrt{2} \times 22.4 \times p \times \left(1 + \frac{4 \times 10^{-2}}{p \tau_p}\right)^{3/16} \end{aligned} \quad (2)$$

where p is the ambient pressure ($\sim 10^5$ Pa) and τ_p is the duration of the pulse. Given that the input pulse with a 0.7-ns pulse length is used to verify the power handling capacity of the proposed antenna, the critical peak electric field strength is 10.53 MV/m. Therefore, the recalculated power handling capacities of the conventional helical antenna and the proposed antenna are $(E_b/2990)^2 = (10.53 \times 10^6/2990)^2 = 12.4$ MW and $(E_b/1253)^2 = (10.53 \times 10^6/1253)^2 = 70$ MW, respectively.

III. RESULT

To verify the operation of the proposed antenna, experimental measurements were performed by conducting both low-power and high-power tests. The geometrical parameters of the fabricated proposed antenna are shown in Fig. 10(a).

1. Low-Power Test

The measurement results for the S -parameter of the proposed HAFI with a conical ground are presented in Fig. 13. The measured impedance bandwidth falls within the frequency

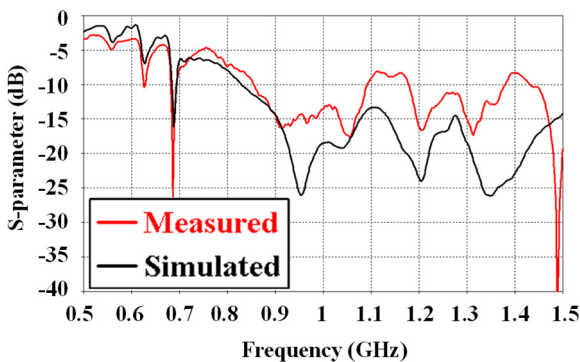


Fig. 13. Simulated and measured S -parameter of the proposed antenna.

range of 0.86–1.09 GHz. The gain and the axial ratio measured in an anechoic chamber are presented in Fig. 14. The measured gain exceeds 11 dBic within the frequency range of operation. The reduction of the measured gain is due to misalignment during the measurement. The measured axial ratio is less than 2 dB within the operating frequency range. Meanwhile, the proposed antenna radiates in near-circular polarization. Thus, the proposed antenna radiates in near-circular polarization.

2. High-Power Test

The power handling capacity of the proposed antenna is verified by a high-power test, the setup for which is presented in Fig. 15. An FPG-P pulse generator (FID GmbH, Burbach, Germany) is used to excite the proposed antenna. The waveform of the output pulse generated by the pulse generator is presented in Fig. 16. This pulse is used as the input pulse of the proposed antenna. The pulse radiated by the proposed helical antenna is measured by vertically and horizontally oriented D-dot sensors in the far-field region. The results, along with the simulation results, are shown in Fig. 16.

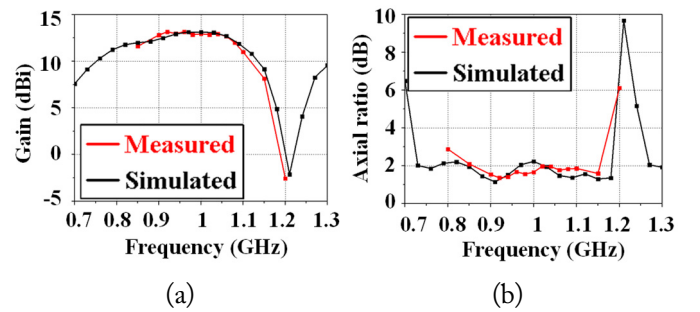


Fig. 14. Simulated and measured (a) gain and (b) axial ratio.

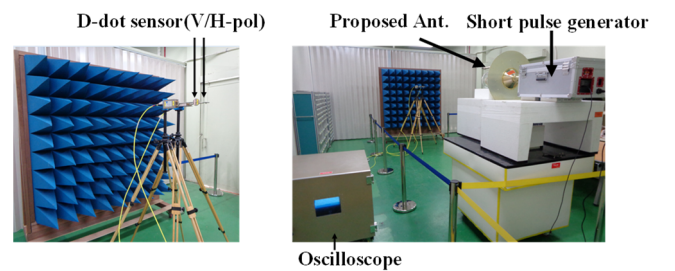


Fig. 15. High-power test setup.

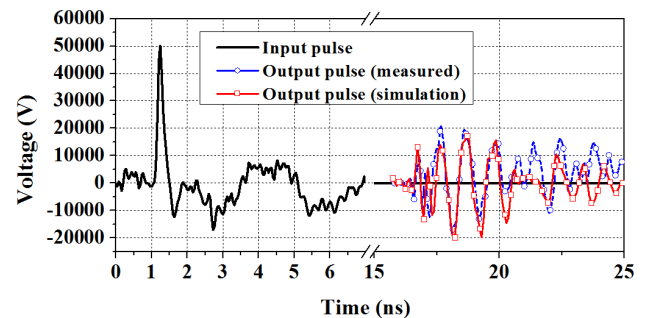


Fig. 16. Waveform of the input and output pulse.

The peak voltage of the input pulse is 50 kV, and the pulse length is 0.7 ns. Thus, the peak power of the input pulse is $(V_p^2/R_{in}) = ((5 \times 10^4)^2/50) = 50$ MW. This input power is sufficient to verify the improvement in power handling capacity, given that this value is larger than the power handling capacity of the conventional helical antenna. The simulation and measured radiated pulses for a 0.7-ns pulse width are well matched, as shown in Fig. 16. Thus, the proposed helical antenna is capable of radiating a high-power short pulse without breaking down and without pulse shortening.

IV. CONCLUSION

A conical ground helical antenna with a feed-through insulator suitable for HPM application is proposed in this paper. The power handling capacity of the proposed antenna is improved by 5.7 times that of the conventional helical antenna. This is achieved by modifying the feeding section. Moreover, the gain of the proposed antenna is improved by modifying the ground plane structure. Additionally, the low- and high-power tests verified that the proposed antenna exhibits a higher power handling capacity and a higher gain than the conventional helical antenna. Therefore, it is suitable for HPM applications.

REFERENCES

- [1] F. Vega and F. Rachidi, "A simple formula expressing the fields on the aperture of an impulse radiating antenna fed by TEM coplanar plates," *IEEE Transactions on Antennas and Propagation*, vol. 66, no. 3, pp. 1549-1552, 2018.
- [2] C. W. Yuan, S. R. Peng, T. Shu, Z. Q. Li, and H. Wang, "Designs and experiments of a novel radial line slot antenna for high-power microwave application," *IEEE Transactions on Antennas and Propagation*, vol. 61, no. 10, pp. 4940-4946, 2013.
- [3] S. Petkar, S. B. Umbarkar, F. Kazi, and N. M. Singh, "Modeling of a high power microwave (HPM) source using 300 kV Marx generator and horn type antenna," *Indian Journal of Science and Technology*, vol. 10, article no. 17, 2017. <https://doi.org/10.17485/ijst/2017/v10i17/111402>
- [4] J. S. Tyo, M. C. Skipper, M. D. Abdalla, J. M. Martin, "Compact, backward-radiating helical antenna for meso-band high-power applications," *IEEE Antennas and Wireless Propagation Letters*, vol. 16, pp. 1699-1702, 2017.
- [5] Y. A. Andreev, A. M. Efremov, V. I. Koshelev, B. M. Kovalchuk, A. A. Petkun, K. N. Sukhushin, and M. Y. Zorkaltseva, "A source of high-power pulses of elliptically polarized ultrawideband radiation," *Review of Scientific Instruments*, vol. 85, no. 10, article no. 104703, 2014. <https://doi.org/10.1063/1.4897167>
- [6] Y. Liang, J. Zhang, Q. Liu, and X. Li, "High-power dual-branch helical antenna," *IEEE Antennas and Wireless Propagation Letters*, vol. 17, no. 3, pp. 472-475, 2018.
- [7] J. R. Mayes, M. G. Mayes, W. C. Nunnally, and C. W. Hatfield, "Helical antennas for high powered RF," in *Proceedings of 2009 IEEE Pulsed Power Conference*, Washington, DC, 2009, pp. 484-488.
- [8] J. D. Kraus and R. J. Marhefka, *Antenna: For All Applications*. New York, NY: McGraw-Hill, 2002.
- [9] A. Larsson, B. Johansson, and S. E. Nyholm, "Radiated electric field strength from high-power microwave systems," *IEEE Transactions on Electromagnetic Compatibility*, vol. 50, no. 3, pp. 758-761, 2008.

Seung Hun Cha



received his B.S. in electrical and electronic engineering from Yonsei University, Seoul, Korea, in 2015. He is currently pursuing an integrated M.S. and Ph.D. degree in electrical and electronic engineering at Yonsei University in Seoul. Since 2015, he has been working as a research assistant at Yonsei University, where he has worked on antenna development for high power antennas.

Jin Soo Choi



received his B.S., M.S., and Ph.D. degrees in physics from Yonsei University, Seoul, Korea, in 1986, 1989, and 2001, respectively. Since 1991, he joined the Agency for Defense Development, Daejeon, Korea, where he is currently a principal researcher. From 2003 to 2004, he was with the Naval Research Laboratory, Washington, DC, USA, as a visiting scientist. His current research interests include explosion phenomena, high power electromagnetic sources, and electromagnetic effects.

Jiheon Ryu



received his B.S. and M.S. degrees in electronic engineering from Sogang University, Seoul, South Korea, in 1998 and 2001, respectively, and a Ph.D. degree in electrical engineering from the Korea Advanced Institute of Science and Technology, Daejeon, South Korea, in 2020. In 2001, he joined the Agency for Defense Development, Daejeon, Korea, where he is currently a principal researcher. He designed many types of high-power wideband pulse generators and antennas in high-power electromagnetic radiator systems. From 2008 to 2009, he was with the Department of Electrical and Computer Engineering, Naval Postgraduate School (NPS), Monterey, CA, USA. He studied distributed digital array radar in NPS. He has been a senior member of the IEEE since 2016. His research interests include high-power microwave, microwave circuit, power transfer circuit, and machine learning. Dr. Ryu was the recipient of the 2010 Defense Acquisition Program Administration Grant Award. He was also the recipient of the 2019 Euibum Academic Award.

Dong-Hee Son



received his B.S. and M.S. degrees in electrical engineering at the Pusan National University, Busan, Korea, in 2017 and 2019, respectively. In 2019, he joined the Hanwha Corporation, Korea, where he is currently an assistant research engineer. His current research interests include the generation and radiation of high-power electromagnetic pulses.

Hae-ok Kwon



received his B.S. and M.S. degrees in Radio Sciences and Engineering at Korea Maritime University, Busan, Korea, in 1998 and 2007, respectively. In 2003, he joined the Hanwha Corporation, Seoul, Korea, where he is currently a principal research engineer. His current research interests include the generation and radiation of high-power electromagnetic pulses.

Young Joong Yoon



earned his B.S. and M.S. in electronics engineering from Yonsei University, Seoul, Korea, in 1981 and 1986, respectively, and a Ph.D. in electrical engineering from the Georgia Institute of Technology, Atlanta, GA, USA, in 1991. From 1992 to 1993, he worked as a senior researcher at the Electronics and Telecommunications Research Institute in Daejeon, South Korea. He joined Yonsei University as a faculty member in 1993, and he is currently a professor at the Department of Electrical and Electronics Engineering. In 2011, he served as the president of the Korean Institute of Electromagnetic Engineering and Science in Seoul. He has more than 30 years of extensive research and development experience in various fields, with a major interest in such systems as ultrasonic, hyperthermia, high power antennas, electronic warfare antennas, and metasurface antennas.

Sang-min Lee

received his B.S. in mechanical engineering at Pusan National University, Busan, Korea, in 1985. He joined Daewoo Electronics, Gumi, Korea, in 1983, and he has been working for the Hanwha Corporation since 2002. He retired in 2021. His current research interests include high-power antennas and sources.

Photograph not available at the time of publication.

Development of a Numerical Tablet Model in WLAN Band for SAR Study

Jisu Lee¹ · Ae-Kyoung Lee² · Seon-Eui Hong² · Hyung-Do Choi² · Kyung-Young Jung^{1,*}

Abstract

This research proposes a numerical model for a tablet in the wireless local area network band for specific absorption rate (SAR) study. The design criteria, such as the tablet size, operating frequencies, antenna position, and target 1-g peak spatial-average SAR (psSAR) values in the flat phantom, are determined based on the SAR test reports of tablets distributed in South Korea from 2013 to 2017. An internal antenna is designed in a tablet platform to operate in dual bands of 2,450 MHz and 5,500 MHz. The numerical results illustrate that the 1-g psSAR values of the proposed numerical tablet model are within $\pm 10\%$ of the target values. Moreover, the return loss of the designed tablet model is larger than 10 dB, regardless of flat phantom, while its radiation efficiency is higher than 90% in free space.

Key Words: Finite-Difference Time-Domain (FDTD) Method, Specific Absorption Rate (SAR), Tablet.

I. INTRODUCTION

Since 2016, several SAR studies have proposed numerical models for mobile phones, including bar-type, folder-type, and smartphone-type mobile phones, in South Korea [1, 2]. Currently, tablets are widely used in wireless local area network (WLAN) services. The use of tablets, especially among infants, is common in many places, such as restaurants and vehicles, thus increasing the need for epidemiological research on tablets used in WLAN services. Therefore, proper evaluation and study of electromagnetic (EM) exposure should be conducted to scientifically judge the health effects of tablet use on humans, especially children.

In this study, for the first time, a numerical tablet model is developed for implementing numerical SAR studies. For this purpose, we analyze the specific absorption rate (SAR) test reports of tablet models distributed in South Korea from 2013

to 2017 to determine the tablet size, operating frequencies, antenna location, and target 1-g peak spatial-average SAR (psSAR) values on the flat phantom. We develop the numerical tablet model such that it satisfies the following conditions: the difference of the 1-g psSAR values (against the target 1-g psSAR values) is within $\pm 10\%$, the $|S_{11}|$ is less than -10 dB, and the radiation efficiency is larger than 90%. The designed antenna operates in dual bands of 2,450 MHz and 5,500 MHz. All simulations are performed using Sim4life [3] based on the accurate and robust finite-difference time-domain (FDTD) method [4–7].

II. NUMERICAL TABLET MODELING

In this study, we develop a simple numerical tablet model that does not include the complicated structures and materials of

Manuscript received December 17, 2021 ; Revised January 10, 2022 ; Accepted February 22, 2022. (ID No. 20211217-151J)

¹Department of Electronic Engineering, Hanyang University, Seoul, Korea.

²Radio Technology Research Department, Electronics and Telecommunications Research Institute (ETRI), Daejeon, Korea.

*Corresponding Author: Kyung-Young Jung (e-mail: kyjung3@hanyang.ac.kr)

This is an Open-Access article distributed under the terms of the Creative Commons Attribution Non-Commercial License (<http://creativecommons.org/licenses/by-nc/4.0>) which permits unrestricted non-commercial use, distribution, and reproduction in any medium, provided the original work is properly cited.

© Copyright The Korean Institute of Electromagnetic Engineering and Science.

commercial tablets. Since the designed numerical tablet model will be employed for future SAR research based on the FDTD method, our simplified tablet modeling can significantly reduce the computational burdens of SAR simulations. As mentioned previously, we decide the design parameters, such as the tablet size, operating frequencies, antenna location, and target 1-g psSAR values on the flat phantom, based on the SAR test reports of commercial tablets released in South Korea in 2013–2017.

The detailed configuration of the numerical tablet model is presented in Fig. 1. The tablet size is set to 255 mm × 170 mm × 8 mm. The thicknesses of the tablet components are listed in Table 1, while their electrical properties, excerpted from [1], are listed in Table 2. Furthermore, Table 3 notes the two WLAN

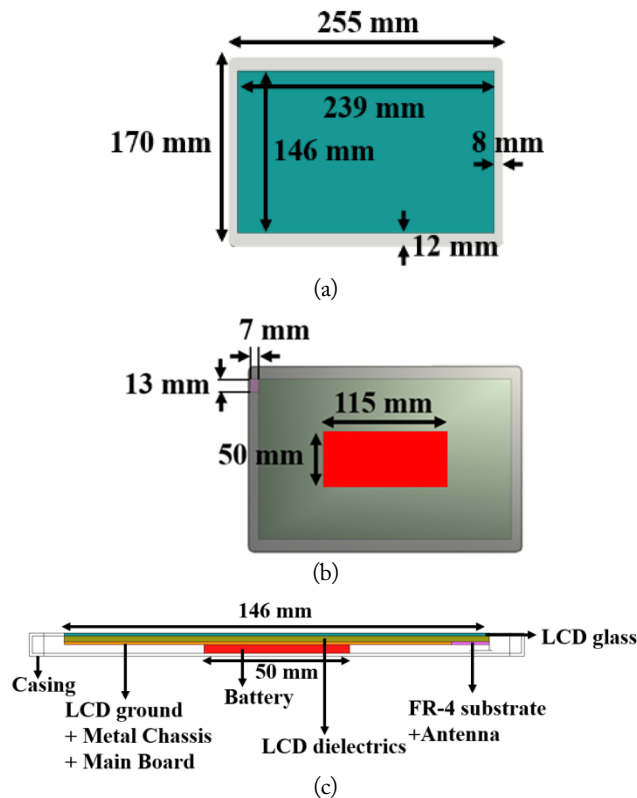


Fig. 1. Schematic diagram of the numerical tablet model: (a) front view, (b) back view, and (c) side view.

Table 1. Thickness of tablet components

Component	Thickness (mm)
Casing	1
LCD glass	1
LCD dielectrics	2
FR-4 substrate	1
LCD ground + Metal chassis + Main board	1
Battery	3

Table 2. Electrical properties of tablet components

Component	Relative permittivity	Conductivity (S/m)
Casing	3.5	0.02
LCD glass	4.5	0.01
LCD dielectrics	3.0	0.01
FR-4 substrate	4.4	0
Antenna		PEC
LCD ground + Metal chassis + Main board		PEC
Battery		PEC

Table 3. WLAN frequency band

Band	Bandwidth (MHz)	SAR target frequency (MHz)
2.4 GHz	2,412–2,472	2,450
5 GHz	5,180–5,825	5,500

bands considered in this study and their respective SAR target frequencies. A survey of the SAR test reports reveals that most WLAN antennas are located at the top right side of tablets. Therefore, in the numerical tablet model, the WLAN antenna is designed to be located at the top right corner.

According to the IEEE standard [8], it is necessary to consider all six planes of a hexahedron tablet device when performing SAR measurements using the flat phantom, as shown in Fig. 2. However, if the distance between the SAR measurement plane and the antenna is more than or equal to 2.5 cm, the corresponding SAR test can be excluded. Therefore, due to the distance between the measurement planes and the antenna location (top

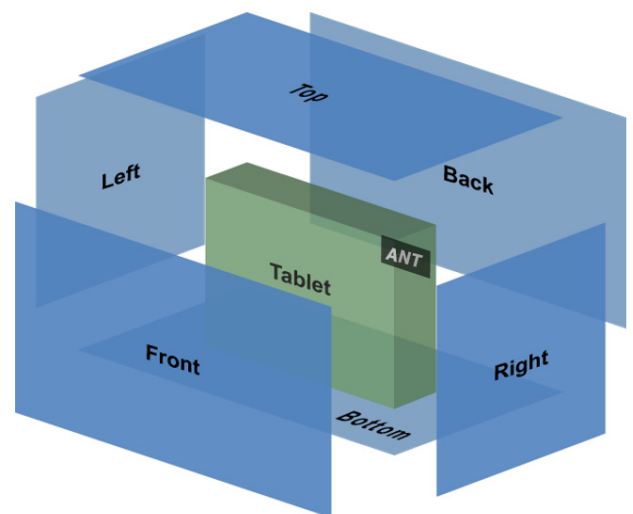


Fig. 2. SAR measurement planes.

right side), only four planes (top, front, back, right) are considered.

In this study, the target 1-g psSAR values are determined by averaging all the measured 1-g psSAR values in the SAR test reports. Besides tablets with top right positioned antennas, we also consider tablets with antennas not located at the top right corner in this study in order to target the 1-g psSAR values. Toward this purpose, we assume that the antenna is located at the top right side, as shown in Fig. 3. For a tablet with the antenna located at the bottom left, as shown in Fig. 3(a), the 1-g psSAR value of the left (right) plane is considered to be that of the right (left), while the 1-g psSAR value of the top (bottom) plane is considered to be that of the bottom (top). Similarly, for Fig. 3(b) and 3(c), it is assumed that the antenna is located at the top right corner. Through this strategy, we can successfully average all the measured 1-g psSAR values of the SAR test reports. The target 1-g psSAR values at 2,450 MHz and 5,500 MHz are listed in Table 4. It should be noted that SAR evaluations for the bottom and left planes are excluded because the distance between the antenna and the SAR measurement planes is longer than 2.5 cm.

It is also of utmost importance to develop a numerical tablet model that yields good antenna performance while simultaneously satisfying the target 1-g psSAR values with small differences. Fig. 4 presents the design guidelines for the model, as also listed

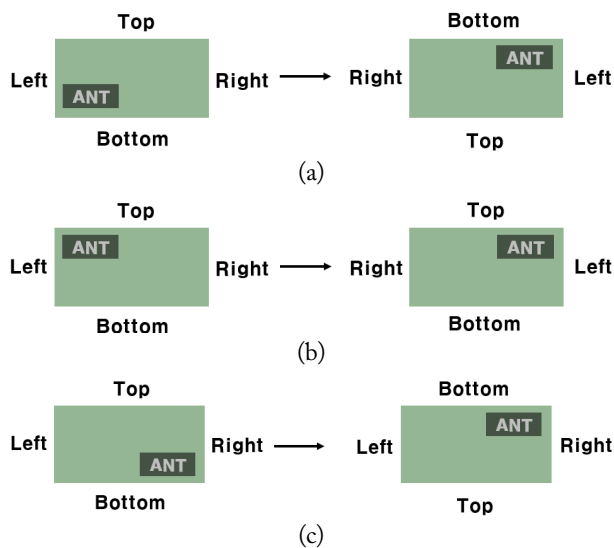


Fig. 3. Equivalent tablet model with antenna position at the top right corner: (a) original antenna position (bottom left), (b) original antenna position (top left), and (c) original antenna position (bottom right).

Table 4. Target 1-g psSAR values

Frequency (MHz)	Target 1-g psSAR values (W/kg)					
	Front	Back	Top	Bottom	Right	Left
2,450	0.091	0.112	0.026	N/A	0.066	N/A
5,500	0.143	0.123	0.032	N/A	0.151	N/A

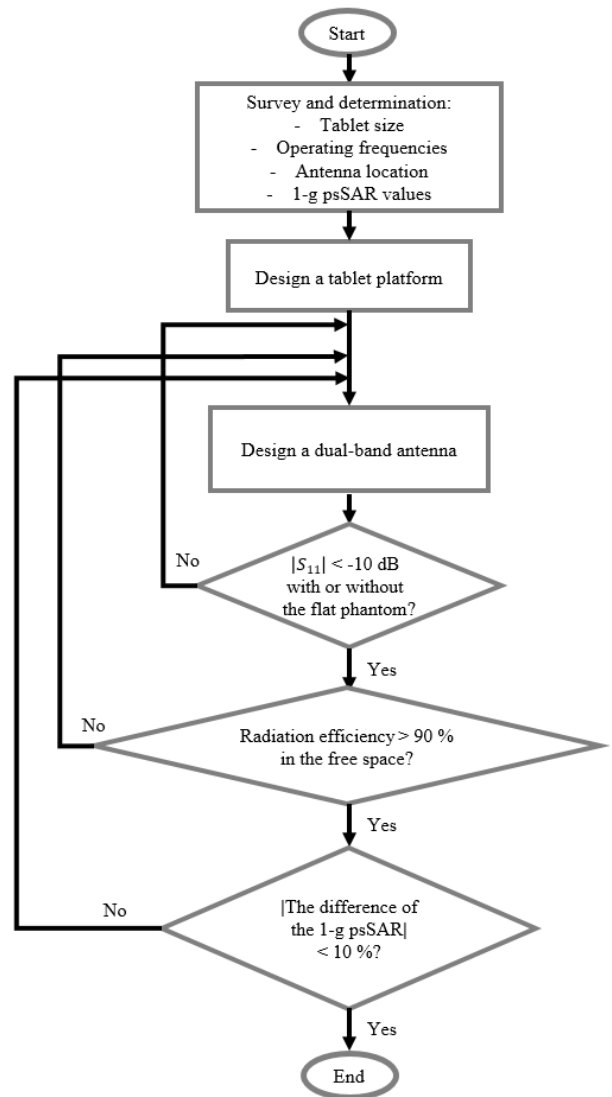


Fig. 4. Design flowchart for the numerical tablet model.

below:

- (1) The magnitude of S_{11} should be less than -10 dB, irrespective of the existence of a flat phantom.
- (2) The radiation efficiency should be higher than 90% in free space.
- (3) The difference between the 1-g psSAR value and the target value should be within $\pm 10\%$.

Before proceeding with the antenna design, the issue of the flat phantom, referred to in the IEEE standard [8], should be addressed. The flat phantom is composed of a liquid and a shell. The liquid takes the shape of a rectangular parallelepiped with a width of 355 mm, length of 270 mm, and thickness of 180 mm. Notably, the bottom of the liquid is covered by a 2-mm thick shell, whose relative permittivity is 3.7. The electrical properties of the liquid are listed in Table 5. The tablet is positioned 10 mm away from the liquid in the flat phantom in all FDTD SAR evaluations.

Table 5. Electrical properties of the liquid

Frequency (MHz)	Relative permittivity	Conductivity (S/m)
2,450	39.2	1.8
5,500	35.65	4.965

The inverted-F antenna [9, 10] is employed in the numerical tablet model. In this study, the antenna is designed to operate in dual bands (2.4 GHz and 5 GHz bands). After extensive FDTD simulations, we designed a dual-band antenna that satisfies the above-mentioned design criteria. The antenna configuration is presented in Fig. 5, and the antenna parameters are listed in Table 6.

III. NUMERICAL RESULTS

This section provides the FDTD simulation results of the designed numerical tablet model. The reflection coefficient and radiation efficiency are depicted in Figs. 6 and 7. Fig. 6 shows that $|S_{11}|$ is less than -10 dB for the numerical tablet model, irrespective of the presence of a flat phantom in both WLAN bands. Fig. 7 illustrates that the radiation efficiency of the numerical tablet model in free space is higher than 90%. It is also observed that the loss of the flat phantom reduces radiation

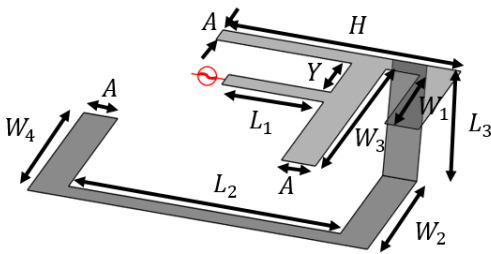


Fig. 5. Antenna configuration.

Table 6. Antenna parameters

Parameter	Value (mm)
A	1
H	7
Y	3
W_1	5
W_2	7
W_3	10
W_4	8
L_1	3
L_2	8
L_3	3

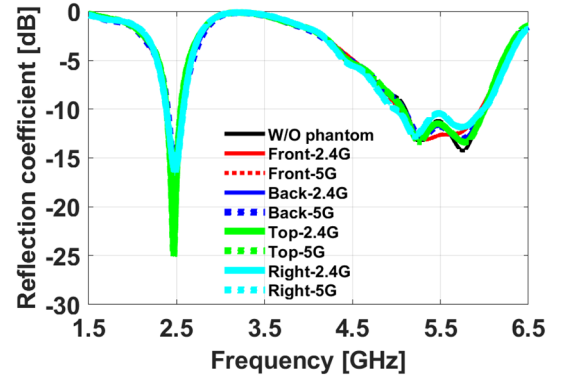


Fig. 6. Reflection coefficient.

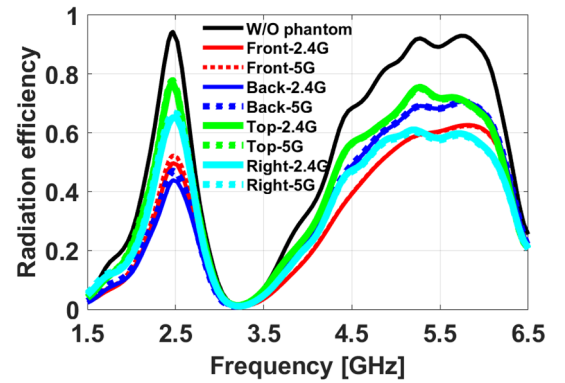


Fig. 7. Radiation efficiency.

efficiency. The simulated 1-g psSAR values and their target values for the target frequency of 2,450 MHz are listed in Table 7, while Table 8 notes the same for the 5,500 MHz frequency band. The maximum difference between the target values and result values is -9.93% . Overall, it is observed that the numerical tablet model developed in this study satisfies all design criteria.

Table 7. Target and simulated 1-g psSAR values at the 2,450 MHz target frequency

	1-g psSAR			
	Front	Back	Top	Right
Target value (W/kg)	0.091	0.112	0.026	0.066
Result value (W/kg)	0.0957	0.11	0.0239	0.0713
Difference (%)	5.16	-1.79	-8.08	8.03

Table 8. Target and simulated 1-g psSAR values at the 5,500 MHz target frequency

	1-g psSAR			
	Front	Back	Top	Right
Target value (W/kg)	0.143	0.123	0.032	0.151
Result value (W/kg)	0.157	0.131	0.0318	0.136
Difference (%)	9.79	6.5	-0.62	-9.93

IV. CONCLUDING REMARKS

The widespread use of tablets necessitates the development of a numerical tablet model for SAR study. In this work, we present a numerical tablet model composed of a tablet platform and a dual-band antenna in the WLAN band. The design parameters of the numerical tablet model, including its size, operating frequencies, and antenna location, are determined by investigating the SAR test reports of tablets released in South Korea in 2013–2017. Drawing on this data, we developed a numerical tablet model that satisfies crucial design guidelines, such as antenna performance and 1-g psSAR values on a flat phantom. Numerical simulations conducted in this study demonstrate that (1) the return loss of the numerical tablet model is larger than 10 dB, regardless of the existence of flat phantom, (2) the radiation efficiency of the numerical tablet model in free space is higher than 90%, and (3) the maximum difference between the simulated 1-g psSAR values and the target values is -9.93% . Our well-designed numerical tablet model can be applied for on-going epidemiological studies on the use of tablets.

This work was supported in part by the ICT R&D program of MSIT/IITP (No. 2019-0-00102, A Study on Public Health and Safety in a Complex EMF Environment) and in part by the National Research Foundation of Korea (NRF) grant funded by the Korea government (MSIT) (No. 2020 R1F1A1055444). The authors would like to thank Samsung Electronics for allowing the use of their SAR test reports.

REFERENCES

- [1] A. K. Lee, Y. Yoon, S. Lee, B. Lee, S. E. Hong, H. D. Choi, and E. Cardis, "Numerical implementation of representative mobile phone models for epidemiological studies," *Journal of Electromagnetic Engineering and Science*, vol. 16, no. 2, pp. 87–99, 2016.
- [2] J. Lee, A. K. Lee, S. E. Hong, H. D. Choi, and K. Y. Jung, "Numerical modeling of smartphones with WCDMA, LTE, and WLAN bands for epidemiological studies," *Journal of Electromagnetic Engineering and Science*, vol. 22, no. 1, pp. 41–47, 2022.
- [3] Sim4life [Online]. Available: <http://zurichmedtech.com>.
- [4] J. Cho, M. S. Park, and K. Y. Jung, "Perfectly matched layer for accurate FDTD for anisotropic magnetized plasma," *Journal of Electromagnetic Engineering and Science*, vol. 20, no. 4, pp. 277–284, 2020.
- [5] J. Park and K. Y. Jung, "Numerical stability of modified Lorentz FDTD unified from various dispersion models," *Optics Express*, vol. 29, no. 14, pp. 21639–21654, 2021.
- [6] S. Jang and K. Y. Jung, "Perfectly matched layer formulation of the INBC-FDTD algorithm for electromagnetic analysis of thin film materials," *IEEE Access*, vol. 9, pp. 118099–118106, 2021.
- [7] Y. J. Kim and K. Y. Jung, "Accurate and efficient finite-difference time-domain formulation of dusty plasma," *IEEE Transactions on Antennas and Propagation*, vol. 69, no. 10, pp. 6600–6606, 2021.
- [8] *Measurement procedure for the assessment of specific absorption rate of human exposure to radio frequency fields from hand-held and body-mounted wireless communication devices – Human models, instrumentation, and procedures (Frequency range of 4 MHz to 10 GHz)*, IEC/IEEE 62209-1528:2020, 2020.
- [9] J. Lee, S. Park, A. K. Lee, H. D. Choi, and K. Y. Jung, "Numerical study of maximum peak spatial SAR reduction in a mobile phone," *Journal of Electrical Engineering & Technology*, vol. 15, no. 5, pp. 2211–2216, 2020.
- [10] S. H. Hsieh, D. L. Huang, F. S. Chen, C. F. Yang, Y. C. Chien, and Y. Y. Chan, "A compact inverted-F antenna for dual-band WLAN operations in a mini tablet computer," in *Proceedings of 2012 IEEE Asia-Pacific Conference on Antennas and Propagation*, Singapore, 2012, pp. 76–77.

Jisu Lee



received her B.S. degree in Electronic Engineering from Seokyeong University, Seoul, Republic of Korea, in 2019. She is currently pursuing her Ph.D. in Electronic Engineering at Hanyang University, Seoul, Republic of South Korea. Her current research interests include antenna development.

Hyung-Do Choi



received his M.S. and Ph.D. degrees in Material Science from Korea University, Seoul, Republic of Korea, in 1989 and 1996, respectively. Since 1997, he has been working with the Electronics and Telecommunications Research Institute, Republic of Korea, as a principal researcher at the Radio and Satellite Research Division. He has performed research on the biological effects of RF radiation and has developed RF radiation protection standards and regulations. His current research interests include spectrum management, microwave tomography, and EMC countermeasures. He has also received a Technology Award from the Korean Institute of Electromagnetic Engineering and Science.

Ae-Kyoung Lee



received her B.S. and M.S. degrees in Electronic Engineering from Chungang University, Seoul, Republic of Korea, in 1990 and 1992, respectively. She received her Ph.D. in Radio Science and Engineering from Chungnam National University, Daejeon, Republic of South Korea, in 2003. In 1992, she joined the Radio Technology Group at the Electronics and Telecommunications Research Institute, Daejeon,

Republic of Korea, where she is currently a principal researcher and has been involved in projects on measurement technologies and numerical analyses of electromagnetic compatibility and human exposure to RF fields. She was the recipient of the Japan Microwave Prize at the 1998 Asia-Pacific Microwave Conference, Japan, and the Technology Award from the Korean Institute of Electromagnetic Engineering and Science in 1999.

Kyung-Young Jung



received his B.S. and M.S. degrees in Electrical Engineering from Hanyang University, Seoul, Republic of Korea, in 1996 and 1998, respectively. He received his Ph.D. in Electrical and Computer Engineering from Ohio State University, Columbus, USA, in 2008. From 2008 to 2009, he was a post-doctoral researcher at Ohio State University. From 2009 to 2010, he was an assistant professor in the

Department of Electrical and Computer Engineering, Ajou University, Suwon, Republic of Korea. Since 2011, he has worked at Hanyang University, where he is currently a professor in the Department of Electronic Engineering. His current research interests include computational electromagnetics, bioelectromagnetics, and nanoelectromagnetics. Dr. Jung received a Graduate Study Abroad Scholarship from the National Research Foundation of Korea, a Presidential Fellowship from Ohio State University, an HYU Distinguished Teaching Professor Award from Hanyang University, and an Outstanding Research Award from the Korean Institute of Electromagnetic Engineering and Science.

Seon-Eui Hong



received her M.S. and Ph.D. degrees in Radio Science and Engineering from Chungnam National University, Daejeon, Republic of Korea, in 1999 and 2017, respectively. Since 1999, she has been working with the Electronics and Telecommunications Research Institute, Daejeon, Republic of Korea, and is currently a principal member of the radio environment and monitoring research group. Her current research

interests include numerical dosimetry and procedures for assessing electromagnetic sources.

A Wideband Doherty Combiner with Phase Variation Compensation Using LTCC Applicable for High Power Transmission

Youna Jang · Kwanhun Jeong · Jiwon Kim · Daeung Lee · Dal Ahn*

Abstract

In this paper, we propose a small-sized Doherty combiner with phase variation compensation using low temperature co-fired ceramic (LTCC) substrate. The proposed design theory for the Doherty combiner is derived using the phase calculation of the S -parameter based on the relation between the input and output ports. The proposed circuit is designed after determining the band edge frequency and the targeted degree of the phase balance. The proposed circuit is verified using the microstrip line and the LTCC substrate. The implemented structure, using LTCC as the substrate, is operated under a high-power test of continuous wave 50 W, the results of which also show that the amplitude and phase balance have variations within 0.2 dB and $\pm 1^\circ$, respectively. The high-power test shows that the implemented structure is applicable for high power Doherty amplifiers or combiners.

Key Words: Doherty Combiner, High Power Test, LTCC Substrate, Transmission Line, Wide Bandwidth.

I. INTRODUCTION

A power amplifier (PA) is an important component that satisfies the requirements of high linearity and high-power efficiency in a radio frequency (RF) communication system. The PA generally operates near the saturation region to achieve maximum power efficiency. However, the power efficiency of a PA undergoes degradation due to distortions in output signals. Furthermore, its efficiency degrades if the PA operates at power levels below the saturation region. As efficiency decreases, most of the power diverges to produce heat, which deteriorates the characteristics of the amplifier and causes various issues, including heat generation and heat dissipation problems [1–2]. The Doherty power amplifier (DPA) possesses the advantages

of easy implementation and high-power efficiency, although it is widely known to suffer from the disadvantage of a narrow bandwidth.

Therefore, many studies [3–9] have attempted to improve the narrow bandwidth of the DPA. For this purpose, previous studies have used a two-stepped transmission line impedance transformer [3], a branch line structure with a splitter and a combiner [4–5], and the addition of resonance circuits [6–8] or an additional line [9]. However, these previous designs occupy large combiner areas on their substrates due to the $\lambda/4$ or $\lambda/2$ electrical lengths of their microstrip lines.

In this paper, a Doherty combiner is implemented to improve the phase bandwidth and reduce the size of the proposed combiner using low temperature co-fired ceramic (LTCC) as the

Manuscript received December 1, 2021 ; Revised January 11, 2022 ; Accepted May 4, 2022. (ID No. 20211201-141J)

Department of ICT Convergence, Soonchunhyang University, Asan, Korea.

*Corresponding Author: Dal Ahn (e-mail: dahnkr@sch.ac.kr)

This is an Open-Access article distributed under the terms of the Creative Commons Attribution Non-Commercial License (<http://creativecommons.org/licenses/by-nc/4.0>) which permits unrestricted non-commercial use, distribution, and reproduction in any medium, provided the original work is properly cited.

© Copyright The Korean Institute of Electromagnetic Engineering and Science.

substrate. In addition, the desired target specification is satisfied as a result of the continuous wave (CW) 50 W high power test, suggesting the possibility of not only miniaturization but also high-power RF systems.

II. DESIGN THEORY

The basic structure of the Doherty power amplifier is composed of a carrier amplifier, a peaking amplifier, and a combiner region, as depicted in Fig. 1(a). The carrier amplifier stage is combined at P'_1 , the peaking amplifier stage at P'_2 , and the output power at P'_3 . The proposed combiner adds a 2θ transmission line between P_2 and P'_1 , as shown in Fig. 1(b), while the added characteristic impedance is Z_C . The added transmission line establishes the desired phase deviation of the target band edge frequency. Phases $\angle S_{31}$ and $\angle S_{32}$ of the proposed structure can be obtained by Eqs. (1) and (2) through the $ABCD|_{31}$ and $ABCD|_{32}$ of [9] and by applying the electrical length θ of the phase shift line from point P_1 to P'_1 and the $\angle S_{31}''$.

$$\begin{aligned} \angle S_{31} &= \theta + \angle S_{31}'' \\ &= \theta - \angle \tan^{-1} \left\{ \frac{\left(\frac{1}{\sqrt{2}} + \sqrt{2} \right) \sin \theta + \left(\frac{A}{\delta} \right) \cos \theta + \left(\frac{B}{2(\delta)} \right) \sin \theta}{2 \cos \theta + \left(\frac{C}{\delta} \right) \cos \theta + \left(\frac{D}{2(\delta)} \right) \sin \theta} \right\} \end{aligned} \quad (1)$$

where,

$$\begin{aligned} A &= Z_0 Z_C \tan 2\theta (50^2 - Z_C^2), \quad B = 50\sqrt{2}Z_0 Z_C^2 (1 + \tan 2\theta^2), \\ C &= 50Z_0 Z_C^2 (1 + \tan 2\theta^2), \quad D = \sqrt{2}Z_0 Z_C \tan 2\theta (50^2 - Z_C^2), \\ \delta &= 50^2 Z_C^2 + Z_C^4 \tan 2\theta^2. \end{aligned}$$

$$\angle S_{32} = -\angle \tan^{-1} \left\{ \frac{\sin 2\theta \cos \theta \left(\frac{2Z_C + Z_0}{Z_0} \right) + 2\sqrt{2} \cos 2\theta \sin \theta}{3 \cos 2\theta \cos \theta - \sin 2\theta \sin \theta \left(\frac{3\sqrt{2}Z_C + \sqrt{2}Z_0}{2Z_0} \right)} \right\} \quad (2)$$

Assuming that the phase differences of $\angle S_{31}$ and $\angle S_{32}$ at center frequency f_0 is \emptyset , the phase difference \emptyset_0 between the two inputs of the proposed structure at f_0 is $\emptyset_0 = \theta_0 + \angle S_{31}''|_{\theta_0} - \angle S_{32}|_{\theta_0}$. Meanwhile, the phase difference \emptyset_1 be-

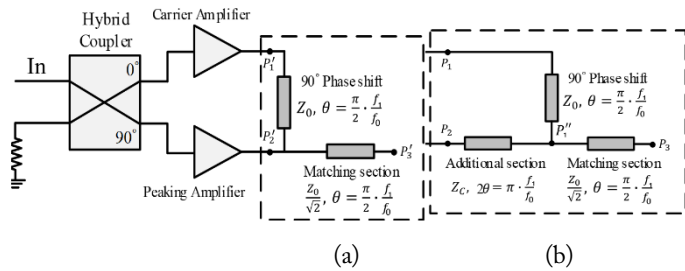


Fig. 1. Block diagram of the Doherty power amplifier with (a) a conventional combiner, and (b) the proposed output combiner.

tween the two inputs at the selected frequency f_1 is obtained as $\emptyset_1 = \theta_1 + \angle S_{31}''|_{\theta_1} - \angle S_{32}|_{\theta_1}$. Thus, when $\theta_0 = \frac{\pi}{2}$, a phase difference of 90° can be obtained at the center frequency through Eq. (3) [9].

$$(\emptyset_0 - \emptyset_1) - \frac{\pi}{2} \left(1 - \frac{\omega_1}{\omega_0} \right) = -\angle S_{31}''|_{\theta=\theta_1} + \angle S_{32}|_{\theta=\theta_1} \quad (3)$$

The proposed circuit has a center frequency of 3.5 GHz, while the phase deviation is set to 2° at an edge frequency of 3.6 GHz. Finally, the Z_C of the additional transmission line is obtained by solving $\angle S_{31}''$, $\angle S_{32}$, $\theta_1 = \frac{\omega_1 \pi}{\omega_0 2}$, and Eq. (3). The obtained value of the transmission line Z_C is 38.81 ohm.

III. 3D STRUCTURE AND FABRICATION RESULTS

The proposed circuit is implemented using an LTCC substrate with a dielectric constant of 6 for a small-sized Doherty combiner, as shown in Fig. 2. The ground L2 is added in order to integrate three transmission lines into one chip. The thickness of the chip from L1 to L3, as depicted in Fig. 2(a) and 2(b), is controlled through the characteristic impedance equations of the strip line. One of the three lines is for the 180° electrical length of the additional section, while the other two lines are for the 90° phase and the matching section.

Since the characteristic impedance Z_C of the additional section has 38.81 Ω with a 180° electrical length, the additional line is located at the L3 layer, which is 0.15 mm away from the bottom ground (GND).

To apply a 180° line within a 6.35 mm \times 5.08 mm size, as shown in Fig. 2(c)–2(e), the height of the layer from the GND is reduced to realize a wider line width for Z_C . The two lines for the 90° phase shift and the matching section are implemented in one layer. The L1 and L3 layers are connected at the P'_1 node. The realized LTCC structure is then mounted on the PCB substrate—a Rogers 5880 with a dielectric constant of 2.2. Fig. 3(a)–

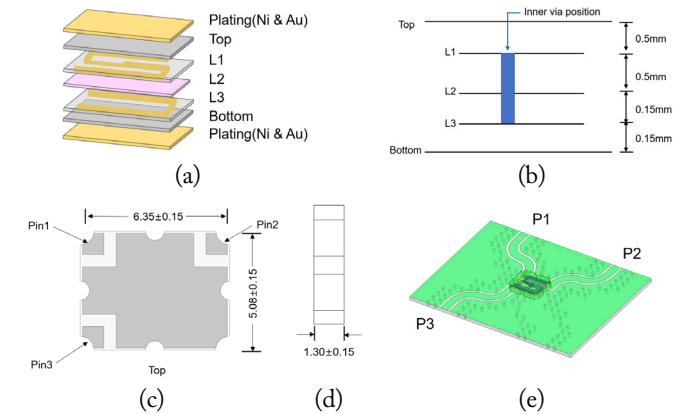


Fig. 2. (a) LTCC diagrams with several layers, (b) side diagrams of the LTCC, (c) top dimension, (d) side dimension, and (e) 3D structure with PCB substrate.

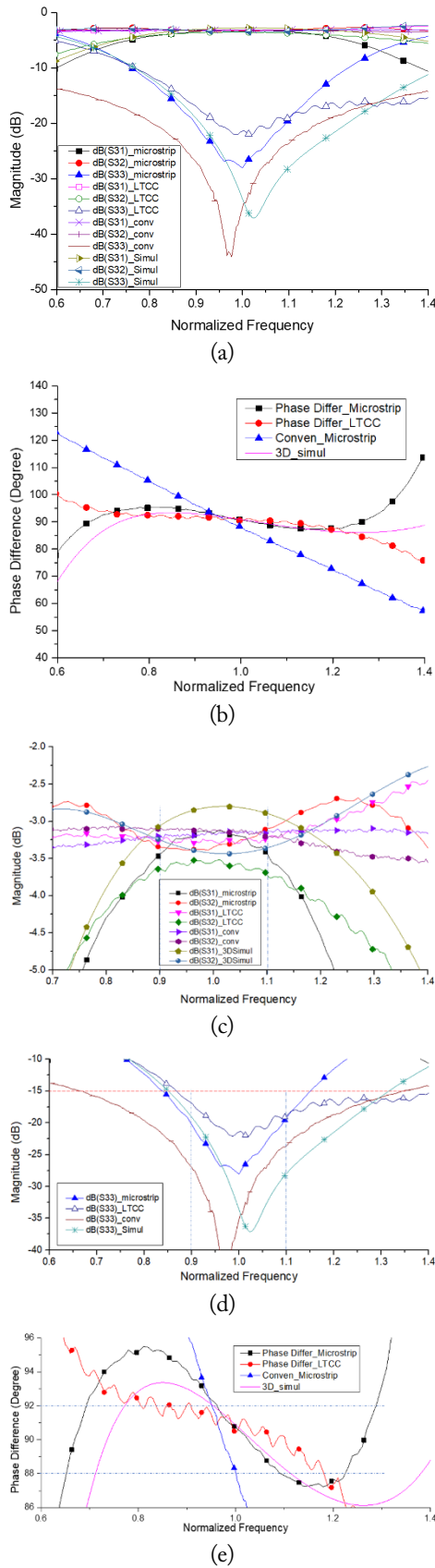


Fig. 3. Comparison results of the conventional, proposed 3D structure, and measured results: (a) magnitude, (b) output phase difference, (c) insertion loss, (d) return loss, and (e) phase balance.

3(e) show the magnitude characteristics, phase differences, insertion loss, return loss, and phase balance of the fabrication results. The Doherty combiner is implemented using a Rogers 5880 microstrip line. The magnitude results are $S_{31} = -3.16$ dB, $S_{32} = -3.35$ dB, and $S_{33} = -28.06$ dB, while the phase difference is 90.72° at the normalized center frequency. Meanwhile, the Doherty combiner with the LTCC substrate exhibits magnitude performances of $S_{31} = -3.26$ dB, $S_{32} = -3.54$ dB, and $S_{33} = -21.42$ dB, with a 90.39° phase difference between S_{32} and S_{31} at normalized center frequency. The analysis confirmed that it has uniform phase differences within the targeted bandwidth close to 90° at the center frequency and close to 89.71° at the normalized selected frequency ($f_1 = 1.06$). The proposed structure has a 34.3% normalized fractional bandwidth (FBW) ranging from 0.837 to 1.18 for $90^\circ \pm 2^\circ$. The magnitude and phase characteristics of the LTCC Doherty combiner also show similar results as the proposed circuit using the microstrip line. Therefore, the measurement results confirm the validity of the proposed theory.

IV. HIGH POWER TEST OF DUT

Fig. 4(a) shows the PCB jig with the LTCC substrate implemented as the Device Under Test (DUT). The high-power test (HPT) is used for checking RF performances when high power is conducted by the test jigs. Fig. 4(b) depicts the setup for the HPT. The equipment required for the HPT process consists of a signal generator, a power amplifier, a power meter, an isolator, a coupler, a termination component, and two test jigs. The signal generator produces a signal, which the power amplifier amplifies, while the power meter checks whether 50 W power is appropriately supplied. The HPT procedures are as follows:

1. The experimental setup for the high-power test is organized, as shown in Fig. 4(b).
2. Two DUT's are linked with each other in a back-to-back connection—the P3 of the first DUT signifies the input port, while the P3 of the second DUT signifies the output port.
3. A 50-W CW at 3.6 GHz is applied to the P3 of the first DUT for 5 minutes.
4. The other DUT's are also tested in the same manner.

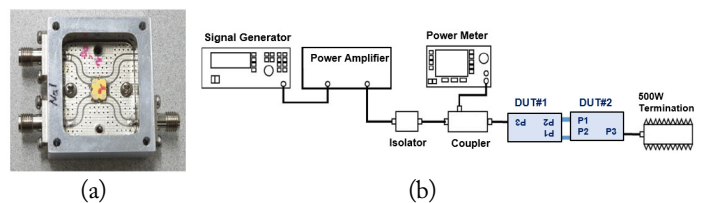


Fig. 4. (a) PCB jig with DUT, (b) setup diagram for the high-power test.

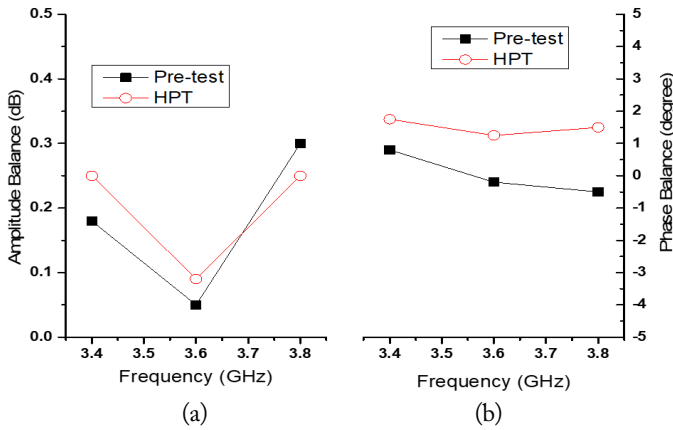


Fig. 5. Pre- and post-high-power test: (a) amplitude balance and (b) phase balance.

The HPT results highlight that the amplitude and phase balance have variations within 0.2 dB and $\pm 1^\circ$, respectively, as shown in Fig. 5. Therefore, the proposed Doherty combiner using LTCC operates well, with fewer variations in phase balance, even under 50 W CW conditions.

V. CONCLUSION

In this paper, a small-sized Doherty combiner using LTCC substrate is proposed. The structure sets the selected frequency of f_1 and the targeted degree of phase balance. Thus, the characteristic impedance with a 180° line can be obtained in the additional section of the combiner from the proposed design theory. Furthermore, to minimize the circuit size, the proposed circuit was implemented using three layers in the LTCC substrate. For the wideband application of the Doherty power amplifier, the proposed circuit was operated under CW 50 W at 3.6 GHz. The amplitude and phase balance were found to be less than 0.06 dB and $\pm 1^\circ$, respectively. Therefore, the proposed circuit is applicable for use in miniaturized high power Doherty Power amplifiers and small-sized high-power combiners in future communication systems.

These results are supported by the Regional Innovation Strategy (RIS) through the National Research Foundation of Korea (NRF), funded by the Ministry of Education (MOE) (No. 2021RIS-004) and the Soonchunhyang University Research Fund.

REFERENCES

- [1] S. C. Cripps, *RF Power Amplifiers for Wireless Communications*, Norwood, MA: Artech House, 1999.
- [2] B. Kim, J. Kim, I. Kim, and J. Cha, "The Doherty power amplifier," *IEEE Microwave Magazine*, vol. 7, no. 5, pp. 42-50, 2006.
- [3] A. Grebennikov and J. Wong, "A dual-band parallel Doherty power amplifier for wireless applications," *IEEE Transactions on Microwave Theory and Techniques*, vol. 60, no. 10, pp. 3214-3222, 2012.
- [4] L. Piazzon, R. Giofre, P. Colantonio, and F. Giannini, "A wideband Doherty architecture with 36% of fractional bandwidth," *IEEE Microwave and Wireless Components Letters*, vol. 23, no. 11, pp. 626-628, 2013.
- [5] R. Giofre, P. Colantonio, F. Giannini, and L. Piazzon, "New output combiner for Doherty amplifiers," *IEEE Microwave and Wireless Components Letters*, vol. 23, no. 1, pp. 31-33, 2013.
- [6] M. N. A. Abadi, H. Golestaneh, H. Sarbishaei, and S. Boumaiza, "An extended bandwidth Doherty power amplifier using a novel output combiner," in *Proceedings of 2014 IEEE MTT-S International Microwave Symposium (IMS)*, Tampa, FL, 2014, pp. 1-4.
- [7] S. Chen, "New output combiner design for broadband Doherty power amplifier," in *Proceedings of 2016 IEEE International Conference on Computational Electromagnetics (ICCEM)*, Guangzhou, China, 2016, pp. 391-393.
- [8] S. Chen, G. Wang, Z. Cheng, and Q. Xue, "A bandwidth enhanced Doherty power amplifier with a compact output combiner," *IEEE Microwave and Wireless Components Letters*, vol. 26, no. 6, pp. 434-436, 2016.
- [9] D. Lee, S. Kim, Y. Jang, S. Koo, I. S. Kim, J. Lim, J. Cho, and D. Ahn, "Modified Doherty combiner with adjustable phase deviation," *Microwave and Optical Technology Letters*, vol. 60, no. 11, pp. 2834-2839, 2018.

Youna Jang



received her master's degree in Display Engineering from Hanyang University, Seoul, Korea, in 2014. She also received her Ph.D. in Electrical Communication System Engineering from Soonchunhyang University, Choongnam, Korea, in 2019. She participated as a designer of the Duplexer filter in an internship program in 2015 at Qorvo, Bundang, South Korea. She was a lecturer at Soonchunhyang University from 2016 to 2020. She is currently a research professor at the Radio and Mechatronics Research Center. Her research areas include the design of passive components in microwave bands.

Daeung Lee



was born in Korea in 1989. He received his Ph.D. degree in Electrical and Communication System Engineering from Soonchunhyang University, Asan, Korea, in 2019. Currently, he works for Huba. His current research interests include RF passive elements theory, design, and multi-layer passive device design.

Kwanhun Jeong



was born in Mokpo, Korea, in 1994. He received his B.E. degree in Electrical Engineering from Soonchunhyang University, Asan, Korea, in 2020. Currently, he is an M.E. student at Soonchunhyang University. His current research interests include RF passive device theory, design, and testing.

Dal Ahn



received his B.S., M.S., and Ph.D. degrees in Electronics from Sogang University, Seoul, Korea, in 1984, 1986, and 1990, respectively. From 1990 to 1992, he worked with the Mobile Communications Division, Electronics, and Telecommunications Research Institute (ETRI), Daejeon, Korea. Since 1992, he has been affiliated with the School of Electrical and Electronic Engineering, Soonchunhyang University, Asan, Chungnam, Korea, where he is currently a professor. Currently, he is also the chief of the RF and Microwave Component Research Center (RAMREC), Soonchunhyang University. He is also a technical consultant for Tel Wave Inc., Suwon, Korea. His current research interests include the design and application of passive and active components at radio and microwave frequencies, the design of RF front-end modules for various handset systems using low-temperature co-fired ceramic (LTCC) technology, DGS circuit applications, and circuit modeling using a commercial EM analysis program. Prof. Ahn is also an editor of the *Journal of Korea Electromagnetic Engineering Society* and a senior member of the Korea Electromagnetic Engineering Society (KEES).

Jiwon Kim



was born in Seoul, Korea, in 1994. She received her M.E. degree in Electrical Communication System Engineering from Soonchunhyang University, Asan, Korea, in 2019. Currently, she is a Ph.D. student at Soonchunhyang University. Her current research interests include RF passive device and filter design, and process design kit (PDK).

Free-Space Unknown Thru Measurement Using Planar Offset Short for Material Characterization

Jin-Seob Kang*

Abstract

Material characterization requires the proper calibration of a material measurement system. This paper describes a free-space unknown thru measurement method using three independent planar metal offset shorts for calibrating a free-space material measurement system. This method is validated by comparing the measurement results with those of the TRL (thru-reflect-line) measurement method for two glass plates of 2.780 mm and 4.775 mm thickness in W-band (75–110 GHz). This can be an affordable and effective alternative to conventional free-space material measurement methods because the precision fabrication of a planar offset short is more feasible and inexpensive than building a precise positioning system in a free-space material measurement system. One can use this measurement method up to a high-frequency range that the fabrication accuracy of a planar offset short is acceptable.

Key Words: Calibration, Free-Space Measurement, Material Measurement, Unknown Thru Calibration.

I. INTRODUCTION

Recently, the application and use of electromagnetic (EM) materials, devices, and systems have become more prevalent in the natural and applied science fields, which need electrical parameters of EM materials, such as permittivity [1], permeability [2], and reflectivity [3], for analyzing and designing EM devices and systems.

The transmission/reflection (T/R) material measurement method [4–6], which is based on the properties of the transmission line—such as a closed guided-wave structure (e.g., coaxial line and waveguide) and an open guided-wave structure (e.g., free space)—is widely used for material parameter measurements. The closed guided-wave T/R material measurement method measures the scattering parameters of an MUT (material under test) located inside a closed guided-wave structure. This

material measurement method is usually used in a low-frequency range, where precise machining for inserting the MUT into the guided-wave structure is available. On the other hand, the open guided-wave T/R material measurement method measures the scattering parameters of an MUT placed between two antennas in free space, as shown in Fig. 1. This material measurement method is suitable for non-destructive testing of an MUT without prior machining and physical contact at varying temperatures in a high-frequency range using the antennas with a manageable size. Meanwhile, the coaxial line T/R material measurement method [4, 7] can provide a broadband material parameter since the coaxial line supports the propagation of a TEM mode. In contrast, waveguide [5, 6] and free-space [8–11] T/R material measurement methods can only provide a frequency-banded material parameter due to limits on the operating frequency of the waveguide and antenna.

Manuscript received December 30, 2021 ; Revised March 15, 2022 ; Accepted April 5, 2022. (ID No. 20211230-165J)

Safety Measurement Institute, Korea Research Institute of Standards and Science (KRISS), Daejeon, Korea.

*Corresponding Author: Jin-Seob Kang (e-mail: jinskang@kriss.re.kr)

This is an Open-Access article distributed under the terms of the Creative Commons Attribution Non-Commercial License (<http://creativecommons.org/licenses/by-nc/4.0>) which permits unrestricted non-commercial use, distribution, and reproduction in any medium, provided the original work is properly cited.

© Copyright The Korean Institute of Electromagnetic Engineering and Science.

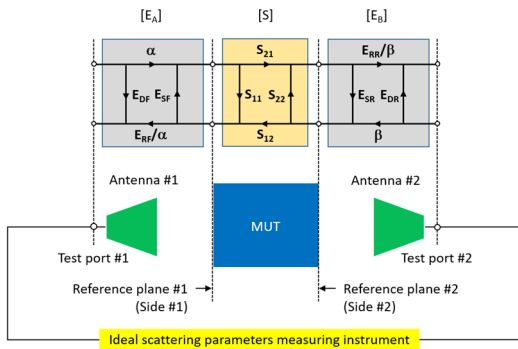


Fig. 1. Two-port eight-term error model of a free-space T/R material measurement.

Usually, EM material measurements exhibit a discrepancy between the measured material parameter of an MUT and its real material parameter due to measurement errors in the measured parameter. From a metrological point of view, the measurement error consists of a systematic error, a random error, and a drift error. Systematic error, which is attributed to imperfections in a measurement system, is the most dominant among measurement error components. Systematic errors can be assumed to be time-invariant, modeled, and mathematically characterized during the calibration of a measurement system [12, 13].

In general, a free-space T/R material measurement consists of the following steps [8–11]:

- Step 1. Calibrating a material measurement system including a scattering parameter measuring instrument, such as a vector network analyzer (VNA), to determine the reference planes (#1 and #2) of the measurement system for both sides (#1 and #2) of an MUT between two antennas, as shown in Fig. 1;
- Step 2. Measuring the scattering parameters of the MUT using the calibrated material measurement system; and
- Step 3. Extracting the material parameters of the MUT from the measured scattering parameters using EM theory.

Accurate and precise measurement of an MUT’s scattering parameters is essential to improving the measurement uncertainty of parameters extracted from a T/R material measurement. Notably, measurement uncertainty depends on the characteristics of the impedance standards and the method used to calibrate a material measurement system.

Free-space calibration methods, such as the TRL (thru-reflect-line), TRM (thru-reflect-match), and GRL (gated-reflect-line) methods, are widely used for T/R material measurement. The TRL method [8, 9] requires a precise positioning system to adjust the separation distance between an antenna and an MUT in free space. This method is susceptible to measurement errors due to the movement of the RF cable that is used to connect the antenna to the scattering parameters measuring instrument. Meanwhile, the TRM method [14], as a variant of the TRL

method, may be used in a low-frequency range where a well-matched broadband EM absorber is available. The GRL method [15] requires a time-gating measurement and a planar metal plate that is as thick as an MUT during calibration, as well as a de-embedding process to compensate for the effect of the difference in thickness of the planar metal plate and the MUT during measurement. Effectively, the TRM and GRL methods can be applied to cases where both the MUT and antenna are fixed and avoid the movement of RF cable.

On the other hand, the unknown thru calibration method [16, 17], also called the SOLR (short-open-load-reciprocal thru) calibration method, is used for measuring the scattering parameters of non-insertable two-port DUTs (devices under test) whose connectors cannot mate together, such as a coaxial to waveguide adapter. The unknown thru calibration method is composed of (i) one-port calibration at each reference plane of a measurement system, where it needs at least three reflect standards (e.g., short, open, and load for a coaxial case; short, offset short, and load for a waveguide case), and (ii) an additional unknown thru measurement of a reciprocal two-port device.

Three independent reflect standards are essential to perform an unknown thru calibration. If a free-space material measurement system can change the separation distance between an antenna and a reflect standard using a precise positioning system [18], it would be easy to realize the reflect standards of the different properties by varying the separation distance. If not, it would be difficult to apply the unknown thru calibration method to a free-space material measurement because discovering independent reflect standards is rather difficult.

Recently, a free-space unknown thru calibration method [19] that uses planar offset shorts as the free-space reflect standard [20, 21] was applied to demonstrate its feasibility in calibrating a free-space material measurement system without a precise positioning system. This paper extends this test of feasibility by adding a detailed description of the calibration procedure and measurement system and analyzing the measurement results. To the best of our knowledge, this study is the first to deal with the realization of the unknown thru calibration method for free-space material measurement.

Section II of this paper briefly describes the use of a planar offset short as a free-space calculable reflect standard and its significance. Section III describes the free-space unknown thru measurement method using planar offset short and its advantages. In Section IV, the free-space unknown thru method is validated by comparing the measurement results with those of the TRL method for two MUTs (glass plates of 2.780 mm and 4.775 mm thickness) using a quasi-optic-based free-space material measurement system in W-band (75–110 GHz). Finally, Section V summarizes this paper.

II. FREE-SPACE CALCULABLE REFLECT STANDARD

Assume that a Gaussian beam, as a localized plane wave, is incident upon the central area of a square metal plate whose size (D) is kept at least three times larger than the waist (d) of the Gaussian beam in order to avoid the edge diffraction effect by the metal plate in quasi-optic-based free-space measurements [22], as shown in Fig. 2 (left). If the central area recedes by an offset (l) (i.e., if the offset short plane is located at a distance from the reference plane, as shown in Fig. 2 (right)), the reflection coefficient of the planar offset short at the reference plane may be expressed by [23]:

$$\Gamma(l) \approx -e^{-2jkl}, \quad (1)$$

where j and k denote the imaginary unit and wavenumber, respectively. Eq. (1) suggests that the planar metal offset short is suitable for utilizing as a free-space calculable reflect standard with the following reflection properties: (i) the magnitude of the reflection coefficient is unity, regardless of the offset and signal frequency, and (ii) its phase is linearly proportional to the offset and frequency.

This paper uses a planar offset short of $125 \text{ mm} \times 125 \text{ mm}$ and 8 mm thickness, as shown in Fig. 2 (right), where the size ($D = 125 \text{ mm}$) of its central area is five times larger than the waist ($d = 25 \text{ mm}$) of the Gaussian beam incident upon the central area in a W-band free-space material measurement system [20, 21].

III. FREE-SPACE UNKNOWN THRU MEASUREMENT

A free-space unknown thru measurement method uses the same calibration theory as a closed guided-wave unknown thru measurement method [16, 17]. However, there are some differences between the two measurement methods in terms of their actual measurements.

1. Two-Port Eight-Term Error Modeling and Its Cascade Matrix Representation

A free-space T/R material measurement system may be

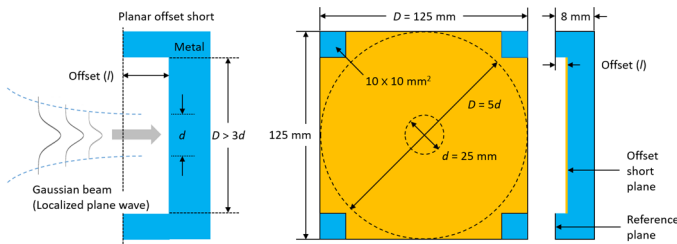


Fig. 2. Planar offset short illuminated by a Gaussian beam: schematic (left) and front and side views (right) of a fabricated planar offset short. Adapted from [21].

represented as a two-port eight-term error model, as shown in Fig. 1. It is composed of the following parts:

- An MUT is placed at the middle of two antennas (#1 and #2) in free space, where both sides (#1 and #2) of the MUT are assigned to the reference planes (#1 and #2) of the material measurement system;
- An ideal scattering parameter measuring instrument for measuring the scattering parameters of the MUT, where the test ports (#1 and #2) of the measuring instrument are connected to the two antennas (#1 and #2); and
- Two error adapters (E_A and E_B) describing the non-ideal parts between the reference plane (#1 and #2) and the test port (#1 and #2), modeled as four systematic errors at each side (#1 and #2) of the MUT, where (E_{DF}, E_{SF}, E_{RF}) and (E_{DR}, E_{SR}, E_{RR}) denote the one-port systematic error corresponding to directivity, port match, and reflection tracking, respectively, on each error adapter, while α and β are the systematic errors related to transmission tracking on each error adapter. Effectively, eight systematic errors can be determined during the calibration of the material measurement system.

The eight-term error model may be expressed in the cascade matrix by:

$$[T_m] = [A][T][B], \quad (2)$$

where $[T_m]$ and $[T]$ denote the cascade matrices of the measured scattering matrix $[S_m]$ and the real scattering matrix $[S]$ of an MUT, respectively, while $[A]$ and $[B]$ represent the cascade matrices of the scattering matrix of error adapters E_A and E_B , respectively. $[T_m]$, $[A]$, and $[B]$ in Eq. (2) can, therefore, be expressed as:

$$[T_m] = \frac{1}{S_{21,m}} \begin{bmatrix} \Delta_{S,m} & S_{11,m} \\ -S_{22,m} & 1 \end{bmatrix}, \quad (3)$$

$$[A] = \frac{1}{\alpha} \begin{bmatrix} \Delta_A & E_{DF} \\ -E_{SF} & 1 \end{bmatrix}, \quad (4)$$

$$[B] = \frac{\beta}{E_{RR}} \begin{bmatrix} \Delta_B & E_{SR} \\ -E_{DR} & 1 \end{bmatrix}, \quad (5)$$

where $S_{ij,m}$ denotes the element of $[S_m]$, $\Delta_{S,m} = -\det[S_m]$, $\Delta_A = -\det[E_A]$, and $\Delta_B = -\det[E_B]$. Substituting Eqs. (4) and (5) in Eq. (2) leads to $[T_m]$ being expressed in only seven unknowns—(E_{DF}, E_{SF}, E_{RF}), (E_{DR}, E_{SR}, E_{RR}), and β/α —which can be denoted as:

$$[T_m] = \frac{\beta}{\alpha} \frac{1}{E_{RR}} \begin{bmatrix} \Delta_A & E_{DF} \\ -E_{SF} & 1 \end{bmatrix} [T] \begin{bmatrix} \Delta_B & E_{SR} \\ -E_{DR} & 1 \end{bmatrix}. \quad (6)$$

From Eq. (6), $[T]$ may be expressed as:

$$[T] = \frac{\alpha}{\beta} \frac{1}{E_{RF}} \begin{bmatrix} 1 & -E_{DF} \\ E_{SF} & \Delta_A \end{bmatrix} [T_m] \begin{bmatrix} 1 & -E_{SR} \\ E_{DR} & \Delta_B \end{bmatrix}. \quad (7)$$

The two one-port systematic errors— (E_{DF}, E_{SF}, E_{RF}) and (E_{DR}, E_{SR}, E_{RR}) —can be determined by performing the one-port calibration at each reference plane (#1 and #2) of the material measurement system. From Eq. (6), the remaining unknown α/β may be expressed as:

$$\frac{\alpha}{\beta} = \pm \sqrt{\frac{S_{21,m} E_{RF}}{S_{12,m} E_{RR}}}, \quad (8)$$

by using the property that the determinant of the cascade matrix of a reciprocal two-port device is equal to unity. The sign ambiguity in Eq. (8) can be solved by comparing the calculated and measured transmission coefficients of the reciprocal two-port device.

According to the unknown thru calibration theory [16, 17], an unknown thru standard (i.e., a reciprocal two-port device) used for determining α/β does not need to be known or perfect. However, the unknown thru standard must be reciprocal, must be aware of the phase within a quarter wavelength, and is additionally recommended to have a transmission loss less than 40 dB for accurate determination of α/β during calibration. If a DUT meets these requirements, it can be considered the unknown thru standard.

2. Procedure of Free-Space Unknown Thru Calibration and Measurement

The steps to conduct a free-space unknown thru calibration and measurement are as follows:

- Step 1. Determining the one-port systematic error (E_{DF}, E_{SF}, E_{RF}) at reference plane #1 by performing the one-port calibration with three free-space reflect standards;
- Step 2. Repeating Step 1 to determine the other one-port systematic error (E_{DR}, E_{SR}, E_{RR}) at reference plane #2, which is situated away from reference plane #1 due to the thickness of an MUT; and
- Step 3. Determining the remaining unknown α/β by performing an unknown thru measurement. If the MUT, which is placed between the two reference planes (#1 and #2), meets the requirements of the unknown thru standard, it is used as the unknown thru standard in the calibration. Otherwise, an air gap with the same thickness as the MUT is used as the unknown thru standard.
- Step 4. If an MUT meets the requirements of the unknown thru standard, its scattering parameters are measured using the calibrated free-space material measurement system without changing the calibration setup. Otherwise, the scattering parameters of the MUT are measured by replacing the air gap with the MUT.

IV. FREE-SPACE UNKNOWN THRU MEASUREMENT

RESULTS

The scattering parameters of two reciprocal MUTs (glass

plates of 2.780 mm and 4.775 mm thickness) are measured by using a quasi-optic-based free-space material measurement system [18], as shown in Fig. 3, which is calibrated by the free-space unknown thru and TRL methods for 500 Hz IF bandwidth and 801 frequency sweep points in W-band.

The quasi-optic-based free-space material measurement system is composed of the following parts:

- A millimeter-wave scattering parameters measuring instrument consisting of a VNA and two frequency extenders; and
- A quasi-optic-based free-space instrument composed of two linearly movable benches with an MUT holder between them, where each bench has a Gaussian beam forming corrugated horn antenna and an ellipsoidal refocusing mirror and is capable of independently changing the separation distance between the bench and the MUT holder for supporting TRL calibration.

The free-space unknown thru and TRL calibrations are performed as follows:

- Free-space unknown thru calibration is carried out by measuring: (i) the one-port calibration at the reference planes corresponding to both sides of the MUT using three planar offset "Shorts" ($l = 0$ mm, 0.550 mm ($\lambda/6$), 1.100 mm ($2\lambda/6$)), generating a phase difference of 120° between the reflection coefficients of the planar shorts at the center frequency of the W-band [21], and (ii) the "unknown Thru" after inserting an MUT between the two reference planes. Since the two reference planes (#1 and #2) of the measurement system are fixed during the calibration, movement of the RF cable can be avoided. Meanwhile, the reflection coefficients of the three reflect standards used in the one-port calibration should not be equal to each other, and should be distributed as far as possible from each other on the complex reflection plane in the operating frequency range. The theoretical magnitude of the reflection coefficient of the three planar offset shorts (0 mm, 0.550 mm, and 1.100 mm) is unity, regardless of the offset and signal frequency. The theoretical phase of the planar flush (0 mm offset) is -180° , irrespective of the signal frequency, while that of the two

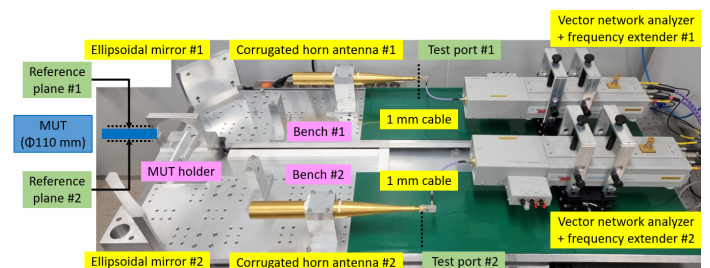


Fig. 3. Quasi-optic-based free-space material measurement system in W-band.

planar offset shorts is changed from 80.96° to 34.75° for the 0.550 mm offset, and from -18.07° to -110.51° for the 1.100 mm offset in the W-band [21]. Therefore, the three planar offset shorts can be used as independent reflect standards in the one-port calibration; and

- TRL calibration is carried out by measuring: (i) the zero-length "Thru" by directly connecting the reference planes (#1 and #2), (ii) the "Reflect" using a metal plate (4.671 mm thickness) inserted between the two reference planes, which are consequently separated by the plate thickness, and (iii) the "Line" of a quarter-wavelength delay (0.82 mm length) in the air, which separates the reference planes. Since reference plane #1 of the measurement system is fixed during the calibration, movement of the RF cable is inevitable.

The scattering parameters of a glass plate of 2.780 mm thickness are measured five times to compare the repeatability of the measured results obtained from the free-space unknown thru (solid symbol) and TRL (open symbol) calibration methods, as shown in Fig. 4. The average and standard deviation of the measured magnitude and phase data exhibit some peaks in the measured data due to multiple reflections between the MUT and antennas as well as within the MUT itself, which is inherent in a free-space material measurement.

Usually, these multiple reflections can be removed by implementing smoothing (i.e., moving average) and time-gating of the measured data as post-signal processing. The application of 10-point smoothing to the measured data, as depicted in Fig. 4, reveals that (i) the effects of the multiple reflections on the magnitude and phase data are drastically reduced, (ii) the averages of the magnitude and phase obtained from the two calibration methods agree with each other, as shown in Fig. 5(a) and 5(c), which validates the free-space unknown thru calibration method, and (iii) the standard deviations of the magnitude and phase obtained from the TRL calibration method are more favorable than those obtained from the unknown thru method, as shown in Fig. 5(b) and 5(d).

Increasing the thickness of the glass plate from 2.780 mm to 4.775 mm results in a reduction of the multiple reflections on the measured data, a shorter period of the magnitude of reflection and transmission coefficients, and a steeper phase slope of the transmission coefficient, as shown in Fig. 6.

The measurement results suggest that the TRL calibration method has better reproducibility (i.e., standard deviation) than the unknown thru calibration method, which involves complicated measurement procedures compared to the TRL calibration method, as shown in Figs. 5 and 6. However, discrepancies between the measured results can be improved by the accurate alignment and placement of the reflect standard and the MUT in the material measurement.

Compared to conventional free-space measurement methods,

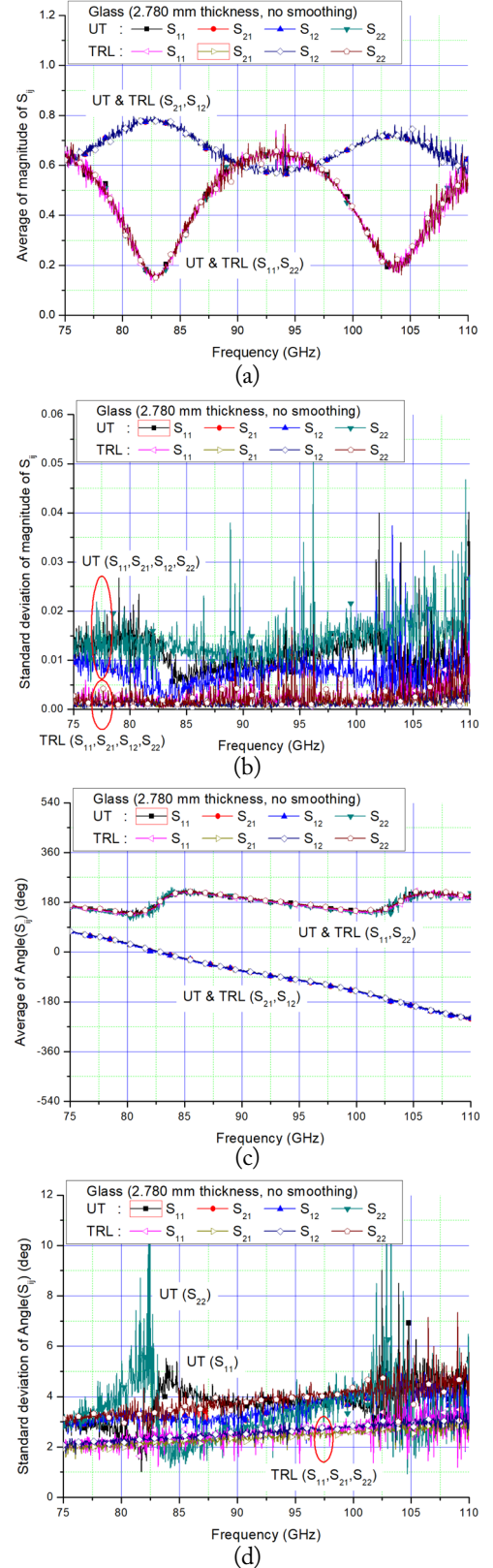


Fig. 4. Average and standard deviation of the magnitude and phase of the scattering parameters, measured five times, of a glass of 2.780 mm thickness obtained from free-space unknown thru (UT, solid symbol) and TRL (open symbol) calibration methods without any smoothing process: (a) average of the magnitude, (b) standard deviation of the magnitude, (c) average of the phase, and (d) standard deviation of the phase.

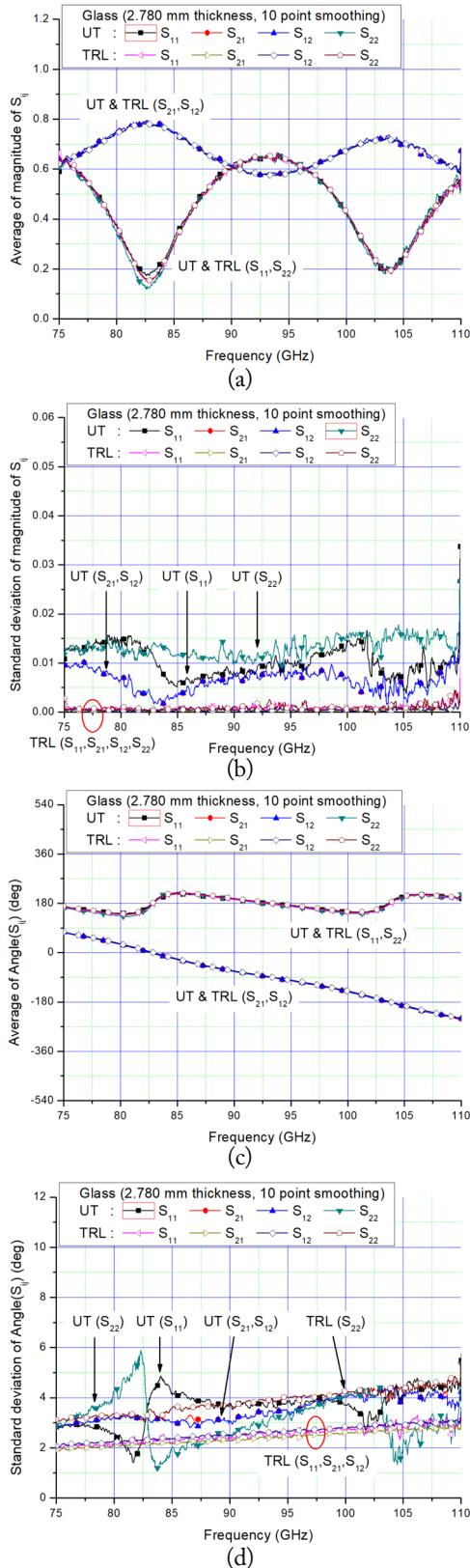


Fig. 5. Average and standard deviation of the magnitude and phase of the scattering parameters, measured five times, of a glass of 2.780 mm thickness obtained from free-space unknown thru (UT, solid symbol) and TRL (open symbol) calibration methods with a 10-point smoothing process: (a) average of the magnitude, (b) standard deviation of the magnitude, (c) average of the phase, and (d) standard deviation of the phase.

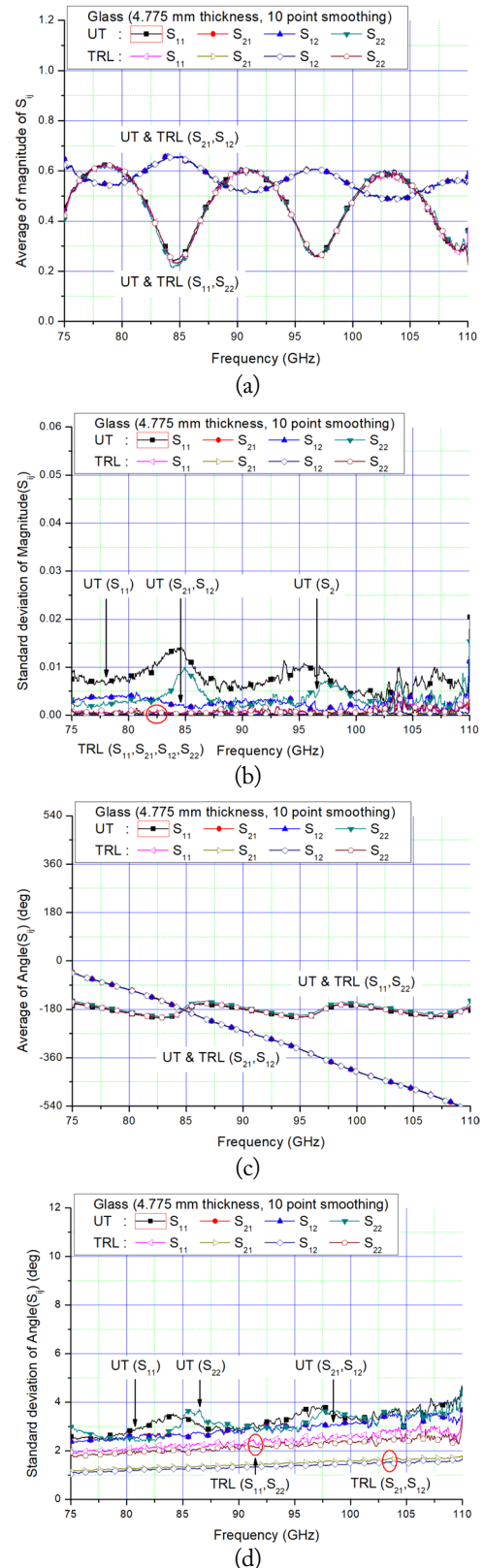


Fig. 6. Average and standard deviation of the magnitude and phase of the scattering parameters, measured five times, of a glass of 4.775 mm thickness obtained from free-space unknown thru (UT, solid symbol) and TRL (open symbol) calibration methods with a 10-point smoothing process: (a) average of the magnitude, (b) standard deviation of the magnitude, (c) average of the phase, and (d) standard deviation of the phase.

such as the TRL, TRM, and GRL methods, the free-space unknown thru measurement method using plane offset shorts has the advantages of not using the followings:

- A precise positioning system and movement of RF cables in the TRL method.
- A well-matched broadband EM absorber in the TRM method.
- A time-gating measurement and a planar metal plate that is as thick as a MUT during calibration and a de-embedding process to compensate for the effect of the difference in thickness of the planar metal plate and the MUT in the GRL measurement method.

V. CONCLUSION

Material characterization requires the proper calibration of a material measurement system. This study describes a free-space unknown thru measurement method using three independent planar metal offset shorts for calibrating a free-space material measurement system.

The scattering parameters of two glass plates, with 2.780 mm and 4.775 mm thickness, obtained from conducting the free-space unknown thru and TRL measurement methods, agree with each other in W-band. This implies that the free-space unknown thru measurement method using planar offset shorts can be considered an affordable and effective alternative to conventional free-space material measurement methods.

This study further highlights that the precision fabrication of a planar metal offset short is more feasible and inexpensive than building a precision positioning system in a free-space material measurement system. This measurement method can be used even for a high-frequency range that the fabrication accuracy of a planar metal offset short finds acceptable. This method can be helpful for microwave, millimeter-wave, and sub-millimeter-wave material measurements.

This study is supported by the Technology Innovation Program (No. 20016225, Development and Dissemination on National Standard Reference Data) funded by the Ministry of Trade, Industry & Energy, Republic of Korea, and the Korea Research Institute of Standards and Science (No. KRIS-2021-21011008) under the project "Development of safety measurement technology for major infrastructures."

REFERENCES

- [1] R. S. Hassan, S. I. Park, A. K. Arya, and S. Kim, "Continuous characterization of permittivity over a wide bandwidth using a cavity resonator," *Journal of Electromagnetic Engineering and Science*, vol. 20, no. 1, pp. 39-44, 2020.
- [2] G. Kim and B. Lee, "Synthesis of bulk medium with negative permeability using ring resonators," *Journal of Electromagnetic Engineering and Science*, vol. 16, no. 2, pp. 67-73, 2016.
- [3] J. S. Kang, J. H. Kim, K. Y. Kang, D. H. Yoon, and S. W. Park, "Specular reflectance measurements of dielectric plates in millimeter frequency range," *Journal of Electromagnetic Engineering and Science*, vol. 18, no. 2, pp. 78-87, 2018.
- [4] A. M. Nicolson and G. F. Ross, "Measurement of the intrinsic properties of materials by time-domain techniques," *IEEE Transactions on Instrumentation and Measurement*, vol. 19, no. 4, pp. 377-382, 1970.
- [5] W. B. Weir, "Automatic measurement of complex dielectric constant and permeability at microwave frequencies," *Proceedings of the IEEE*, vol. 62, no. 1, pp. 33-36, 1974.
- [6] J. Baker-Jarvis, E. J. Vanzura, and W. A. Kissick, "Improved technique for determining complex permittivity with the transmission/reflection method," *IEEE Transactions on Microwave Theory and Techniques*, vol. 38, no. 8, pp. 1096-1103, 1990.
- [7] E. J. Vanzura, J. R. Baker-Jarvis, J. H. Grosvenor, and M. D. Janezic, "Intercomparison of permittivity measurements using the transmission/reflection method in 7-mm coaxial transmission lines," *IEEE Transactions on Microwave Theory and Techniques*, vol. 42, no. 11, pp. 2063-2070, 1994.
- [8] D. K. Ghodgaonkar, V. V. Varadan, and V. K. Varadan, "Free-space measurement of complex permittivity and complex permeability of magnetic materials at microwave frequencies," *IEEE Transactions on Instrumentation and Measurement*, vol. 39, no. 2, pp. 387-394, 1990.
- [9] D. Bourreau, A. Peden, and S. Le Maguer, "A quasi-optical free-space measurement setup without time-domain gating for material characterization in the W-band," *IEEE Transactions on Instrumentation and Measurement*, vol. 55, no. 6, pp. 2022-2028, 2006.
- [10] A. Kazemipour, M. Hudlicka, S. K. Yee, M. A. Salhi, D. Allal, T. Kleine-Ostmann, and T. Schrader, "Design and calibration of a compact quasi-optical system for material characterization in millimeter/submillimeter wave domain," *IEEE Transactions on Instrumentation and Measurement*, vol. 64, no. 6, pp. 1438-1445, 2015.
- [11] S. Iyer, C. C. Cheng, C. Kim, and A. Abbaspour-Tamijani, "Compact Gaussian beam system for S-parameter characterization of planar structures at millimeter-wave frequencies," *IEEE Transactions on Instrumentation and Measurement*, vol. 59, no. 9, pp. 2437-2444, 2010.
- [12] D. K. Rytting, "Network analyzer accuracy overview," in *Proceedings of the 58th ARFTG Microwave Measurement Conference*, San Diego, CA, 2001, pp. 1-13.

- [13] Keysight Technologies, "Specifying calibration standards and kits for Keysight vector network analyzers," 2019 [Online]. Available: <https://www.keysight.com/kr/ko/assets/7018-01375/application-notes/5989-4840.pdf>.
- [14] D. V. Blackham, "Free space characterization of materials," in *Proceedings of the 5th Symposium of the Antenna Measurement Techniques Association (AMTA)*, Dallas, TX, 1993, pp. 58-60.
- [15] P. Bartley and S. Begley, "Improved free-space S-parameter calibration," in *Proceedings of 2005 IEEE Instrumentation and Measurement Technology Conference*, Ottawa, Canada, 2005, pp. 372-375.
- [16] A. Ferrero and U. Pisani, "Two-port network analyzer calibration using an unknown 'thru'," *IEEE Microwave and Guided Wave Letters*, vol. 2, no. 12, pp. 505-507, 1992.
- [17] K. Wong, "The 'unknown thru' calibration advantage," in *Proceedings of the 63rd ARFTG Microwave Measurement Conference*, Fort Worth, TX, 2004, pp. 73-81.
- [18] J. S. Kang, J. H. Kim, C. Cho, and D. C. Kim, "W-band permittivity measurements using a free-space material measurement technique," *The Journal of Korean Institute of Electromagnetic Engineering and Science*, vol. 24, no. 3, pp. 253-258, 2013.
- [19] J. S. Kang, "SOLR calibration using planar offset short in free-space material measurement," in *Proceedings of the 42nd Symposium of the Antenna Measurement Techniques Association (AMTA)*, Newport, RI, 2020, pp. 1-4.
- [20] J. S. Kang, J. H. Kim, and K. S. Min, "W-band free-space planar offset short," in *Proceedings of 2019 International Symposium on Antennas and Propagation (ISAP)*, Xi'an, China, 2019, pp. 1-2.
- [21] J. S. Kang and J. H. Kim, "Planar offset short applicable to the calibration of a free-space material measurement system in W-band," *Journal of Electromagnetic Engineering and Science*, vol. 21, no. 1, pp. 51-59, 2021.
- [22] P. F. Goldsmith, *Quasioptical Systems*. London, UK: IEEE Press, 1998.
- [23] D. M. Pozar, *Microwave Engineering*. Reading, MA: Addison-Wesley, 1990.

Jin-Seob Kang



received his B.S. degree in Electronic Engineering from Hanyang University, Seoul, Korea, in 1987, and his M.S. and Ph.D. degrees in Electrical and Electronic Engineering from Korea Advanced Institute of Science and Technology (KAIST), Daejeon, Korea, in 1989 and 1994, respectively. He was a postdoctoral research associate with the Department of Electrical and Computer Engineering, University

of Illinois at Urbana-Champaign in 1995, and an assistant professor with the School of Electrical and Electronic Engineering, Chungbuk National University, Korea, from 1996 to 1997. He joined the Korea Research Institute of Standards and Science (KRISS), Daejeon, in 1998 and currently serves as a principal research scientist. He has been working on electromagnetic (EM) measurement standards, material measurements, material parameter reference standards, (sub-)mm-wave EM measurements, and non-destructive testing.

Reduced-Size Series-Fed Two-Dipole Endfire Antenna

Heesu Wang¹ · Yong Bae Park^{1,2} · Ikmo Park^{1,*}

Abstract

The conventional series-fed endfire dipole antenna has a wide impedance bandwidth and is inexpensive to manufacture. However, it has a disadvantage: its size is large because of the large inter-dipole spacing, which is required to satisfy the endfire condition for good antenna radiation characteristics. Here, we propose a two-dipole endfire antenna with a reduced size. The miniaturized endfire antenna was designed using a meander line to reduce the interdipole spacing while ensuring that the endfire condition was satisfied. Furthermore, the overall width of the antenna was reduced using a bent dipole and a corrugated ground plane. The electrical size of the proposed antenna was only $0.33\lambda_0 \times 0.33\lambda_0 \times 0.014\lambda_0$ at a center frequency of 5 GHz, its -10 dB impedance bandwidth was 4.47–5.72 GHz (24.5%), and the gain at the center frequency was 5.9 dBi.

Key Words: C-Band Antenna, Dipole Antenna, Endfire Antenna, Miniaturized Antenna, Printed Dipole Antenna.

I. INTRODUCTION

Recently, wireless communication devices have been gradually miniaturized, and this has led to a continuous increase in demand for small antennas for civilian and military purposes in the wireless communication market [1–6]. Owing to this demand, various types of small antennas are being studied. Conventional printed series-fed endfire dipole antennas are easy and inexpensive to manufacture, and they can be implemented with a wide bandwidth; therefore, they are popular in the wireless communication market [7–12]. However, owing to the large size of the endfire dipole antenna, which results from the dipole length and the interdipole spacing required to satisfy the endfire condition, it is difficult to use a conventional endfire dipole antenna for small wireless communication devices. To overcome this problem, researchers have conducted studies on the miniaturization of dipole arms [13–25]. The electrical length of a conventional dipole is half the wavelength of the center frequency. To reduce

the electrical length of the dipole, researchers have studied many types of meander dipole [13–17], bent dipole, and folded dipole structures [18–25]. Furthermore, small zeroth-order resonant dipole antennas with composite right-/left-handed metamaterial structures have been proposed [26, 27]. Although the size of the dipole arm of the endfire dipole antenna can be reduced by using these structures, the phase difference between adjacent dipoles should be between 90° and 180° to satisfy the endfire condition. In a conventional endfire dipole antenna, this phase difference is determined by the interdipole distance. It is difficult to reduce the size of the antenna since the interdipole distance is large [28, 29].

In this study, a meander line was used for the transmission line connecting the dipoles of a series-fed endfire dipole antenna to satisfy the endfire condition while reducing interdipole spacing. Furthermore, a bent dipole and a corrugated ground plane were used to reduce the overall width of the antenna.

Manuscript received January 9, 2022 ; Revised May 6, 2022 ; Accepted June 1, 2022. (ID No. 20220109-006J)

¹Department of Electrical and Computer Engineering, Ajou University, Suwon, Korea.

²Department of AI Convergence Network, Ajou University, Suwon, Korea.

*Corresponding Author: Ikmo Park (e-mail: ipark@ajou.ac.kr)

This is an Open-Access article distributed under the terms of the Creative Commons Attribution Non-Commercial License (<http://creativecommons.org/licenses/by-nc/4.0>) which permits unrestricted non-commercial use, distribution, and reproduction in any medium, provided the original work is properly cited.

© Copyright The Korean Institute of Electromagnetic Engineering and Science.

II. TWO-ELEMENT DIPOLE ANTENNA

A conventional series-fed two-dipole endfire antenna was designed by connecting two straight dipoles in series with a parallel strip transmission line. The dipoles were matched using a quarter-wave impedance transformer, and their lengths were chosen to be slightly different to achieve a large impedance bandwidth [30, 31]. Fig. 1 shows the geometry of the conventional two-dipole antenna. The substrate used for the antenna was Rogers RO4003C ($\epsilon_r = 3.38$ and $\tan\delta = 0.0027$), and its thickness was 0.8128 mm. The -10 dB impedance bandwidth of the conventional dipole antenna is 4.48–5.56 GHz, and its gain at a center frequency of 5 GHz is 5.9 dBi. The ANSYS High-Frequency Structure Simulator (HFSS) was used to design and optimize the conventional series-fed two-dipole endfire antenna. The optimized design parameters were $W = 30$ mm, $L_g = 10$ mm, $W_f = 1.8$ mm, $L_{d1} = 25$ mm, $L_{d2} = 19$ mm, $S_{d1} = 13$ mm, $S_{d2} = 17$ mm, $W_d = 0.5$ mm, $W_r = 0.5$ mm, $W_q = 0.3$ mm, $L_q = 6$ mm, $L = 41$ mm, and $S = 1$ mm.

Fig. 2 shows the antenna structure that satisfies the endfire

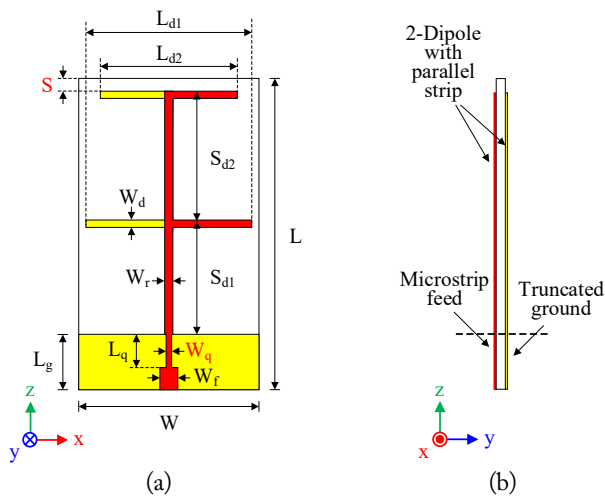


Fig. 1. Conventional two-element dipole antenna: (a) front view and (b) side view.

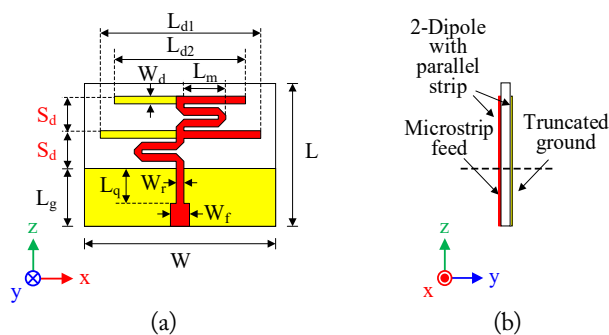


Fig. 2. Spacing reduced printed two-dipole antenna: (a) front view and (b) side view.

condition with reduced spacing; it comprises a meander parallel stripline, two dipoles, and a ground plane. The spacing between the dipoles and that between the dipoles and the ground plane are the same. In a conventional two-dipole antenna, they are connected with a straight transmission line. When the spacing is changed, the length of the transmission line changes; thus, the phase difference also changes. Therefore, the antenna gain is reduced at around the center frequency. To reduce the spacing S_d and to overcome the gain reduction due to the phase difference change, a meander transmission line was used instead of a straight transmission line to connect the radiating elements and the radiating element to the ground plane. The gain in the vicinity of the center frequency was maximized by adjusting the length of the meander line, L_{pd} , on the basis of interdipole spacing. Fig. 3 shows the characteristics of the antenna for different interdipole spacings. The interdipole spacing S_d was simulated to have values between 3 mm and 12 mm. Fig. 3(a) shows the variation of the reflection coefficient with the frequency for different dipole spacings. The antenna showed good impedance bandwidth characteristics. However, for $S_d = 3$ mm, the distance between the meander transmission lines was too narrow, and the characteristic impedance of the transmission

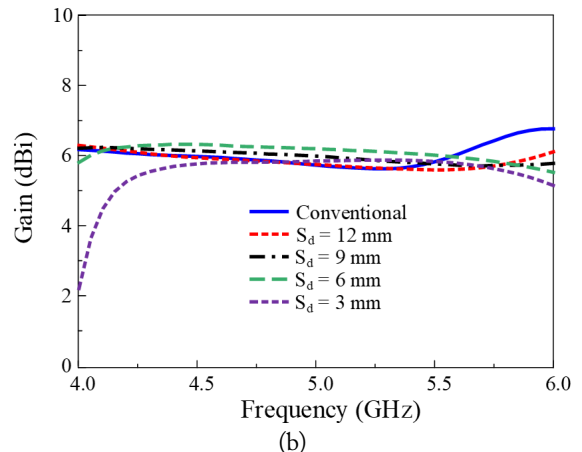
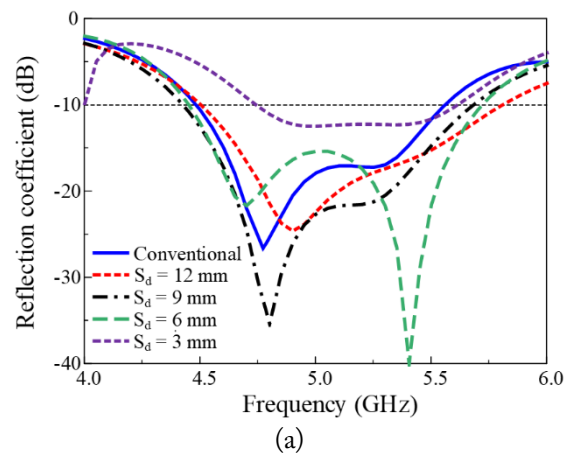


Fig. 3. Effect of the dipole spacing S_d : (a) reflection coefficient and (b) gain.

line was changed, which considerably reduced the impedance bandwidth. Fig. 3(b) shows the gain characteristics of the antenna; the gain around the center frequency was apparently similar, even if the spacing was decreased. The antenna characteristics for different dipole spacings are presented in Table 1. The minimum dipole spacing at which the antenna’s performance was maintained was 4.5 mm. The overall electrical length of the antenna with reduced spacing was $0.33\lambda_0$, which was about 48.5% of the overall length of the conventional antenna. The impedance bandwidth of the reduced-spacing antenna was 4.53–5.76 GHz, and the gain was 6.2 dBi at the center frequency. The design parameters of the optimized antenna obtained using the HFSS were $W = 30$ mm, $L_g = 10$ mm, $W_f = 1.8$ mm, $L_{d1} = 25$ mm, $L_{d2} = 19$ mm, $S_d = 4.5$ mm, $L_{pd} = 5$ mm, $W_d = 0.5$ mm, $W_r = 0.5$ mm, $W_q = 0.5$ mm, $L_q = 6$ mm, $L = 20$ mm, and $S = 1$ mm.

Fig. 4 shows a reduced-spacing antenna with a bent dipole as the radiation element. Owing to the length of the bent portion, L_b , the electric length of the dipole increased, which resulted in a lower center frequency. A parametric study was performed according to the L_b change. Fig. 5 shows the variation in the antenna characteristics with L_b . As L_b increased, the resonant frequency of the antenna decreased, as expected, and the frequency of the peak gain also decreased.

Table 1. Characteristics of two-element dipole antennas with different spacing

	Conven- tional	$S_d =$ 12 mm	$S_d =$ 9 mm	$S_d =$ 6 mm	$S_d =$ 3 mm
–10 dB IBW (GHz)	4.48–5.56 (21.6%)	4.50–5.81 (26.2%)	4.42–5.68 (25.2%)	4.45–5.72 (25.4%)	4.74–5.61 (17.4%)
Gain at 5 GHz (dBi)	5.9	5.8	6.0	6.2	5.9
Antenna length (λ_0)	0.68	0.58	0.48	0.38	0.28

IBW = impedance bandwidth.

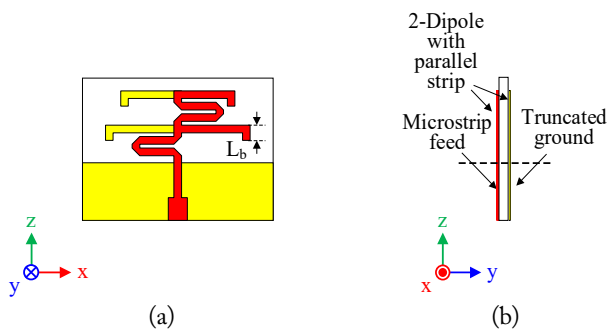


Fig. 4. Spacing reduced antenna with bent dipoles: (a) front view and (b) side view.

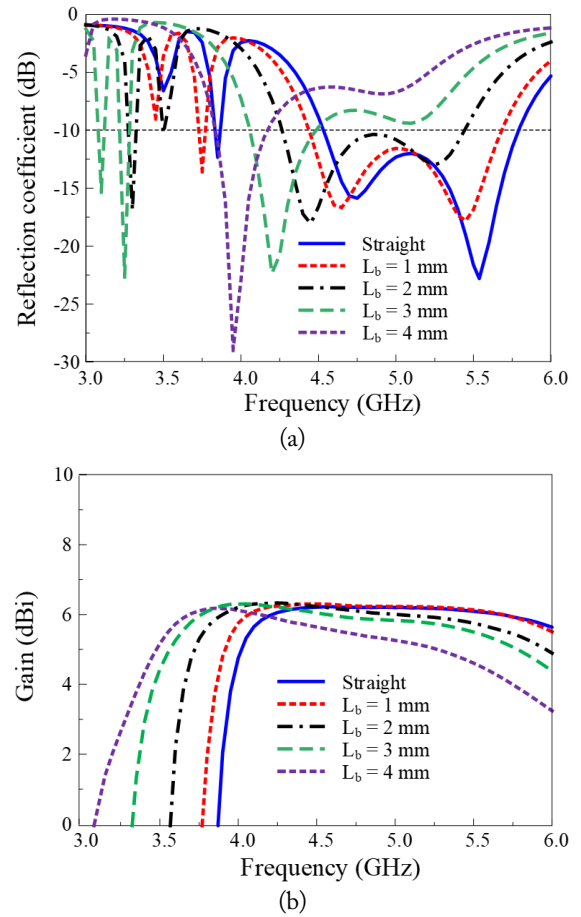


Fig. 5. Effect of bent length L_b : (a) reflection coefficient and (b) gain.

Fig. 6 shows an antenna structure with a corrugated ground plane. The conventional truncated ground plane serves as a reflector, and the ground plane width W strongly affects the antenna’s performance. When the width of the ground plane decreases, the front-to-back ratio and gain of the antenna decrease.

A corrugated ground plane acts as a magnetic ground, and the size of the ground plane significantly decreases with a slight reduction in gain [32]. Corrugation lengthens the edge of the ground plane because the current is concentrated at the edge of the conductor. Therefore, a small corrugated ground plane can

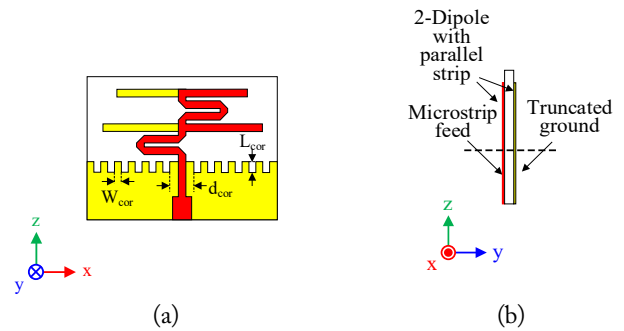


Fig. 6. Spacing reduced antenna with corrugated ground plane: (a) front view and (b) side view.

perform the same role as a relatively large non-corrugated ground plane. Fig. 7 shows the antenna characteristics at different corrugation depths of a fixed-size ground plane. When the corrugation depth was 3 mm, the impedance bandwidth was maximum, and the center frequency apparently decreased. As shown in Fig. 7(b), the antenna gain decreased as the corrugation depth increased. However, as shown in Fig. 7(c), no significant difference in antenna efficiency was observed within the impedance bandwidth. Fig. 8 shows the surface current distribution

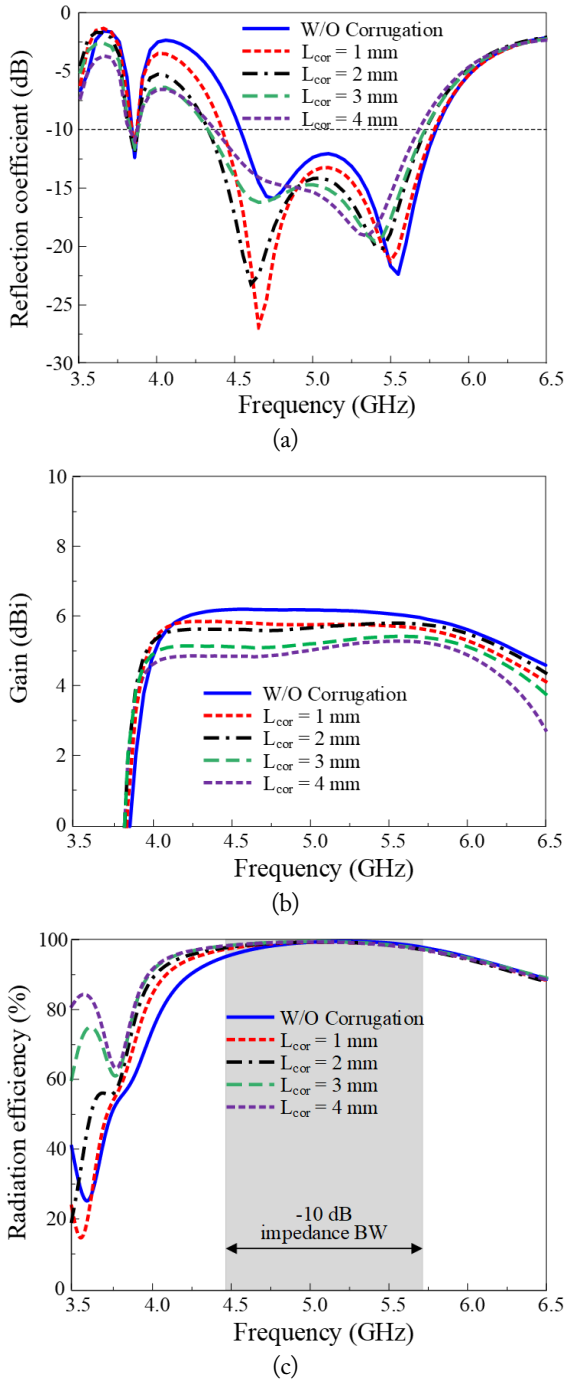


Fig. 7. Effect of corrugation depth L_{cor} : (a) reflection coefficient, (b) gain, and (c) radiation efficiency.

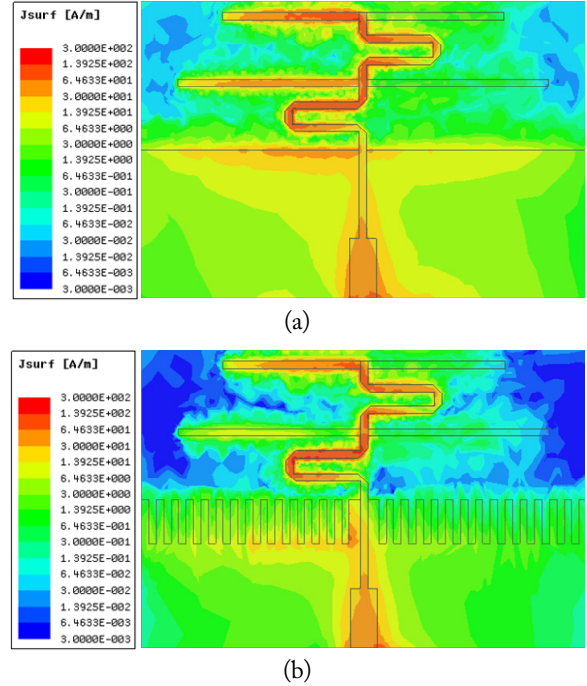


Fig. 8. Surface current distributions at 5 GHz: (a) without corrugation and (b) with corrugation of $L_{cor} = 3$ mm.

of the antenna at 5 GHz without corrugation and the antenna with a 3-mm corrugation depth. Given that the antenna without corrugation was close to the meander line and to the ground plane, a large amount of current was distributed at the edge of the ground plane. In contrast, the antenna with corrugation distributed a relatively small amount of current at the edge of the ground plane due to the effect of corrugation. Most of the current in an antenna with corrugation is concentrated in the dipole and the transmission line, thereby widening the antenna beamwidth and reducing gain.

III. SIMULATION AND MEASUREMENT

Section II shows the antenna structure used to reduce dipole spacing, dipole width, and ground plane width. By combining these three structures, we designed a small two-dipole endfire antenna in which the interdipole spacing, dipole length, and ground plane width were reduced.

Fig. 9 shows the proposed antenna structure. The antenna size was $0.33\lambda_o \times 0.33\lambda_o \times 0.014\lambda_o$, which was 32% of the size of a conventional series-fed two-dipole antenna. The optimized design parameters of the antenna obtained using the HFSS were $W = 20$ mm, $L_g = 10$ mm, $W_f = 1.8$ mm, $L_{d1} = 18$ mm, $L_{d2} = 13$ mm, $S_d = 4.5$ mm, $L_{pd} = 5$ mm, $W_d = 0.5$ mm, $W_r = 0.5$ mm, $W_q = 0.5$ mm, $L_q = 6$ mm, $L_b = 3.5$ mm, $W_{cor} = 0.5$ mm, $L_{cor} = 3$ mm, $d_{cor} = 0.5$ mm, $L = 20$ mm, and $S = 1$ mm.

Fig. 10 shows a comparison between the optimized reduced-size antenna and the conventional antenna. The impedance band-

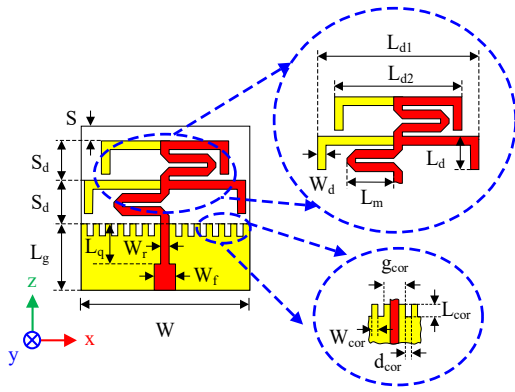


Fig. 9. Proposed two-element dipole antenna.

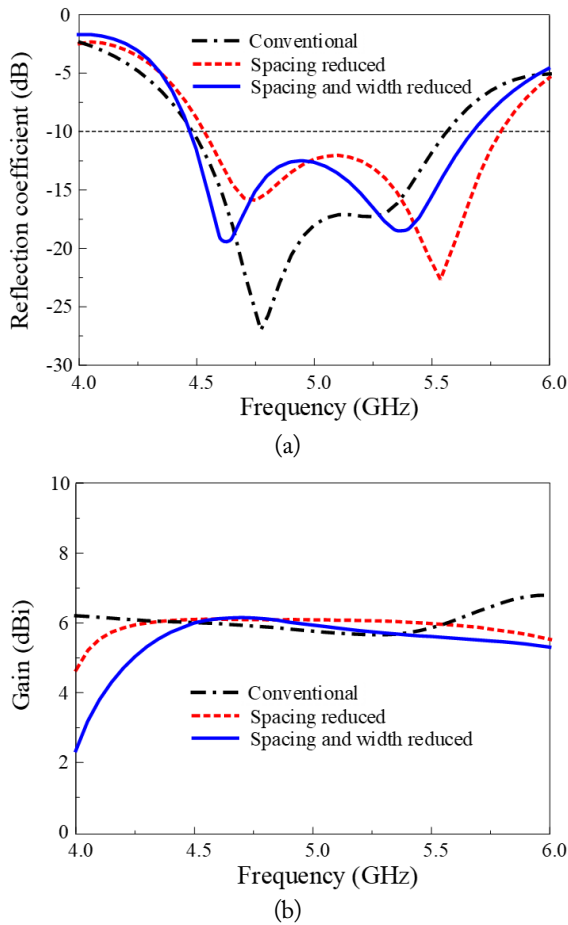


Fig. 10. Comparison of conventional and proposed antenna: (a) reflection coefficient and (b) gain.

width of the proposed antenna structure was 4.47–5.68 GHz, which was wider than that of the conventional antenna (4.48–5.56 GHz) by 0.13 GHz. The gain at the center frequency was 6.0 dBi, which was almost similar to that of the conventional antenna (5.9 dBi).

Fig. 11 shows the fabricated antenna. A Rohde & Schwarz ZVA67 vector network analyzer was used for reflection coefficient measurement, and an MTG anechoic chamber was used for radiation pattern measurement. Fig. 12 shows the simulated

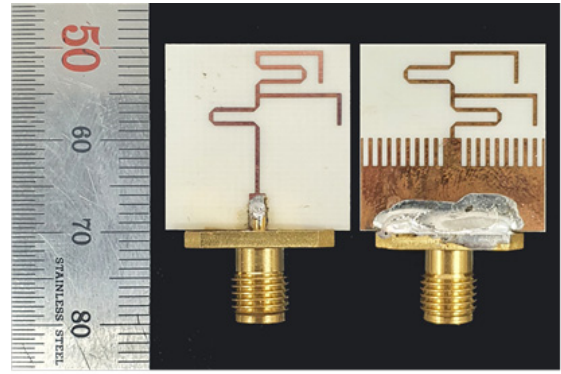


Fig. 11. Photograph of the fabricated antenna.

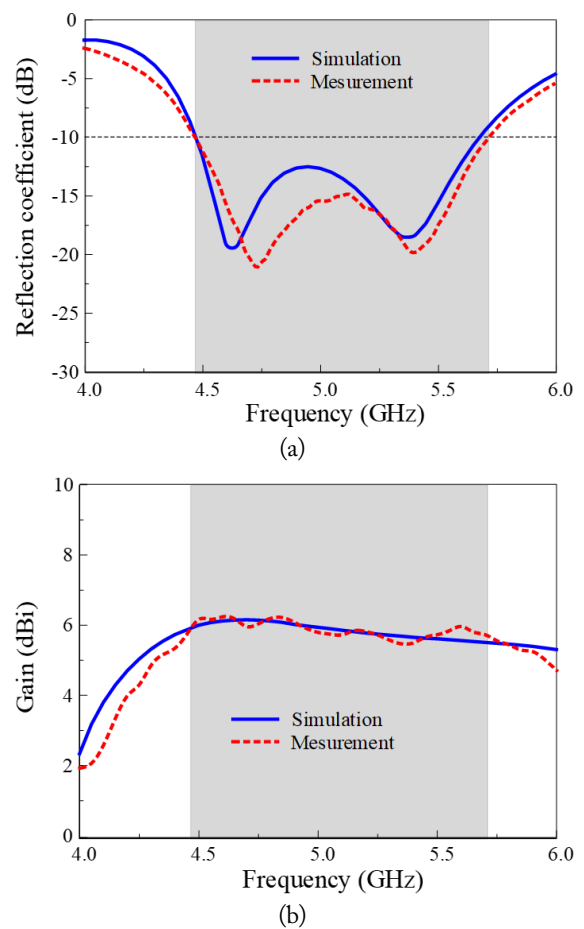


Fig. 12. Simulation and measurement of the proposed antenna: (a) reflection coefficient and (b) gain.

and measured reflection coefficients and gains. Fig. 12(a) shows the reflection coefficient. The measured -10 dB impedance bandwidth was 4.47–5.72 GHz, almost identical to the impedance bandwidth in the simulation. Fig. 12(b) shows the gain. The gain measured at 5 GHz was 5.9 dBi, which was almost identical to that in the simulation. Fig. 13 shows the normalized radiation pattern of the antenna at 5 GHz. The simulated and measured values of the half-power beamwidth in the xz -plane were 80° and 94° , respectively, and those in the yz -plane were

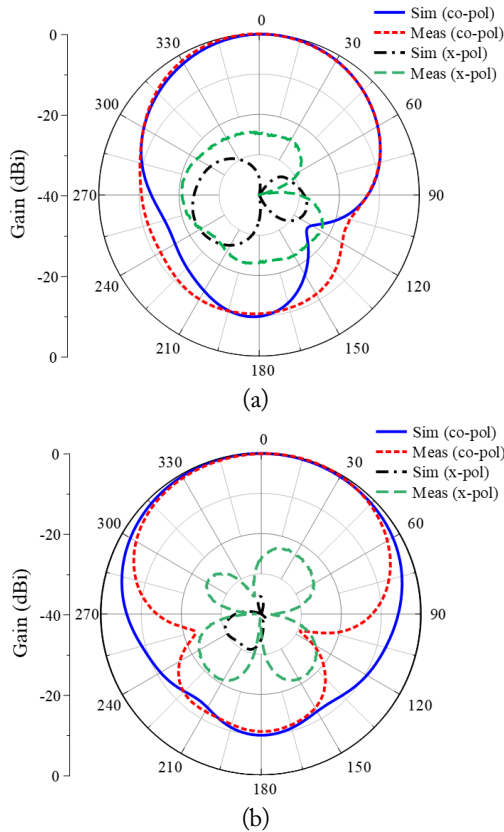


Fig. 13. Simulation and measurement of radiation patterns at 5 GHz: (a) xz -plane and (b) yz -plane.

139° and 122°, respectively. The measured value of the x-pol level was slightly larger than the simulated value, but the x-pol level was lower than -20 dB. The measured co-pol level and radiation pattern were similar to those in the simulation.

The characteristics of the proposed antenna and the existing endfire antennas with two radiation elements were compared. An endfire antenna using two dipoles of the same size is presented in [8]. Given that the antenna has a large ground plane and that both dipoles operate near the center frequency, the gain is relatively high at 7 dBi. However, the bandwidth of the antenna was only 5.0%. An antenna with an integrated balun that connects two dipoles of different sizes using a coplanar strip transmission line is given in [11]. The antenna had a wide bandwidth of 49.7% due to the integrated balun. However, the gain was 6.0 dBi, which is low in relation to the size of the antenna. A quasi-Yagi antenna using a folded dipole antenna and a director is presented in [12]. This antenna has a gain of 5.5 dBi and an impedance bandwidth of 12.3%. Although its structure is simple, reducing the space between the director and the driven element is difficult. The size of the proposed antenna is only $0.33\lambda_o \times 0.33\lambda_o$, the impedance bandwidth is 24.5%, and the gain at the center frequency is 5.9 dBi. The proposed antenna displayed excellent characteristics compared to existing antennas, as summarized in Table 2.

Table 2. Comparison of existing two-element antennas and proposed antennas

	-10 dB IBW (GHz)	Gain ^{a)} (dBi)	Antenna size
Wang and Park [8]	27.50–28.90 (5.0%)	7.0	$0.93\lambda_o \times 1.68\lambda_o$
Yeo and Lee [11]	1.68–2.79 (49.7%)	6.0	$0.60\lambda_o \times 0.90\lambda_o$
Hwang et al. [12]	26.30–29.75 (12.3%)	5.5	$0.47\lambda_o \times 0.47\lambda_o$
Proposed	4.47–5.72 (24.5%)	5.9	$0.33\lambda_o \times 0.33\lambda_o$

IBW=impedance bandwidth.

^{a)}Gain at center frequency.

IV. CONCLUSION

In this paper, a series-fed two-dipole endfire antenna with small size and good characteristics is proposed, comprising a meander line, a bent dipole, and a corrugated ground plane. The size of the proposed antenna is $0.33\lambda_o \times 0.33\lambda_o \times 0.014\lambda_o$, which is about one-third of the size of a conventional two-dipole endfire antenna. The impedance bandwidth and gain at 5 GHz are 4.47–5.72 GHz and 5.9 dBi, respectively, which are almost identical to those of the conventional two-dipole endfire antenna. Owing to its good characteristics, the proposed antenna can be useful in applications that require antennas with a small size, high gain, and wide bandwidth.

This work was supported in part by the National Research Foundation of Korea (NRF) grant funded by the Korea government (MSIT) (No. NRF-2022R1F1A1065324); in part by the National Research Foundation of Korea (NRF) grant funded by the Korea government (MSIT) (No. 2021R1A4A1030775); and in part by Institute of Information & communications Technology Planning & Evaluation (IITP) grant funded by the Korea government (MSIT) (No. 2022-0-00704-001, Development of 3D-NET Core Technology for High-Mobility Vehicular Service).

REFERENCES

[1] H. Wong, K. M. Luk, C. H. Chan, Q. Xue, K. K. So, and H. W. Lai, "Small antennas in wireless communications," *Proceedings of the IEEE*, vol. 100, no. 7, pp. 2109–2121, 2012.

- [2] M. W. Lee, K. W. Leung, and Y. L. Chow, "Dual polarization slotted miniature wideband patch antenna," *IEEE Transactions on Antennas and Propagation*, vol. 63, no. 1, pp. 353-357, 2015.
- [3] H. H. Tran, S. X. Ta, and I. Park, "A compact circularly polarized crossed-dipole antenna for an RFID tag," *IEEE Antennas and Wireless Propagation Letters*, vol. 14, pp. 674-677, 2015.
- [4] H. Lee, Z. Zahid, and H. Kim, "Loop-type ground radiation antenna for a C-shaped ground plane," *Journal of Electromagnetic Engineering and Science*, vol. 19, no. 1, pp. 1-5, 2019.
- [5] T. K. Nguyen, B. Kim, H. Choo, and I. Park, "Multiband dual spiral stripline-loaded monopole antenna," *IEEE Antennas and Wireless Propagation Letters*, vol. 8, pp. 57-59, 2009.
- [6] S. E. Sussman-Fort and R. M. Rudish, "Non-Foster impedance matching of electrically-small antennas," *IEEE Transactions on Antennas and Propagation*, vol. 57, no. 8, pp. 2230-2241, 2009.
- [7] H. Wang, K. E. Kedze, and I. Park, "A high-gain and wideband series-fed angled printed dipole array antenna," *IEEE Transactions on Antennas and Propagation*, vol. 68, no. 7, pp. 5708-5713, 2020.
- [8] H. Wang and I. Park, "Characteristics of the angled printed dipole array antenna with different numbers of dipole elements," *Journal of Electromagnetic Engineering and Science*, vol. 20, no. 3, pp. 183-189, 2020.
- [9] W. S. Yeoh, K. L. Wong, and W. S. T. Rowe, "Wideband miniaturized half bowtie printed dipole antenna with integrated balun for wireless applications," *IEEE Transactions on Antennas and Propagation*, vol. 59, no. 1, pp. 339-342, 2011.
- [10] H. Wang and I. Park, "Series-fed printed dipole array antenna," in *Proceedings of 2018 11th Global Symposium on Millimeter Waves (GSMW)*, Boulder, CO, 2018, pp. 1-3.
- [11] J. Yeo and J. I. Lee, "Modified series-fed two-dipole-array antenna with reduced size," *IEEE Antennas and Wireless Propagation Letters*, vol. 12, pp. 214-217, 2013.
- [12] I. J. Hwang, B. Ahn, S. C. Chae, J. W. Yu, and W. W. Lee, "Quasi-Yagi antenna array with modified folded dipole driver for mmWave 5G cellular devices," *IEEE Antennas and Wireless Propagation Letters*, vol. 18, no. 5, pp. 971-975, 2019.
- [13] J. H. Kim, M. G. Jeong, S. H. Bae, and W. S. Lee, "A printed fan-shaped meandered dipole antenna with mutual-coupled dual resonance," *IEEE Antennas and Wireless Propagation Letters*, vol. 16, pp. 3168-3171, 2017.
- [14] O. O. Olaode, W. D. Palmer, and W. T. Joines, "Effects of meandering on dipole antenna resonant frequency," *IEEE Antennas and Wireless Propagation Letters*, vol. 11, pp. 122-125, 2012.
- [15] G. Shin, M. Kong, S. H. Lee, S. T. Kim, and I. J. Yoon, "Gain characteristic maintained, miniaturized LPDA antenna using partially applied folded planar helix dipoles," *IEEE Access*, vol. 6, pp. 25874-25880, 2018.
- [16] R. Lesnik, N. Verhovski, I. Mizrachi, B. Milgrom, and M. Haridim, "Gain enhancement of a compact implantable dipole for biomedical applications," *IEEE Antennas and Wireless Propagation Letters*, vol. 17, no. 10, pp. 1778-1782, 2018.
- [17] A. Shafqat and F. A. Tahir, "Miniaturized tapered meandered dual band dipole antenna for WiFi 2.4/5.8 GHz application," in *Proceedings of 2017 Progress in Electromagnetics Research Symposium-Fall (PIERS-FALL)*, Singapore, 2017, pp. 1640-1642.
- [18] S. X. Ta, S. G. Kang, and I. Park, "Closely spaced two-element folded-dipole-driven quasi-Yagi array," *Journal of Electromagnetic Engineering and Science*, vol. 12, no. 4, pp. 254-259, 2012.
- [19] Y. Luo, Q. X. Chu, and L. Zhu, "A miniaturized wide-beamwidth circularly polarized planar antenna via two pairs of folded dipoles in a square contour," *IEEE Transactions on Antennas and Propagation*, vol. 63, no. 8, pp. 3753-3759, 2015.
- [20] Z. Wang, J. Wu, Y. Yin, and X. Liu, "A broadband dual-element folded dipole antenna with a reflector," *IEEE Antennas and Wireless Propagation Letters*, vol. 13, pp. 750-753, 2014.
- [21] S. Das, H. Saghlatoon, P. Mousavi, and A. K. Iyer, "A highly miniaturized and inherently conjugately matched folded dipole-based RFID tag antenna," *IEEE Access*, vol. 7, pp. 101658-101664, 2019.
- [22] D. E. Anagnostou, J. Papapolymerou, M. M. Tentzeris, and C. G. Christodoulou, "A printed log-periodic Koch-dipole array (LPKDA)," *IEEE Antennas and Wireless Propagation Letters*, vol. 7, pp. 456-460, 2008.
- [23] S. Das, D. J. Sawyer, N. Diamanti, A. P. Annan, and A. K. Iyer, "A strongly miniaturized and inherently matched folded dipole antenna for narrowband applications," *IEEE Transactions on Antennas and Propagation*, vol. 68, no. 5, pp. 3377-3386, 2020.
- [24] A. Verma, M. Arrawatia, and G. Kumar, "Low-profile wideband high-gain folded dipole antenna," *IEEE Antennas and Wireless Propagation Letters*, vol. 20, no. 6, pp. 1058-1062, 2021.
- [25] M. Zada and H. Yoo, "Miniaturized dual band antennas for intra-oral tongue drive system in the ISM bands 433 MHz and 915 MHz: design, safety, and link budget considerations," *IEEE Transactions on Antennas and Propagation*, vol. 67, no. 9, pp. 5843-5852, 2019.

- [26] Q. Liu, P. S. Hall, and A. L. Borja, "Efficiency of electrically small dipole antennas loaded with left-handed transmission lines," *IEEE Transactions on Antennas and Propagation*, vol. 57, no. 10, pp. 3009-3017, 2009.
- [27] C. C. Liu, P. L. Chi, and Y. D. Lin, "Compact zeroth-order resonant antenna based on dual-arm spiral configuration," *IEEE Antennas and Wireless Propagation Letters*, vol. 11, pp. 318-321, 2012.
- [28] H. Wang and I. Park, "Coplanar strip line-fed series dipole array antenna for high-gain realization," *IEEE Transactions on Antennas and Propagation*, vol. 69, no. 8, pp. 5106-5111, 2021.
- [29] C. A. Balanis, *Antenna Theory Analysis and Design*, 3rd ed. Hoboken, NJ: Wiley, 2005.
- [30] S. X. Ta, H. Choo, and I. Park, "Wideband double-dipole Yagi-Uda antenna fed by a microstrip-slot coplanar stripline transition," *Progress in Electromagnetics Research B*, vol. 44, pp. 71-87, 2012.
- [31] H. Wang and I. Park, "A compact series-fed two-element dipole antenna," in *Proceedings of 2021 IEEE International Symposium on Antennas and Propagation and USNC-URSI Radio Science Meeting (APS/URSI)*, Singapore, 2021, pp. 939-940.
- [32] R. A. Alhalabi and G. M. Rebeiz, "High-efficiency angled-dipole antennas for millimeter-wave phased array applications," *IEEE Transactions on Antennas and Propagation*, vol. 56, no. 10, pp. 3136-3142, 2008.

Heesu Wang



received his B.S. and M.S. degrees in Electrical and Computer Engineering from Ajou University, Suwon, Republic of Korea, in 2018 and 2020, respectively. He is currently studying for his Ph.D. degree at the Department of Electrical and Computer Engineering at Ajou University. His research interests include the design of patch antennas, printed antennas, small antennas, and metasurface antennas for various wire-

less communication applications.

Ikmo Park



received the B.S. degree in Electrical Engineering from the State University of New York at Stony Brook, and M.S. and Ph.D. degrees in Electrical Engineering from the University of Illinois at Urbana-Champaign. He joined the Department of Electrical and Computer Engineering at Ajou University in 1996. Prior to joining Ajou University, he has been working with the Device & Materials Laboratory of

LG Corporate Institute of Technology, Seoul, Republic of Korea, where he had been engaged in research and development of various antennas for personal communication systems, wireless local area networks, and direct broadcasting systems. He was a Visiting Professor at the Department of Electrical and Computer Engineering, POSTECH, Pohang, Republic of Korea, from March 2004 to February 2005, and the Department of Electrical and Computer Engineering, University of Arizona, Tucson, Arizona, USA, from July 2011 to June 2012. He has authored and co-authored over 300 technical journal and conference papers. He also holds over 50 domestic and international patents. He served as a Chair of the Department of Electrical and Computer Engineering at Ajou University. He is a member of Board of Directors at the Korea Institute of Electromagnetic Engineering and Science (KIEES). He serves as the Editor-in-Chief for the *Proceeding of the KIEES* and *Journal of KIEES*, an Editorial Board member for the *International Journal of Antennas and Propagation*, and an Associate Editor for *IET Electronics Letters*. He served as an Editorial Board member of the *Journal of Electromagnetic Engineering and Science*. He is also a member of Eta Kappa Nu and Tau Beta Pi.

Yong Bae Park



received the B.S., M.S., and Ph.D. degrees in Electrical Engineering from the Korea Advanced Institute of Science and Technology, South Korea, in 1998, 2000, and 2003, respectively. From 2003 to 2006, he was with the Korea Telecom Laboratory, Seoul, South Korea. He joined the School of Electrical and Computer Engineering, Ajou University, South Korea, in 2006, where he is currently a Professor. His research interests include electromagnetic field analysis, high-frequency methods, metamaterial antennas, radomes, and stealth technology.

Omega-K Algorithm Using Plane Wave Approximation for Forward-Looking Imaging Radar

Byunglae Cho · Sungwon Hong · Kichul Yoon*

Abstract

We propose an Omega-K algorithm that uses plane wave approximation for image formation in forward-looking imaging radar (FIRA) with the multi-input/double-output configuration. We assume that each of the transmitting antennas is located at the center of the receiving antenna array by applying a virtual antenna array. Then, we solve numerical equations in an approximation of the plane wave with the direction normal to the antenna array. Finally, we can obtain an image by proceeding with the following steps in order: the matched filtering, Stolt interpolation, two-dimensional inverse fast Fourier transform, phase compensation, image registration, and image merging. The performance of the proposed algorithm is verified through a simulation and a real experiment with neighboring targets. The results show that the proposed Omega-K algorithm with plane wave approximation can be successfully applied to FIRA systems with bistatic synthetic aperture radar configuration.

Key Words: Forward-Looking Imaging Radar, Omega-K Algorithm, Plane Wave Approximation, Ultra-Wideband, Unmanned Ground Vehicle.

I. INTRODUCTION

Synthetic aperture radar (SAR), which can produce high-resolution images regardless of brightness or weather conditions, has been an important and efficient Earth-observing tool that uses microwave frequencies. Although SAR systems have usually been operated from aircraft or orbiting satellite platforms, ground-based SAR (GB-SAR) systems have also been proposed as portable geotechnical instruments [1]. In some applications, vehicle-mounted forward-looking imaging radar (FIRA) using a real aperture has been employed to inspect forward ground surfaces [2–5]. A FIRA system installed on an unmanned ground vehicle (UGV) has also been proposed for visualizing forward areas through vegetation [3]. In many applications,

FIRA has usually adopted the multi-input/double-output (MIDO) principle to decrease system complexity, power consumption, weight, and cost.

Most previous research on FIRA has adopted the back-projection (BP) algorithm for image formation [3, 4]. However, the BP algorithm requires additional processing steps to reduce the sidelobes of FIRA images [6] and to increase spatial resolution. In addition, computation time depends on the size of the interested region due to the process that computes pixel-based received signals in the time domain. As alternatives, the range-Doppler method, the Omega-K method, and so on are also available. In FIRA applications, the bistatic configuration is more complicated than the monostatic configuration due to its difficulty and complexity in the formulation of analytic equa-

Manuscript received January 14, 2022 ; Revised April 5, 2022 ; Accepted June 28, 2022. (ID No. 20220114-007J)

Radar/EW Technology Center, Agency for Defense Development, Daejeon, Korea.

*Corresponding Author: Kichul Yoon (e-mail: yoonkc@add.re.kr)

This is an Open-Access article distributed under the terms of the Creative Commons Attribution Non-Commercial License (<http://creativecommons.org/licenses/by-nc/4.0>) which permits unrestricted non-commercial use, distribution, and reproduction in any medium, provided the original work is properly cited.

© Copyright The Korean Institute of Electromagnetic Engineering and Science.

tions and imaging algorithms [7]. In this paper, we describe the Omega-K algorithm in a bistatic configuration that uses plane wave approximation, phase compensation, image registration, and image merging. The next section describes the proposed method in detail, and the effectiveness of the method is verified by a simulation, in the case of point targets, and an experiment, employing a real FIRA introduced in [3].

II. SIMPLIFIED BISTATIC OMEGA-K ALGORITHM

1. Forward-Looking Imaging Radar

Sun et al. [3] investigated FIRA, which can detect visually hidden obstacles in vegetation, as a potential asset to support the autonomous navigation of a UGV or an unmanned air vehicle. Fig. 1 shows the schematic geometry of the FIRA system used in the proposed method. The radar system is installed on a commercial vehicle and operates in a frequency range of 3.6 GHz to 5.2 GHz. As shown in Fig. 1, the FIRA system has two transmitting (Tx) antennas located 0.2 m above the ends of the linear array, which is composed of 26 receiving (Rx) antennas. The receiving antennas are horizontally equally spaced at a distance of 0.03 m, and the total length is 0.75 m. The heights of the transmitting antennas and the receiving antenna arrays are 2.1 m and 1.9 m, respectively.

We used commercial horn antennas as transmitting antennas. Since the receiving antennas should be planar, compact in size, and directive with high radiation efficiency to compose a physical array, we used antipodal Vivaldi antennas with a high gain, a relatively wide bandwidth, and a simple structure. The antipodal Vivaldi antenna is advantageous due to its ease of fabrication and small volume. The voltage standing wave ratio is roughly less than 2.1 and the gain greater than 5 dBi over the frequency range of 3.6–5.2 GHz [3].

The transceiver in the FIRA system uses two independent direct digital synthesizers, followed by multipliers, to generate

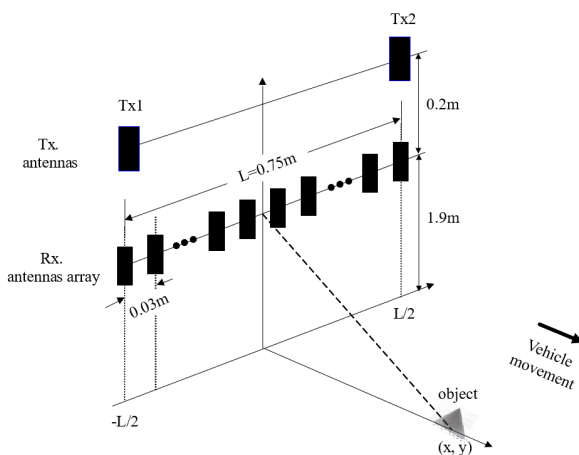


Fig. 1. Schematic geometry of the FIRA system.

transmitting and local oscillator (LO) signals, respectively. The transmit power is amplified by more than 25 dBm through an amplifier. The received signals pass through low-noise amplifiers, whose noise figure and gain are 2.8 dB and 14 dB, respectively, and are mixed with the LO signal. The signals are then processed after passing through low-pass filters and a 16-bit A/D converter with a sampling frequency of about 400 MHz [3].

2. Bistatic Omega-K Algorithm using Plane Wave Approximation

The target area is composed of an infinite or finite set of stationary targets located at the coordinates (x_n, y_n) . The measured signal at the receiving antenna position u and at the fast-time frequency ω is as follows [8]:

$$s_{Txi}(\omega, u) = \sum_n a_n(\omega, x_n, y_n, u_{Txi}, u) a(\omega, x_n, y_n, u_{Txi}, u) \times \exp[-jk\sqrt{x_n^2 + (y_n - u)^2}] \times \exp[-jk\sqrt{x_n^2 + (y_n - u_{Txi})^2}], \quad (1)$$

where $a(\cdot)$ is the radar amplitude pattern, $a_n(\cdot)$ the n^{th} target amplitude pattern, and u_{Txi} the position of the i^{th} transmitting antenna.

The Fourier transform of $s_{Txi}(\omega, u)$ with respect to the slow time u , followed by using the stationary phase method, results in the following equation:

$$S_{Txi}(\omega, k_u) = \sum_n A_n(\omega, k_u) A(\omega, k_u) \times \exp[-j(\sqrt{k^2 - k_u^2} x_n + k_u y_n)] \times \exp[-jk\sqrt{x_n^2 + (y_n - u_{Txi})^2}]. \quad (2)$$

The second phase term in Eq. (2) originates from the bistatic configuration, and we propose a simplified bistatic Omega-K algorithm using plane wave approximation, as demonstrated in Fig. 2 and the following explanation.

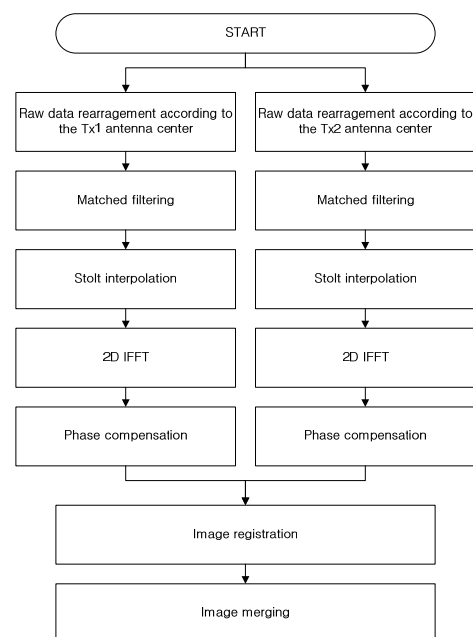


Fig. 2. Flowchart of the proposed method.

First, we assume that each Tx antenna is located at the center of the Rx antenna array, as illustrated in Fig. 3, and that the wave propagates as a plane wave. Consequently, the second phase term in Eq. (2) is simplified to Eq. (3).

$$\frac{\exp[-jk\sqrt{x_n^2 + (y_n - u_{Tx_i})^2}]}{\exp[-jk\sqrt{x_n^2 + y_n^2}] \approx \exp(-jkx_n). \quad (3)$$

Substituting Eq. (3) into Eq. (2), we obtain the following equation:

$$\begin{aligned} S_{Tx_i}(\omega, k_u) &\approx \sum_n A_n(\omega, k_u) A(\omega, k_u) \times \\ &\exp[-j\{(\sqrt{k^2 - k_u^2} + k)x_n + k_u y_n\}] = \\ &\sum_n A_n(\omega, k_u) A(\omega, k_u) \times \exp[-j\{k_x(\omega, k_u)x_n + \\ &k_y(\omega, k_u)y_n\}], \end{aligned} \quad (4)$$

where

$$\begin{aligned} k_x(\omega, k_u) &= \sqrt{k^2 - k_u^2} + k \\ k_y(\omega, k_u) &= k_u \end{aligned} \quad (5)$$

Stolt interpolation is performed according to the relationship of Eq. (5). An image can then be obtained by performing a two-dimensional (2D) inverse fast Fourier transform (IFFT).

The error caused by the plane wave approximation along the new coordinate axes centered at each transmitted antenna is compensated for, as shown in Eq. (6).

$$I_{Tx_i}^{comp}(x_n, y_n) = I_{Tx_i}(x_n, y_n) \times \exp\{-jk(\sqrt{x_n^2 + y_n^2} - x_n)\}, \quad (6)$$

where $I_{Tx_i}(\cdot)$ is the image obtained by 2D IFFT of $S_{Tx_i}(\omega, k_u)$.

Here, the coordinate axes of the two images obtained through Eq. (6) are not aligned. Therefore, the images must be registered on the original coordinate axis.

Finally, a combined image is created by the coherent summation of pixels from the two images.

III. SIMULATION AND EXPERIMENT RESULTS

The performance of the proposed method was analyzed through a simulation and an experiment conducted using the

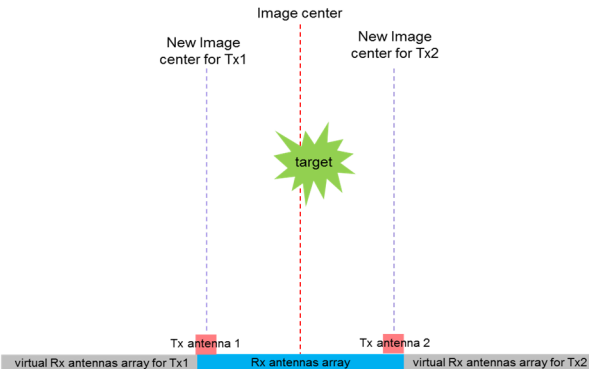


Fig. 3. Concept of plane wave approximation.

FIRA system developed by the Agency for Defense Development in South Korea [3].

1. Simulation Results with Point Targets

In the simulation, the raw data were corrupted by additive white Gaussian noise using MATLAB. Fig. 4 shows the results of the comparison between the images obtained by the BP algorithm and the proposed method. In the first simulation of a point target, the target is located at a range of 10 m with an azimuth of 0 m. As shown in Table 1, the cross-range resolution, or azimuth resolution, and peak side-lobe ratio (PSLR) have similar values for both imaging methods, but the integrated side-lobe ratio (ISLR) of the image obtained by the proposed method is superior to that obtained by the BP method.

In the other simulation, three neighboring point targets are located at $(10 \text{ m}, 0 \text{ m})$, $(10 \times \cos 5^\circ \text{ m}, 10 \times \sin 5^\circ \text{ m})$, and $(10 \times \cos 5^\circ \text{ m}, -10 \times \sin 5^\circ \text{ m})$. The proposed algorithm can distinguish the three neighboring targets and achieve image quality comparable to that achieved by the BP method.

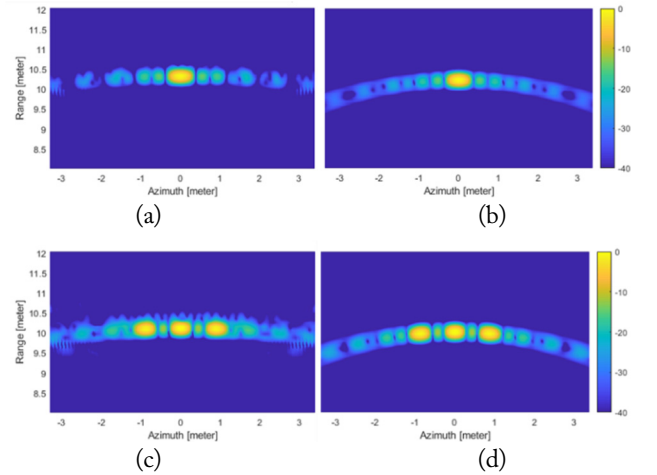


Fig. 4. Simulation results of a point target (a, b) and three neighboring point targets (c, d), obtained from the proposed method (a, c) and the back-projection method (b, d).

Table 1. Quantitative analysis of the image qualities for the FIRA images obtained by the proposed method and the back-projection method

	Back-projection		Proposed	
	Simulation	Experiment	Simulation	Experiment
Azimuth resolution (m)	0.33	0.36	0.34	0.37
PSLR (dB)	14.27	9.89	14.28	10.84
ISLR (dB)	10.79	5.88	9.42	5.62

"Simulation" presented the results of a point target in Fig. 4, and "Experiment" is the results of T1 target in Fig. 5.

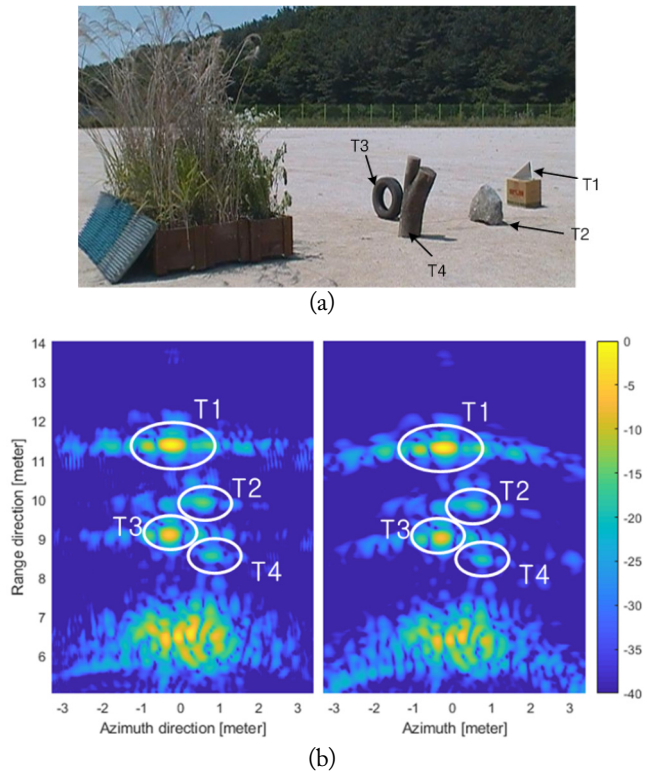


Fig. 5. (a) A photograph of the experimental site and (b) experiment results obtained from the proposed method (left) and the back-projection method (right).

2. Experimental Results with an Actual FIRA System

The experiments were carried out using the FIRA system described in the earlier section, with a pulse width of 2 ms and a sampling frequency of 400 MHz. A photograph of the measurement site is shown in Fig. 5(a). Four targets (a tree fork, a tire, a rock, and a trihedral corner reflector) on the ground were prepared, and reeds were placed between the targets and the FIRA system, visually hiding the targets from the FIRA system. In Fig. 5(b), the FIRA images by both the proposed method (left) and the BP method (right) show comparable qualities.

More quantitatively, the azimuth resolution, PSLR, and ISLR for the T1 target in Fig. 5(b) are evaluated and summarized in Table 1. The cross-range (azimuth) resolution had similar values for both imaging methods, but the PSLR and ISLR of the image obtained by the proposed method showed better performance than that obtained by the BP method.

For more detailed performance comparison, Fig. 6 presents azimuth cuts of the point target result in Fig. 4 and T1 target result in Fig. 5. The values of the azimuth resolution and PSLR are reconfirmed from the figures in Table 1.

IV. CONCLUSION

A novel image-formation method that can be used in a FIRA system with an MIDO configuration was proposed. This method

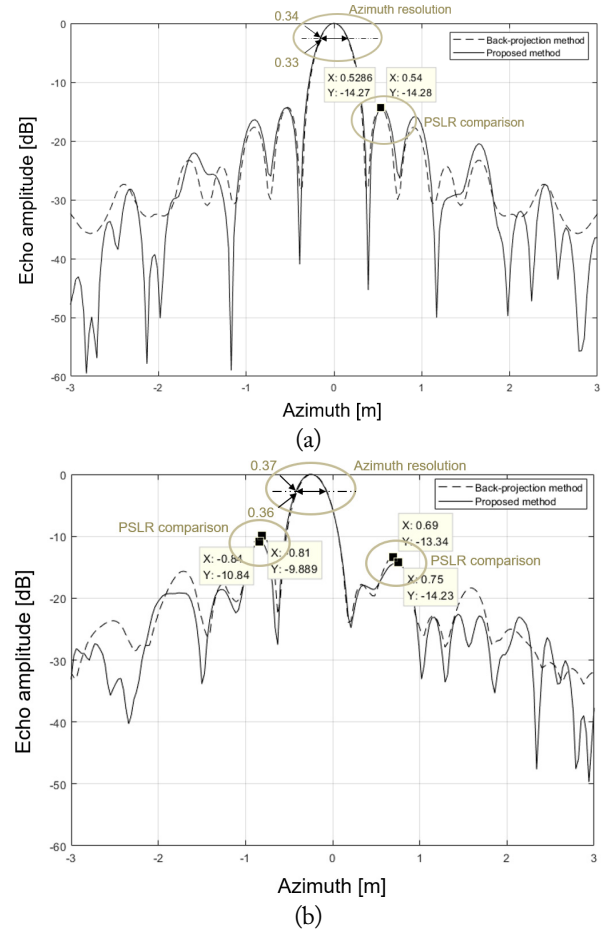


Fig. 6. Azimuth cuts of (a) a point target result in Fig. 4 and (b) T1 target result in Fig. 5 for comparison between the back-projection method and the proposed method.

is based on a conventional Omega-K algorithm. To resolve the difficulties originating from the bistatic configuration, the following approximation and assumption were used: approximation of spherical wave to plane wave radiating toward the interesting area and assumption that each of the transmitting antennas is located at the center of the receiving antenna array by applying a virtual antenna array. Phase compensation and image registration were then performed to compensate for errors caused by approximation and assumption.

The proposed method was tested through simulations with point targets and experiments using a real FIRA system, and the results were compared with those from the BP method. In terms of image quality, the proposed method and the BP method showed mostly comparable performance, but the PSLR and ISLR of the image obtained by the proposed method was superior to that obtained by the BP method. The proposed method can be applied to bistatic radar imaging systems.

REFERENCES

[1] B. L. Cho, Y. K. Kong, H. G. Park, and Y. S. Kim, "Auto-

- mobile-based SAR/InSAR system for ground experiments," *IEEE Geoscience and Remote Sensing Letters*, vol. 3, no. 3, pp. 401-405, 2006.
- [2] S. Yoo, H. Kim, G. Byun, and H. Choo, "Estimation of detection performance for vehicle FMCW radars using EM simulations," *Journal of Electromagnetic Engineering and Science*, vol. 19, no. 1, pp. 13-19, 2019.
- [3] S. G. Sun, B. L. Cho, J. S. Lee, G. C. Park, and J. S. Ha, "Ultra-wideband imaging radar to reveal obstacles concealed in vegetation to improve navigation of unmanned ground vehicles," *Journal of Electromagnetic Waves and Applications*, vol. 28, no. 11, pp. 1305-1315, 2014.
- [4] L. Nguyen and M. Soumekh, "System trade analysis for an ultra-wideband forward imaging radar," in *Proceedings of SPIE 6230: Unmanned Systems Technology VIII*. Bellingham, WA: International Society for Optics and Photonics, 2006, pp. 13-23.
- [5] T. Jin, Q. Song, and B. Lu, "Virtual array imaging radar azimuth resolution analysis," in *Proceedings of IET International Radar Conference*, Guilin, China, 2009.
- [6] B. L. Cho, S. G. Sun, and B. G. Lim, "Image enhancement in forward imaging radar using modified apodisation technique," *Electronics Letters*, vol. 49, no. 13, pp. 846-848, 2013.
- [7] B. Liu, T. Wang, Q. Wu, and Z. Bao, "Bistatic SAR data focusing using an omega-K algorithm based on method of series reversion," *IEEE Transactions on Geoscience and Remote Sensing*, vol. 47, no. 8, pp. 2899-2912, 2009.
- [8] M. Soumekh, *Synthetic Aperture Radar Signal Processing with MATLAB Algorithm*. New York, NY: John Wiley & Sons, 1999.

Byunglae Cho



received a B.S. degree in electronic and electrical engineering from Kyungpook National University in 1999 and M.S. and Ph.D. degrees in electronics and electrical engineering from POSTECH in 2001 and 2005, respectively. In 2005, he was with POSTECH as a postdoctoral researcher for one year. Since 2006, he has worked as a principal researcher at the Agency for Defense Development in Korea. His research

interests include SAR, interferometric SAR, forward-looking imaging radar, frequency-modulated continuous wave radar, and active electronically scanned array radar.

Kichul Yoon



received a B.S. degree in mechanical engineering, Sungkyunkwan University (2011), M.S. degree in mechanical and aerospace engineering, Seoul National University (2013), and Ph.D. degree in mechanical and nuclear engineering, The Pennsylvania State University (2016). In 2016, he joined the Agency for Defense Development in Korea. His research

interests include active phased-array radar systems and forward-looking imaging radar systems.

Sungwon Hong



received his B.S., M.S., and Ph.D degrees in electronic and electrical engineering from Kyungpook National University, Daegu, South Korea, in 2010, 2012, and 2017, respectively. Since 2017, he has been with the Agency for Defense Development, Daejeon, South Korea. His current research interests include radar system design, signal processing, and performance analysis.

A Neural Network-Based Microwave Imaging Method for Object Localization

Wonhyung Son¹ · Won-Kwang Park² · Seong-Ho Son^{1,3,*}

Abstract

This paper presents a new microwave imaging method using artificial neural networks to localize an object. The trained neural network reconstructs a tomographic image from the measured scattering data, such as a nonlinear electromagnetic inverse scattering solver. The appropriate number of hidden neurons is determined through the cross-entropy between network predictions and target values. To verify this method experimentally, we set up a testbed consisting of 16 antennas that transmit and receive 950 MHz microwaves underwater and used a metal rod with a diameter of 2 mm as a localizing target. The results show excellent imaging performance with fewer artifacts and less than a 2-mm localization error.

Key Words: Artificial Neural Networks, Inverse Scattering, Microwave Imaging, Object Localization.

I. INTRODUCTION

Microwave imaging, known as the inverse scattering problem [1], can be widely used in various fields, such as industry, military, medical, and daily life. In particular, with the emergence of the Internet of things, many researchers have recently paid attention to radio frequency (RF) energy rather than light, infrared, and thermal energy when inferring human movement [2]. While visible light cameras are highly sensitive to light and can invade privacy when monitoring humans, RF can pass through non-metallic materials, unlike light or thermal energy. Because of these advantages, the RF-based localization technique can be used in object tracking, indoor fire detection, survivor sensing, and elderly monitoring. Thus far, many localization technologies have been developed (see Table 1 in [2]). Recently, improved radio tomographic imaging, which reconstructs from the re-

ceived signal strength, has been presented [3]. The signal patterns induced by the target are different when the target appears at different locations. Therefore, by analyzing the changes in the RF signal, the location of the target can be determined. Other methods include ultra-wideband tomographic radar imaging [4] and multistatic microwave imaging [5]. These methods use the scattering parameters measured. The reconstructed image shows the distribution of the dielectric properties of an object or localizes small anomalies that are stationary or moving [5].

However, there are still challenges to be solved in the nonlinear electromagnetic inverse scattering problem, such as the unpredictability of the scattered signal in a multi-pass environment, the low spatial resolution of the reconstructed image, the uncertainty of the sensor position, and the ill-posedness of inverse problems [1].

On the other hand, an artificial neural network (NN) is

Manuscript received January 22, 2022 ; Revised June 5, 2022 ; Accepted July 21, 2022. (ID No. 20220122-008J)

¹Department of ICT Convergence, Soonchunhyang University, Asan, Korea.

²Department of Information Security, Cryptology, and Mathematics, Kookmin University, Seoul, Korea.

³Department of Mechanical Engineering, Soonchunhyang University, Asan, Korea.

*Corresponding Author: Seong-Ho Son (e-mail: son@sch.ac.kr)

This is an Open-Access article distributed under the terms of the Creative Commons Attribution Non-Commercial License (<http://creativecommons.org/licenses/by-nc/4.0>) which permits unrestricted non-commercial use, distribution, and reproduction in any medium, provided the original work is properly cited.

© Copyright The Korean Institute of Electromagnetic Engineering and Science.

recognized as a powerful technique in microwave modeling and design [6]. NNs can learn nonlinear input-output relationships by training with corresponding data. These trained NN models can be used to provide fast answers to learned tasks.

Therefore, NN can also be an efficient tool for developing inverse models for microwave imaging. To this end, this paper presents a new multistatic microwave imaging method that applies NN for object localization under conditions where analytical formulas for inverse models do not exist or are difficult to obtain.

II. METHOD

The general configuration of multistatic microwave imaging consists of distributing a certain number of sensors (transmitters and receivers) to a certain region surrounding the object [3–5]. Here, the difference in scattering parameters for transmitter n and receiver m , $\Delta S_{m,n}$, can be obtained by subtracting each scattering data with and without an object: $\Delta S_{m,n} = |S_{m,n}^{with} - S_{m,n}^{without}|$. These data reveal the intrinsic signatures scattered by the object in which the influence of the background and surrounding noise has been eliminated.

To reconstruct the tomographic image, the scattering data Δs become the input to the NN, as shown in Fig. 1. Then, a nonlinear function f between the input and output can be approximated by NN training: $c = f(\Delta s)$, where c is reconstructed image data (pixel intensity), meaning the dielectric contrast between the object and the background. Here, the scattering datasets collected from all potential locations are used to train the NN model using supervised learning.

To verify the proposed method, we set up a testbed (Fig. 2). In the water tank (600 mm \times 600 mm \times 400 mm), 16 monopole antennas operating at 950 MHz are arranged with a diameter of 180 mm (the wavelength is about 35 mm in the water). One antenna transmits the microwave signal, and the other antennas receive the propagated signals. This process is repeated sequentially to collect data of 16 \times 16 scattering matrix for the input of the NN. The scattering data are acquired with a vector network analyzer (Keysight E5063A) connected with an in-house-made 2 \times 16 switch matrix (not shown in Fig. 2).

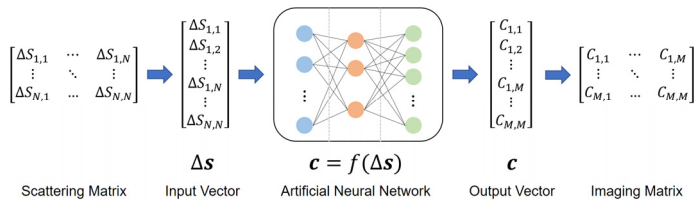


Fig. 1. Neural network model reconstructing a tomographic image from scattering data.

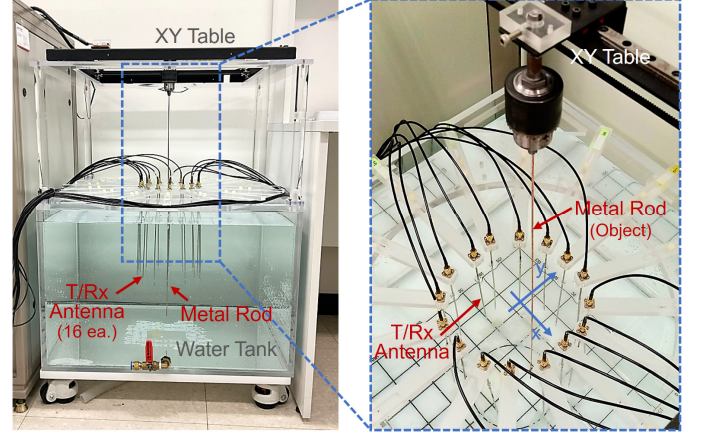


Fig. 2. Experimental setup.

The imaging area is set to 140 mm \times 140 mm. For the reconstruction, the area is divided into 28 \times 28 pixels (5 mm/pixel), which is one-seventh of the wavelength used. Therefore, the number of output nodes of the NN becomes 784. The detailed parameters used in the study are summarized in Table 1. On the other hand, the minimum sampling criteria are reported in terms of the dimension of the reconstruction area and practical measurement aspects (see Section II-B of [4]).

Meanwhile, a metal rod 2 mm in diameter is used for the localizing object. Scattering datasets for 1,000 positions are collected, while the rod is moved to random positions with the XY positioner. Here, 70% of the datasets are used for training, 15% for validation, and 15% for testing.

The well-trained NN expects to convert the measured scattering data into a tomographic image with 5 mm pixels. Then, the image is upsampled to 1 mm pixels by cubic interpolation to obtain a finer image, and the peak is normalized to 1.

III. RESULTS

In the NN model, the decision of the hidden layer is critical. This is because using too many neurons can lead to overfitting and poor generalization. Therefore, we first investigated how

Table 1. Parameters of the neural network used in this study

Item	Description
Input vector	Measured scattering parameters
Output vector	Intensity of imaging pixels
Input node	256 (16 \times 16)
Hidden node	35
Output node	784 (28 \times 28, 5 mm/pixel)
Training algorithm	Scaled conjugate gradient
Loss function	Cross-entropy

the number of hidden neurons affect localization. The performance, H , was evaluated with the average cross-entropy of N samples used for training: $H(T, Y) = -\frac{1}{N} \sum_{n=1}^N \sum_{i=1}^K T_{ni} \log Y_{ni}$, where T and Y are network predictions and target values (intensity values of K pixels in the imaging area), respectively.

As a result of increasing the number of neurons from 10 to 1,000, cross-entropy was minimized at around 100 neurons and then gradually increased. This shows that increasing the number of neurons does not guarantee performance improvement. The representative results are shown in Fig. 3. Meanwhile, according to the cross-entropy trend, we finally selected 35 neurons in the hidden layer to simplify the NN. The resulting image is almost identical to the image reconstructed with 100 neurons, showing better localization and fewer artifacts.

Using the designed NN, we demonstrated two cases. The first is when the position of the object is slightly away from the antenna (Fig. 4), and the second is when the object is close to the antenna (Fig. 5). Here, to show the NN-based method, it was compared with the bi-focusing (BF) method (see Section II-A of [4]), which is one of the conventional imaging methods based on analytical formulation.

Comparing the results in terms of localization error (BF, 4–7 mm; NN, 1–2 mm), peak-to-sidelobe ratio (BF, 0.7–0.9; NN, 0.1–0.2), and half-spatial resolution (BF, 15–18 mm; NN, 6–8 mm), all performances of the proposed NN method are much better.

IV. CONCLUSION

In this paper, an NN-based microwave imaging method was proposed to localize an object placed under conditions in which it is difficult to obtain an analytical formula. This was verified in an experimental testbed with a 16-antenna array operating at 950 MHz. For this, we designed an NN with 256 inputs and 784 outputs. Here, 35 hidden neurons determined from cross-entropy were used. The trained NN successfully converted the measured scattering data into tomographic image data and localized the object well within a 2-mm error and fewer artifacts, showing excellent imaging performance compared to the conventional method based on an analytical formulation.

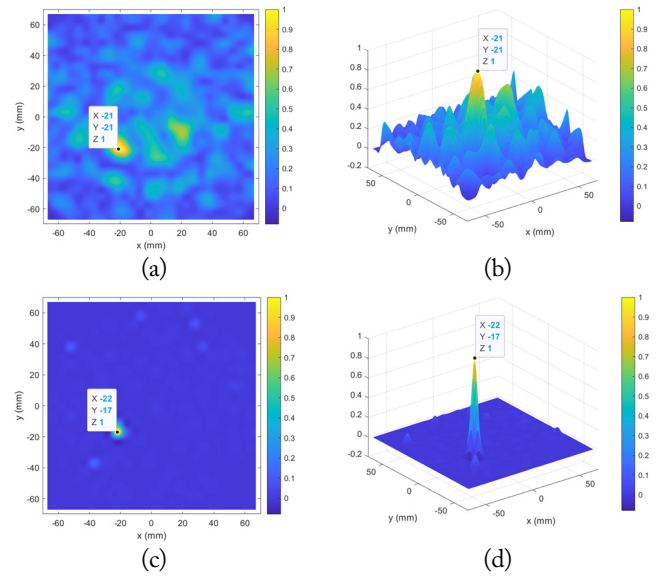


Fig. 4. Imaging results for an object located at $(-21, -17)$ mm: (a) 2D and (b) 3D views of BF method, (c) 2D and (d) 3D views of NN method.

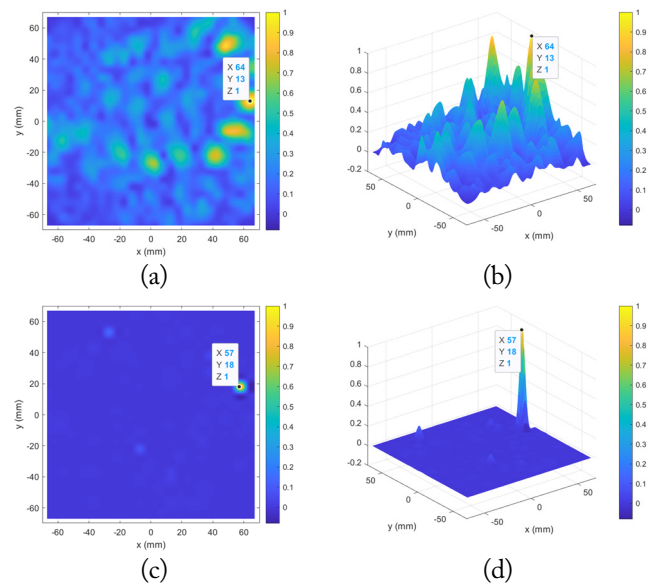


Fig. 5. Imaging results for an object located at $(57, 16)$ mm: (a) 2D and (b) 3D views of BF method, (c) 2D and (d) 3D views of NN method.

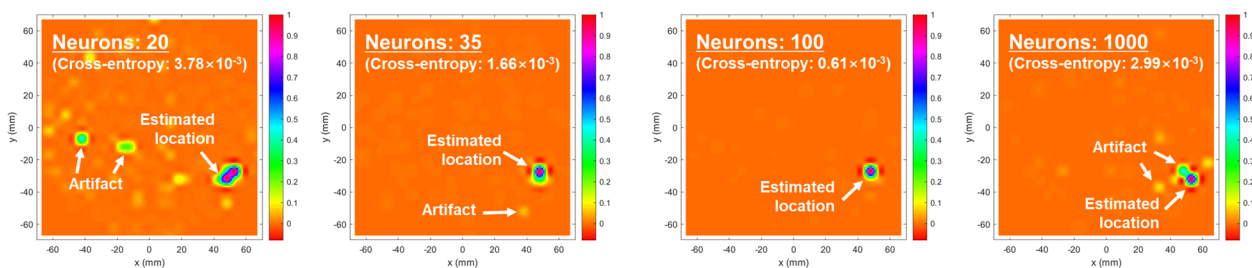


Fig. 3. NN-based imaging results according to the number of hidden neurons for an object located at $(47, -31)$ mm.

This work was partly supported by the Institute of Information & communications Technology Planning & Evaluation (IITP) grant funded by the Korea government (MSIT) (No. 2021-0-00731), the National Research Foundation of Korea (NRF) grant funded by the Korea government (MSIT) (No. NRF-2020R1A2C1A01005221), and the Soonchunhyang University Research Fund.

REFERENCES

- [1] R. C. Aster, B. Borchers, and C. H. Thurber, *Parameter Estimation and Inverse Problems*, 3rd ed. Cambridge, MA: Elsevier, 2019.
- [2] H. Obeidat, W. Shuaieb, O. Obeidat, and R. Abd-Alhameed, "A review of indoor localization techniques and wireless technologies," *Wireless Personal Communications*, vol. 119, no. 1, pp. 289–327, 2021.
- [3] J. Tan, Q. Zhao, X. Guo, X. Zhao, and G. Wang, "Radio tomographic imaging based on low-rank and sparse decomposition," *IEEE Access*, vol. 7, pp. 50223–50231, 2019.
- [4] L. Jofre, A. Broquetas, J. Romeu, S. Blanch, A. P. Toda, X. Fabregas, and A. Cardama, "UWB tomographic radar imaging of penetrable and impenetrable objects," *Proceedings of the IEEE*, vol. 97, no. 2, pp. 451–464, 2009.
- [5] W. K. Park, "Application of MUSIC algorithm in real-world microwave imaging of unknown anomalies from scattering matrix," *Mechanical Systems and Signal Processing*, vol. 153, article no. 107501, 2021. <https://doi.org/10.1016/j.ymsp.2020.107501>
- [6] J. Jin, F. Feng, W. Na, S. Yan, W. Liu, L. Zhu, and Q. J. Zhang, "Recent advances in neural network-based inverse modeling techniques for microwave applications," *International Journal of Numerical Modelling: Electronic Networks, Devices and Fields*, vol. 33, no. 6, article no. e2732, 2020. <https://doi.org/10.1002/jnm.2732>

Wonhyung Son



received the B.S. degree in mechanical engineering from Soonchunhyang University, Asan, South Korea, in 2020, and the M.S. degree in ICT Convergence from the same university, in 2022. He is currently working as a researcher at DMTS Co. (Daejeon R&D Lab), Ulsan, Korea. His research interests include electromagnetic/mechanical wave sensing and imaging, machine learning, and mechatronics.

Seong-Ho Son



received the B.S. degree in control and mechanical engineering from Pusan National University, Busan, South Korea, in 1997, and the M.S. and Ph.D. degrees from Pohang University of Science and Technology (POSTECH), Pohang, South Korea, in 1999 and 2009, respectively. From 1999 to 2001, he was a researcher with the Technical Research Center, Daewoo Motors (now, GM Korea), Incheon, South Korea. From 2001 to 2019, he was a principal researcher with the Radio and Satellite Research Division, Electronics and Telecommunications Research Institute (ETRI), Daejeon, South Korea, where he was involved in the development of microwave medical imaging and thermotherapy technologies. Since 2019, he has been an assistant professor with the Department of Mechanical Engineering, Soonchunhyang University, Asan, South Korea, where he also joined the Department of ICT Convergence. His research interests include electromagnetic/mechanical wave sensing and imaging, phased arrays, mechatronic systems, and machine learning.

Won-Kwang Park



received the M.S. degree in mathematics from Yonsei University, Seoul, South Korea, in 2004, and the Ph.D. degree in applied mathematics from the Ecole Polytechnique, Palaiseau, France, in 2009. After graduation, he joined the Institute for Mathematics and Scientific Computing, Karl Franzens University of Graz, Austria, as a Postdoctoral Researcher, in 2009. In 2010, he joined the Department of Mathematics in Kookmin University, as a full-time lecturer, where he is currently a full professor at the Department of Information Security, Cryptology, and Mathematics in Kookmin University. His research interests include inverse problems, microwave imaging, and scientific computing.

Spatial Delay Line Canceler-Based Sidelobe Blanking for Low Radar-Cross-Section Target

Youn-Hui Jang^{1,*} · Donghyeon Cho²

Abstract

This study proposes a sidelobe blanking (SLB) system with a spatial delay line canceler (DLC) and non-coherent integrator in a uniform linear array. After the equations for the target and noise power in the SLB system were established, SLB-ratio functions for the proposed and conventional SLB channels were developed. Using these ratio functions, the optimal SLB thresholds for the general detectable target and low radar-cross-section (RCS) target were estimated. The results of the SLB thresholds were confirmed by the Monte Carlo simulation, which indicated that the proposed SLB channel provides reliable performance without false SLB decisions in the sidelobe region. Using the estimated optimal threshold, the proposed SLB channel provides reliable performance, particularly for low-RCS targets. In contrast, the conventional SLB channel produces numerous false SLB decisions in the sidelobe region. The proposed synthesis is a simple but powerful method for obtaining the reliable SLB ratio. The SLB channel in various array antenna systems can be developed based on this method.

Key Words: Low-RCS Target, Optimal SLB Threshold, Radar, SLB-ratio Function, SLB Synthesis, Spatial Delay Line Canceler.

I. INTRODUCTION

A radar detects a target in a desired direction by transmitting and receiving radio waves. This means that the antenna of the radar maximizes the directivity of the detection direction and suppresses the other directions using a tapering window. Hereafter, in this study, the antenna beamwidth centered on the detection direction is referred to as the mainlobe, whereas the suppressed region excluding the mainlobe is referred to as the sidelobes.

In addition to signals from the mainlobe, the antenna simultaneously receives suppressed signals from the sidelobe. Despite the directivity of the antenna, the target signal in the mainlobe may still be indistinguishable from the clutter signals suppressed

in the sidelobe because of the inherently low radar cross-section (RCS) of the target. If these unwanted signals from the sidelobe are not deleted or blanked during post-processing, it may result in false targets or system degradation of the radar.

To blank the sidelobe signals, radars use a sidelobe blanker (SLB). For this purpose, radars make an auxiliary channel for the SLB channel in addition to the detection channel and compares the output magnitudes of the detection and the SLB channels. Hereafter, the detection channel is referred to as the main beam channel, which forms the mainlobe on the detection direction. The SLB system first sorts out the mixed sidelobe signal in the main beam channel and then blanks it [1, 2].

Although an SLB channel generally requires a dedicated antenna, a phased array antenna can re-synthesize the outputs of

Manuscript received February 7, 2022 ; Revised June 5, 2022 ; Accepted July 21, 2022. (ID No. 20220207-013J)

¹Agency for Defense Development, Daejeon, Korea.

²Department of Electronics Engineering, Chungnam National University, Daejeon, Korea.

*Corresponding Author: Youn-Hui Jang (e-mail: yhjjang@add.re.kr)

This is an Open-Access article distributed under the terms of the Creative Commons Attribution Non-Commercial License (<http://creativecommons.org/licenses/by-nc/4.0>) which permits unrestricted non-commercial use, distribution, and reproduction in any medium, provided the original work is properly cited.

© Copyright The Korean Institute of Electromagnetic Engineering and Science.

the array for the SLB channel without an additional antenna. In addition, it can simultaneously apply adaptive beamforming to the main beam and SLB channels for nulling interference.

In this study, we focused on synthesizing a robust SLB channel for low-RCS targets. The synthesized SLB channel should be simply implementable to be expansible for adaptive beamforming. We designed this channel using a discrete Fourier analysis of spatial frequency and a finite impulse response (FIR) filter system in discrete time.

Digital signal processing (DSP), which samples time signals in a fixed sampling period, has a discrete sequence. Thus, assuming an equally spaced array, such as a uniform linear array (ULA) and far-field radiation, we can analyze array processing using the DSP technique. Some studies have already offered a fundamental understanding of digital array processing with FIR filtering [3, 4]. In addition, many applied studies have also been published.

Within the domain of array processing, adaptive beamforming has been investigated in diverse research fields. For radar, the objective of adaptive beamforming is to preserve detection performance under conditions of strong jamming or interference. Therefore, an adaptive SLB channel should be adopted for preserving the target through adaptive beamforming in the main beam channel; otherwise, the target will inevitably be blanked by strong interference in non-adaptive SLB channel. This requirement has resulted in various adaptive SLB studies [6–9]. While one study generalized adaptive detection using a generalized likelihood ratio test (GLRT) for SLB [6], another described a 2D adaptive sidelobe blanker (ASB) using the generalized adaptive coherence/cosine estimator (ACE) [7]. Yet another study modified the 2D adaptive matched filter (AMF) and ACE detector introduced in the aforementioned study using subarrays [8]. Suitable thresholds were presented for the detection margin, and results were achieved based on the designed subarrays.

Although research on adaptive methods for SLB is abundant, studies on channel synthesis for actual implementation are rare. We proposed an adaptive SLB channel synthesis in a ULA system using spatial delay line cancelers (DLC) and non-coherent integrators [10–13]. The synthesis is simple but powerful in terms of the ratio difference between the channels, also called the detection margin [8]. In this study, we formulated SLB thresholds appropriate for low-RCS targets with equations for the signal-to-noise ratio (SNR) in the SLB system. We verified the performance using Monte Carlo simulations for all angles of the various target scenarios.

Practically, in a phased-array antenna system, the physical phenomenon of array mutual coupling and inaccurate calibration produces a substandard final array pattern, such as the main beam shape and the sidelobe level (SLL). Despite sound theoretical synthesis, inferior SLL performance causes degradation of SLB. Therefore, we focused on robust synthesis with a sufficient ratio

difference for all angles to overcome this practical problem.

Section II summarizes the SLB channel synthesis proposed in an earlier study [12], while Section III presents the equations of the target signal, noise signal, and ratio for the SLB decision. Following this, Section IV presents the SLB thresholds suitable for the target signals and the results of the Monte Carlo simulation. Finally, Section V concludes the study.

II. ADAPTIVE SLB CHANNEL SYNTHESIS

1. Conventional SLB System

To generate a good SLB performance, the angular pattern of the SLB channel should be distinguishable separately from that of the main beam channel in terms of the angular region, as displayed in Fig. 1. If this difference is insufficient, clutter with large RCS originating from the sidelobe region cannot be blanked, which may result in numerous false targets in the main beam channel. Therefore, proper SLB channel design is critical for the optimization of the main beam of the radar system.

Fig. 1 displays the typical angular gain patterns of the main beam and SLB channels. The gain pattern of the SLB channel is smaller than that of the main beam channel in the mainlobe, which is the detection region, whereas the pattern is larger than that of the main beam channel in the sidelobe region. Fig. 2 presents a block diagram of a radar SLB system, in which the SLB decision compares the ratio of $main^2$ (the output power of the main beam channel) to slb^2 (the output power of the

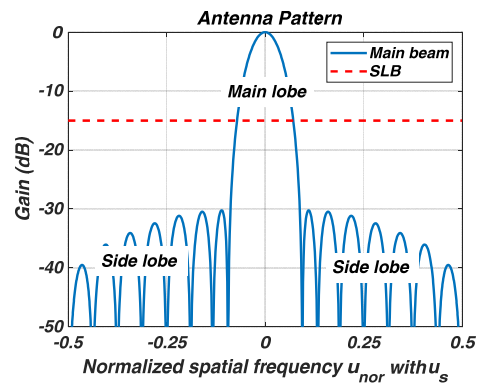


Fig. 1. Angular gain patterns of the main beam and SLB channels.

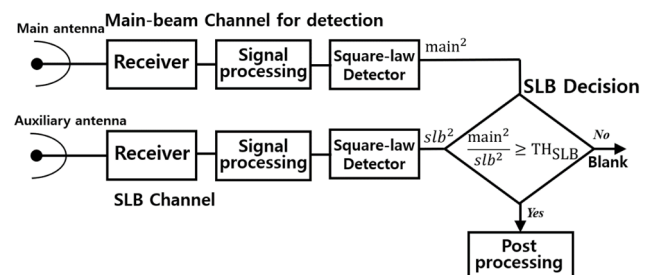


Fig. 2. SLB system of the radar.

SLB channel) with a threshold of TH_{SLB} [1, 2]. If $main^2$, represented by the solid line in Fig. 1, is smaller than TH_{SLB} compared to slb^2 , which is represented by the dotted line in Fig. 1, the $main^2$ is assumed to originate from the sidelobe region and is eventually blanked. Since the actual signal of the mainlobe in the main beam channel exhibits maximum antenna gain, it is always greater than the output of the SLB channel.

$$SLB \text{ blank } main^2 \quad \text{if } \frac{main^2}{slb^2} < TH_{SLB},$$

$$\text{process } main^2 \text{ otherwise.} \quad (1)$$

where,

$main$: output of the main-beam channel,

slb : output of the SLB channel,

TH_{SLB} : threshold of the SLB decision.

2. Adaptive SLB System with Spatial DLC and Non-coherent Integrator

As mentioned earlier, to obtain a clear SLB decision, the main beam channel should be sufficiently greater than the SLB channel in the mainlobe. In this study, we set the decision criterion as TH_{SLB} and designed a distinguishable angular pattern of the SLB channel in the overall angular domain. Fig. 3 depicts an adaptive SLB channel synthesized in a ULA system, along with the spatial DLC and non-coherent integrators [12].

A DLC in the Doppler domain is a simple and powerful tool for indicating a moving target. Thus, it was applied to the spatial domain. A spatial DLC forms a null at the boresight ϕ_{look} of the angular pattern in the same manner as the DLC does on the zero Doppler. The proposed SLB synthesis is summarized as follows: first, the null makes a significant gap between the two channels within the mainlobe. Second, in the sidelobe region, the non-coherent integrator makes the angular pattern of the SLB channel uniformly higher than that of the main beam

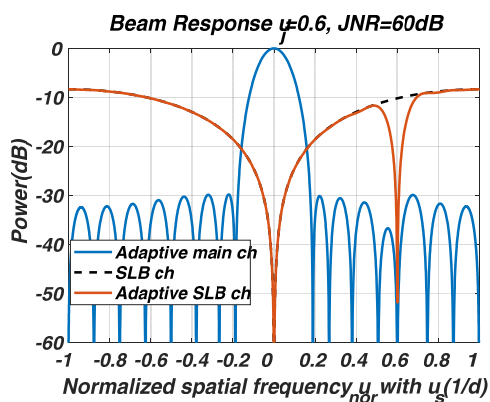


Fig. 3. Comparison of the angular patterns between the adaptive main and the proposed adaptive SLB channels using the spatial DLC and non-coherent integrators: ULA with 16 elements, $d = \lambda/2$, and Taylor window (30 dB SLL). Adapted from [12].

channel. Finally, adaptive beamforming ensures robust SLB performance in environments with interference.

In this section, we briefly describe the spatial DLC response, which is explained in further detail in Fig. 4. The DLC operation is called the first difference in discrete time [14]. Each sample in the output signal is equal to the difference between the two adjacent samples in the input signal. Using this operation, we defined the spatial DLC system in the ULA with the impulse response $h_{sDLC}[n]$ and frequency response $H_{sDLC}(u)$, where n is the element number in N -element ULA, and u is the spatial frequency in period u_s .

$$h_{sDLC}[n] = \delta[n] - \delta[n - 1]$$

$$\xleftrightarrow{DTFT} H_{sDLC}(u) = 1 - \exp(-j2\pi u/u_s)$$

$$= \exp(-j\pi u/u_s) \cdot (2j \cdot \sin(\pi u/u_s)) \quad (2)$$

Owing to the zero value of $\sin(\pi u/u_s)$ at $u = 0$ in $H_{sDLC}(u)$ with $u_{look} = 0$, the angular pattern of the adaptive SLB channel is considerably different from that of the adaptive main channel. Therefore, $main^2/sl b^2$ is clearly distinguishable between the mainlobe and the sidelobes, thus improving SLB decisions.

III. SLB-RATIO FUNCTION FOR SLB DECISION

In this section, we present the SNR of each input/output signal as well as the SLB ratio formulation in the proposed SLB system. To simplify the equations, we assumed the boresight $\phi_{look} = 0^\circ$ of the array and omitted adaptive beamforming.

As mentioned previously, we developed formulations of the N -element ULA using a discrete-time Fourier transform (DTFT) or DSP technique, with $n = 0, 1, \dots, N-1$ in the spatial/array domain and u along with period u_s in the spatial frequency domain. However, in this study, we did not consider the time variables in each element or the array system. Note that variable n represents the sample or element number in the spatial/array domain and is not related to time. A former study has explained the DSP technique in terms of the sample domain [17].

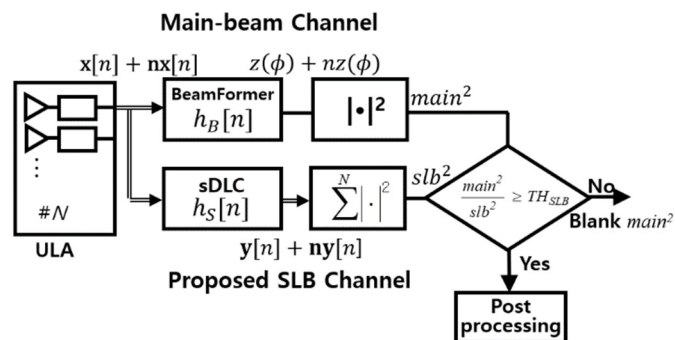


Fig. 4. Block diagram of the proposed SLB system in the ULA.

1. Impulse Response and Frequency Response of the SLB System

In the N -element ULA, the signal field arriving from ϕ is measured at locations $d \cdot n$ of N elements with spatially equal distance d , expressed as:

$$\begin{aligned} r(n, \phi) &= a(n, \phi) \cdot p(n, \phi) \quad n = 0, 1, \dots, N-1 \\ &= \alpha \cdot p(n, \phi) \end{aligned} \quad (3)$$

where $a(\cdot)$ and $p(\cdot)$ represent the amplitude and phase distributions of the elements, respectively, while ϕ is the arrival angle perpendicular to the ULA. For isotropic and far-field radiation, the distribution of $a(\cdot)$ is uniform over all n and becomes a constant α . The phase difference between the adjacent elements is consecutively delayed, corresponding to the direction of ϕ . This denotes the response of the array, which can be expressed as follows:

$$\begin{aligned} p(n, \phi) &= \exp(j2\pi \cdot \sin\phi / \lambda \cdot d \cdot n) \\ \text{Or } p(n, u) &= \exp(j2\pi u / u_s n) \end{aligned} \quad (4)$$

where λ and d represent the wavelength of the signal and the equal distance between the elements, respectively.

N samples of the measured signal in the ULA have a fixed spatial sampling distance of d between samples, spatial frequency $u = \sin\phi / \lambda$ by equal phase difference between samples, and a spatial sampling frequency of $u_s = 1/d$ [5, 12].

$$r(n, u) = \alpha \cdot \exp(j2\pi u / u_s n) \quad n = 0, 1, \dots, N-1 \quad (5)$$

The output of the array eventually constitutes a discrete sequence of $r(n, \phi)$ satisfying the DSP technique, and can produce a function of spatial frequency u through DTFT.

Spatial domain of the array ($n = 0, 1, \dots, N-1$) $\xleftrightarrow{\text{DTFT}}$
 Spatial frequency domain (u periodic with u_s)
 Inverse DTFT:

$$r[n] = \int_{-u_s/2}^{u_s/2} R(u) \cdot e^{i2\pi \frac{u}{u_s} n} du \quad (6)$$

where

$$R(u) = \sum_n r[n] \cdot e^{-i2\pi \frac{u}{u_s} n} \quad (7)$$

$r[n]$ represents a discrete set of samples $r(n, \phi)$ measured in each element.

Fig. 4 displays a block diagram specifying the mathematical expressions for the input/output signal and the impulse responses of each stage in the proposed SLB system. For the target signal, $x[n]$ denotes the output set of the array and input set of the SLB system, $y[n]$ denotes the output set of the spatial DLC in the proposed SLB channel, while $z(\phi)$ denotes the output of the beamformer in the main beam channel for detection. The

noise signals are denoted as $nx[n]$, $ny[n]$, and $nz(\phi)$ with respect to the target signal. Furthermore, the final output signals of each channel are denoted by $main^2$ and slb^2 , in which the target and noise are still mixed.

We denote the impulse responses of the spatial domain and the spatial frequency responses in each channel using Eqs. (6) and (7). In this context, $h_B[n]$ and $H_B(u)$ indicate the beamformer in the main-beam channel, whereas $h_S[n]$ and $H_S(u)$ refer to the spatial DLC in the SLB channel. We define the normalization constants α_{BF} and α_{sDLC} , respectively, for the constraint "noise gain = 1."

$$\begin{aligned} h_B[n] &= \alpha_{BF} \cdot h_{BF}[n], \quad \alpha_{BF} = \frac{1}{\sqrt{\sum_{k=0}^{N-1} |h_{BF}[k]|^2}} \\ h_B[n] &\xleftrightarrow{\text{DTFT}} H_B(u) = \alpha_{BF} \cdot H_{BF}(u) \end{aligned} \quad (8)$$

$$\begin{aligned} h_S[n] &= \alpha_{sDLC} h_{sDLC}[n], \quad \alpha_{sDLC} = \frac{1}{\sqrt{\sum_{k=1}^2 |h_{sDLC}[k]|^2}} \\ h_S[n] &\xleftrightarrow{\text{DTFT}} H_S(u) = \alpha_{sDLC} \cdot H_{sDLC}(u) \end{aligned} \quad (9)$$

Since the SLB system satisfies the conditions for DTFT, which particularly has an equal spatial sampling distance of d for all n , it can also be considered for digital FIR filtering. $h_B[n]$ represents a filter matched to the array response vector for the boresight $\phi_{look} = 0^\circ$ as well as the conventional frequency-selective digital filter of finite length [5]. This indicates that we can design N coefficients of $h_B[n]$ for the directivity to reach a maximum frequency response at $u_{look} = \sin \phi_{look} / \lambda = 0$. Similarly, we can observe the $h_S[n]$ of Eq. (2) as the frequency-selective FIR filter, with two coefficients for the frequency response with the null at $u_{look} = 0$. In addition, for causality, we designed the length of the FIR filter in such a way that the n th output uses only the samples of the i th elements, with $i \leq n$ at an observation time, as in Eq. (2). Thus, the designed FIR filter is causal for n .

Eq. (10) shows the general form of the output $g[m]$ in a causal discrete FIR system, which is analogous to the discrete convolution of $f[m]$ with coefficients of $h[m]$ in Eq. (11) [14–16]:

$$g[m] = \sum_{k=0}^{M-1} b_k f[m-k] \quad (10)$$

$$h[m] = \begin{cases} b_m & m = 0, 1, \dots, M-1, \\ 0 & \text{otherwise.} \end{cases} \quad (11)$$

The impulse response $h[m]$ has a finite length of M .

This general form can be used to obtain the output of the FIR filter in Fig. 4, according to the discrete input sequence of $r(n, u_i)$ in Eq. (5):

$$\begin{aligned}
 g[n] &= \sum_{k=0}^{M-1} h_x[k] \cdot r[n-k, u_i] \\
 &= \underbrace{\alpha \cdot \exp(j2\pi \frac{u_i}{u_s} n)}_{r(n, u_i)} \underbrace{\sum_{k=0}^{M-1} h_x[k] \exp(-j2\pi \frac{u_i}{u_s} k)}_{H_x(u_i)} \quad (12)
 \end{aligned}$$

where $g[n]$ represents the output of a FIR filter, $h_x[n]$ denotes any impulse response in Fig. 4, and u_i is the spatial frequency of the input samples related to the arriving direction ϕ .

Since the input set $r[n, u_i]$ is a complex exponential, the n th output $g[n]$ finally represents the multiplied form of the n th input sample $r(n, u_i)$ and $H_x(u)$ at u_i : $H_x(u)$ represents the spatial frequency response of M -length $h_x[n]$ FIR filter. Specifically, $H_x(u_i)$ indicates the value of the frequency response designed for frequency-selectivity according to the input spatial frequency. Eq. (12) can be further understood with digital FIR filtering as follows: the length of the frequency-selective FIR filter, and the steady-state response of the FIR system:

(i) We designed the M -length of $h_x[n]$ to extract the desired spatial frequency-selective response, for example, the directivity and the null. Thus, the number of valid output samples depends on the M . If M is greater than the number of input samples N , we cannot obtain the valid output with the designed frequency-selective response of $M \leq N$, which is a necessary condition for Fig. 4. In the spatial DLC in the SLB channel, the output $y[n]$ has valid output samples of $N-1$, $n = 1, \dots, N-1$, since $h_s[n]$ satisfies the causality of the first difference operation and is 2-length in Eq. (2). In the case of the beamformer in the main beam channel, for N -length $h_B[n]$, the only $N-1$ th output is valid:

$$\begin{aligned}
 z(u_i) &= g[N-1] = \sum_{k=0}^{N-1} h_B[k] x[(N-1)-k] \\
 &= x(N-1, u_i) \cdot H_B(u_i) \\
 &= \alpha_x \exp(j2\pi u_i / u_s \cdot (N-1)) \cdot H_B(u_i) \quad (13)
 \end{aligned}$$

The output with one sample no longer has a variable of n in the spatial domain, and is related to the spatial frequency response at u_i , as in Eq. (13).

(ii) If the input of the FIR system is a complex exponential, as in Eqs. (5) and (12), the $H_x(u_i)$ in the output is referred to as the steady-state response of the system [14]. It represents the spatial frequency response at u_i in steady state, such as a pass-band or a stop-band. In addition, the steady state indicates holding its frequency response for all observations [14–16]. Consequently, the $H_x(u)$ with the input-complex-exponential must persist for n of any output. In particular, the steady state response $H_x(u)$ has no more statistical meaning, such as averaging over n . On the other hand, the first term in Eq. (12), representing the value of the current input sample, becomes only a factor for scaling the ampli-

tude and shifting the initial phase independent of the system response. Therefore, it is regarded as an ignorable complex constant of the system response.

2. Target Signal

The target signal sampled at each element, $x(n, u_t)$, refers to the complex exponential form generated along with the target's amplitude and spatial frequency [19]:

$$x(n, u_t) = \sigma_t \exp(j2\pi u_t / u_s n) \quad n = 0, 1, \dots, N-1 \quad (14)$$

where

σ_t : RCS or amplitude of the target,

$u_t = \sin(\phi_t) / \lambda$: spatial frequency of the target,

ϕ_t : arriving angle of the target.

As in Eq. (3), the instant amplitude of $x(n, u_t)$ at an arbitrary time has the same deterministic value σ_t for all n . Thus, we obtain the target's input power of $x[n]$ in Fig. 4:

$$P_x = E\{|x[n]|^2\} = \sigma_t^2 E\left\{\left|\exp(j2\pi \frac{u_t}{u_s} n)\right|^2\right\} = \sigma_t^2 \quad (15)$$

where $E\{\cdot\}$ denotes the expected value for all n in the spatial domain.

We summarize the target output signal in the proposed SLB channel. First, using Eqs. (9) and (12), the output set of the spatial DLC $y[n]$ consists of:

$$\begin{aligned}
 y[n] &= \sum_{k=1}^{N-1} h_s[k] \cdot x[n-k] \quad n = 1, 2, \dots, N-1 \\
 &= \sigma_t \exp(j2\pi \frac{u_t}{u_s} n) \cdot H_S(u_t) \quad (16)
 \end{aligned}$$

According to the null at $u_{look} = 0$ in Eqs. (2) and (9), if the target of $y[n]$ is on the boresight $u_t = u_{look}$, the frequency response $H_S(u_t)$ becomes zero, that is, $y[n] = 0$, if $u_t = u_{look}$.

Next, the proposed SLB channel passes $y[n]$ through the non-coherent integrator, which calculates the energy of $y[n]$ through the total sum of the input power, as specified in Fig. 4. We obtain the target output signal for slb^2 by employing \hat{E}_y , the modified energy by $\alpha_{N,I}$ to satisfy the noise normalization constraint in Eq. (18).

$$E_y = \sum_{k=1}^{N-1} |y[k]|^2 = (N-1) \cdot \sigma_t^2 |H_S(u_t)|^2 \quad (17)$$

$$\hat{E}_y = \alpha_{N,I} \cdot E_y \quad \alpha_{N,I} = 1/(N-1) \quad (18)$$

Finally, we obtain the target output signal for $main^2$ in Fig. 4. The output power in $main^2$ can be mathematically expressed as the squared magnitude of the beamformer—the output signal $z(u)$ of the main beam former is in accordance with $z(\phi)$. As mentioned in the steady-state response of the FIR system with complex exponential inputs, the expected value of

the output $z(u)$ for all n becomes unimportant. Therefore, we obtain the target output signal in $main^2$ as power P_z :

$$P_z = |z(u_t)|^2 = \sigma_t^2 \cdot |H_B(u_t)|^2 \quad (19)$$

3. Noise Signal

Contrary to a target signal with a deterministic amplitude, the expected value for all n can be calculated using an autocorrelation function, since noise power is a random variable [14–16]. Let σ_n^2 and m be the average noise power in the output of each element and the lag amount of the autocorrelation function, respectively. Since $nx[n]$ is uncorrelated between the elements, the autocorrelation function $\rho_{nx,nx}(m)$ can be expressed as follows:

$$\rho_{nx,nx}[m] = \sigma_n^2 \cdot \delta[m] \quad (20)$$

The average power of $nx[n]$, P_{nx} , is considered to be equal to the autocorrelation function's quantity at $m = 0$:

$$P_{nx} = E\{nx^2[n]\} = \rho_{nx,nx}[0] = \sigma_n^2 \quad (21)$$

For the output noise signal $ny(n)$ of the spatial DLC, the autocorrelation function and its average power are denoted as follows [14–16]:

$$\rho_{ny,ny}[m] = \rho_{nx,nx}[m] * h_S[m] * h_S^*[-m] \quad (22)$$

where $*$ is a discrete convolution and $*$ represents a complex conjugate.

$$P_{ny} = E\{ny^2[n]\} = \rho_{ny,ny}[0] = \sigma_n^2 \sum_{k=1}^2 |h_S(k)|^2 \quad (23)$$

For the final output noise in slb^2 by the non-coherent integrator, we obtain the energy of the input noises, $E_{ny} = (N - 1)P_{ny}$, as in Eq. (17), and then normalize it using the noise constraint constant $\alpha_{N,I}$:

$$\hat{E}_{ny} = \alpha_{N,I}(N - 1)P_{ny} \quad \alpha_{N,I} = 1/(N - 1) \quad (24)$$

Next, we consider the noise signal in $main^2$. The output noise set $nz(n)$ of the beamformer can be represented in the same manner as Eqs. (22) and (23).

$$\rho_{nz,nz}[m] = \rho_{nx,nx}[m] * h_B[m] * h_B^*[-m] \quad (25)$$

$$P_{nz} = E\{nz^2[n]\} = \rho_{nz,nz}[0] = \sigma_n^2 \sum_{k=0}^{N-1} |h_B(k)|^2 \quad (26)$$

Finally, we review the output noises \hat{E}_{ny} and P_{nz} of the two channels, along with the noise constraint constants.

$$\begin{aligned} \hat{E}_{ny} &= P_{ny} = \sigma_n^2 \sum_{k=1}^2 |h_S(k)|^2 \\ P_{nz} &= \sigma_n^2 \sum_{k=0}^{N-1} |h_B(k)|^2 \end{aligned} \quad (27)$$

where

$$\begin{aligned} \sum_{k=1}^2 |h_S(k)|^2 &= |\alpha_{sDLC}|^2 \sum_{k=1}^2 |h_{sDLC}(k)|^2 = 1 \\ \sum_{k=0}^{N-1} |h_B(k)|^2 &= |\alpha_{BF}|^2 \sum_{k=0}^{N-1} |h_{BF}(k)|^2 = 1 \end{aligned}$$

Though the output noises \hat{E}_{ny} and P_{nz} have individual gains in proportion to the input noise power σ_n^2 , all gains become "unit gain = 1" by α_{sDLC} and α_{BF} . Therefore, all output noises in Fig. 4 have the same value of σ_n^2 .

$$P_{nx} = P_{nz} = P_{ny} = \hat{E}_{ny} = \sigma_n^2 \quad (28)$$

4. Input/Output SNR and SLB-Ratio Function

This section presents the input and output SNRs of each channel as well as the SLB ratio between the two channels for the SLB decision using equations of the targets and noise signals. For the performance comparison, the output SNR of the conventional SLB channel, SNR_{slb_conv} , is further defined as Eq. (32). We assume that the conventional SLB uses the one-element output of the array antenna or the non-coherent integrator of the elements with noise normalization [9], SNR_{slb_conv} , which has the same SNR as the input. The input/output SNR can then be expressed as:

Input SNR of the SLB system, as shown in Fig. 4:

$$SNR_{in} = P_x/P_{nx} = \sigma_t^2/\sigma_n^2 \quad (29)$$

Output SNR of the main beam channel:

$$SNR_{main} = P_z/P_{nz} = SNR_{in} \cdot |H_B(u_t)|^2 \quad (30)$$

Output SNR of the proposed SLB channel:

$$SNR_{slb} = \hat{E}_y/\hat{E}_{ny} = SNR_{in} \cdot |H_S(u_t)|^2 \quad (31)$$

Output SNR of the conventional SLB channel:

$$SNR_{slb_conv} = P_x/P_{nx} = \sigma_t^2/\sigma_n^2 = SNR_{in} \quad (32)$$

Next, we derive the SLB ratio of $main^2$ to slb^2 for the SLB decision. The target and noise signals in the channel were mixed and were found to be uncorrelated, indicating that they are independent variables. Therefore, the average power of the channel can be obtained by adding the average power of the target and the noise.

The expected value of the SLB ratio $E\{Ratio\}$ between the output powers of the two channels is summarized in Eq. (33) by noise normalization, depending on the output SNRs of the two channels.

$$\begin{aligned} E\{Ratio\} &= E\left\{\frac{main^2}{slb^2}\right\} = \frac{P_z + P_{nz}}{\hat{E}_y + \hat{E}_{ny}} = \frac{P_z/P_{nz} + 1}{\hat{E}_y/\hat{E}_{ny} + 1} \\ &= \frac{SNR_{main} + 1}{SNR_{slb} + 1} \end{aligned} \quad (33)$$

Substituting the equations of the output SNRs, we can obtain the SLB ratios depending on the SNR_{in} , u_t , and the spatial frequency responses of two channels, as follows:

$$E\{Ratio\} = \frac{SNR_{in} \cdot |H_B(u_t)|^2 + 1}{SNR_{in} \cdot |H_S(u_t)|^2 + 1} \quad (34)$$

Extending u_t to the entire spatial frequency domain, we can compare the SLB ratio functions between $R(\cdot)$ of the proposed SLB and $R_{conv}(\cdot)$ of the conventional SLB.

$$R(u, SNR_{in}) = \frac{SNR_{in} \cdot |H_B(u)|^2 + 1}{SNR_{in} \cdot \alpha \left| \sin\left(\pi \frac{u}{u_s}\right) \right|^2 + 1} \quad (35)$$

where α is 2, as indicated by Eqs. (2) and (9).

$$R_{conv}(u, SNR_{in}) = \frac{SNR_{in} \cdot |H_B(u)|^2 + 1}{SNR_{in} + 1} \quad (36)$$

The different component of Eqs. (35) and (36) is the $\sin(\pi u/u_s)$ term of $H_S(u)$ in the denominator, which creates a null at $u = u_{look}$. Thus, for a target near u_{look} , the $R(\cdot)$ may be approximated to SNR_{main} , which is significantly greater than $R_{conv}(\cdot)$: if $u_t \approx u_{look}$, $R(u_{look}) \gg R_{conv}(u_{look})$. However, for a target in the sidelobe region, it becomes gradually smaller because of $\sin(\cdot)$. Compared to $R_{conv}(\cdot)$, $R(\cdot)$ provides a distinguishable ratio with respect to u and then ensures an excellent SLB performance, which ultimately decides whether the target originates from the sidelobe or otherwise.

The various target scenarios for the SLB ratios are listed in Table 1, while the SLB ratios of Eqs. (35) and (36) are illustrated in Fig. 5. We employed the Taylor window with an SLL of

Table 1. Target scenarios for the simulation (Element # 16, $G_{SNR} = 11.35$ dB with Taylor 30 dB SLL)

	SNR_{main} (dB)	SNR_{in} (dB)
Case 1	10	-1.35
Case 2 ^a	13	1.65
Case 3	16	4.65

G_{SNR} = SNR gain of the beamformer in the main beam.

$SNR_{in} = SNR_{main} - G_{SNR}$

^aA typical minimum-detectable target in the radar.

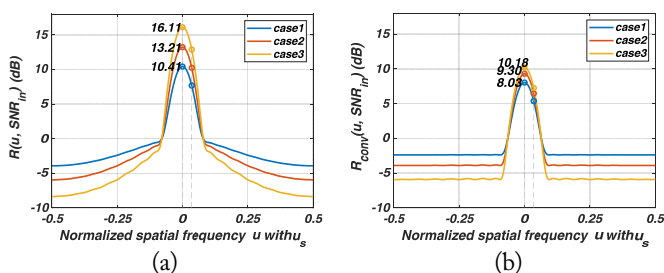


Fig. 5. Graph of $R(u, SNR_{in})$ and $R_{conv}(u, SNR_{in})$ for the targets in Table 1: (a) proposed SLB channel and (b) conventional SLB channel.

30 dB for tapering in a 16-element ULA.

For Case 2 in Table 1, the target with a 13-dB SNR_{main} represents a commonly *minimum-detectable target* in the radar detector. The signal would be injected with 1.65-dB SNR_{in} at the input of the beamformer to obtain $SNR_{main} = 13$ dB at u_{look} for this simulation. Compared to the minimum-detectable target with 13-dB SNR_{main} in Case 2, Case 3 represents a more easily detectable target with 3-dB higher power, while Case 1 represents a low-RCS target with 3-dB lower power.

We generated the target signal arriving from the individual u of all u and then calculated the SLB ratios in Fig. 5. For the u_{look} within the mainlobe, $R(\cdot)$ in (a) has a large value close to SNR_{main} , but the $R_{conv}(\cdot)$ in (b) has a relatively low value. Conversely, in the sidelobe region, $R(\cdot)$ gradually decreases to be lower than $R_{conv}(\cdot)$. Furthermore, for the identical target case, $R(\cdot)$ has a value that is 2–6 dB higher than that of $R_{conv}(\cdot)$ at u_{look} , and a lower value in the sidelobe. We can observe that $R(\cdot)$ provides considerably distinct ratios for various target scenarios according to SNR_{in} .

IV. OPTIMAL SLB THRESHOLD AND SIMULATION RESULTS

In this section, we estimate the SLB thresholds suitable for the desired targets using the derived SLB-ratio function. The results are demonstrated through 10,000 Monte Carlo simulations.

For practical situations, a cos-shaped element pattern was used to simulate a target signal [20].

$$f_e(\varphi)^2 = \cos^3 \varphi \quad (37)$$

1. SLB Thresholds Appropriate for the Targets

The radar system generally regards a 3-dB beam width as the detection region, while the blanking region of an SLB indicates the regions that exclude the detection region. We determined the SLB threshold of the boundary separating the detection and blanking regions as the value of the SLB-ratio function at a 3-dB beam width of $\pm u_{3dB}$ using Fig. 5.

Table 2 indicates the SLB thresholds—the SLB-ratio function's value with respect to a wanted SNR_{in} and $\pm u_{3dB}$. It is evident that Th 2 is applicable for the typical minimum-

Table 2. SLB thresholds for $\pm u_{3dB}$ (detection region) corresponding to a low-RCS target and a detectable target

	SNR_{main} (dB)	TH_{SLB} (dB)	
		$R(u_{3dB}, SNR_{in})$	$R_{conv}(u_{3dB}, SNR_{in})$
Th 1	10	7.50	5.40
Th 2	13	10.23	6.50

detectable target with 13-dB SNR_{main} , while Th 1 is appropriate for a low-RCS target with 3-dB lower power.

TH_{SLB} by $R(\cdot)$ of 10.23 and 7.5 dB refer to the proposed SLB channel, 6.5 and 5.4 dB by $R_{conv}(\cdot)$ refer to the conventional SLB channel in the simulations. The proper SLB thresholds by $R(\cdot)$ for the detection region are much higher than those by $R_{conv}(\cdot)$, thus performing robust SLB decisions in noisy environments or with the low-RCS targets. This is because the proposed SLB channel increases $R(\cdot)$ significantly within the detection region as mentioned previously. In contrast, 6.5-dB Th 2 by $R_{conv}(\cdot)$ has an insufficient difference relative to the noise even for the minimum-detectable target of 13-dB. Furthermore, Th 1 for a low-RCS target is severely lowered to 5.4 dB, we can predict that the lower threshold will lead to the performance degradation. The superiority of the SLB thresholds by the proposed SLB channel was verified in more detail in the simulation results.

2. Simulation Results

The Monte Carlo simulation generated the test signal with the noise at every u point of the target scenarios in Table 1, estimated the SLB ratio, and processed the SLB decision with reference to the SLB thresholds in Table 2. The same procedures were repeated 10,000 times at each u .

With reference to the figures depicted in this section, the legend "sDLC + NCI" pertains to the proposed SLB channel and "Conventional" pertains to the conventional SLB channel.

In (a) of Figs. 6–11, the y-axis of "Target Existence Decision#" denotes the number of decisions about the target-in-mainlobe at each u . Specifically, the SLB determines that the angle of the test signal is the mainlobe and does not blank it—it is interpreted as either *the detectability of the target-in-mainlobe* or *the blanking ability of the target-in-sidelobe*. This represents SLB performance at a specific u .

In (b) of Figs. 6–11, the y-axis of the "Probability mass function" represents the proportional quantity of "Target Existence Decision#" at each u to the total decisions taken in all u . It represents the probability density of "Target Existence Decision#" in the u domain, also known as the discrete density function [21]. This indicates the reliability of the SLB performance in a particular u compared to all other u domains. Notably, the probability mass function $f_{tgtML}(\hat{u}_i)$ has a sum value of 1 for all u :

$$\sum_{\hat{u}_i=-0.5}^{0.5} f_{tgtML}(\hat{u}_i) = 1 \quad (38)$$

where \hat{u}_i is u normalized with u_s , $\hat{u}_i = u/u_s$.

We analyzed the performance results of the SLB synthesis and thresholds with the following indicators:

1) The amount of "Target Existence Decision#" within $\pm u_{3dB}$ represents *the detectability of the target-in-mainlobe in the*

detection region, meaning the frequency of a target-in-mainlobe decision occurring in the mainlobe. If this value is low, many of the target-in-mainlobes are blanked by SLB, thus reducing the detection probability of a radar.

2) *The distribution of the probability mass function* identifies the region where the decision probability of the mainlobe target occurs intensively.

3) The partial sum of the probability mass function within $\pm u_{3dB}$ involved *a reliability in the detection region* relative to the entire u domain. This is an important indicator of a low-RCS target because an improper SLB threshold or an insufficient SLB ratio can frequently blank the target with low SNR_{main} in the detection region. Thus, we have displayed the quantities in tabular form. Additionally, an unfavorable SLB ratio and SLB threshold of a low-RCS target are inherently difficult when it comes to satisfying overall performance. Hence, a reasonable threshold may be acceptable. Although there is a disadvantage of low detectability of "Target Existence Decision#" in the detection region, it is sufficient to satisfy fewer blanking errors and high reliability in the detection region. Nevertheless, in the proposed method, an appropriate threshold exhibits superior detectability with high reliability in the detection region.

4) The remaining partial sum within the $\pm u_{3dB}$ involved a *blanking error in the blanking-region*:

$$1 - \sum_i^{\pm u_{3dB}} f_{tgtML}(u_i) \quad (39)$$

Despite the blanking region, the SLB incorrectly makes a decision as the target-in-mainlobe and does not blank it. This further relates to the blanking ability of the target-in-sidelobe.

2.1 Results of the threshold appropriate for a minimum-detectable target

Initially, we set TH_{SLB} as Th 2 applicable for the typical minimum-detectable target in Table 2, the input target scenarios in Table 1 were simulated. The results are presented in Figs. 6–8 and Table 3.

For Cases 2 and 3 in Figs. 7(a) and 8(a), since the input targets have enough SNR_{main} of 13-dB or more for Th 2, "sDLC + NCI" and "Conventional" both exhibit good detectability of the target-in-mainlobe in the detection region. However, due to the false SLB decisions in the sidelobe region in the (a) of Figs 7 and 8, "Conventional" shows poor reliabilities across u compared to "sDLC + NCI". In contrast, "sDLC + NCI" has the intensive shape of the probability mass function only within the detection region in (b)s, ensuring excellent reliability across u .

For Case 1 of a low-RCS input target in Fig. 6, its signal of a 10-dB SNR_{main} at u_{look} is significantly lower than that of Cases 2 and 3 as well as the target's SNR subject to Th 2. Thus the estimated SLB ratio is also reduced relative to Th 2—

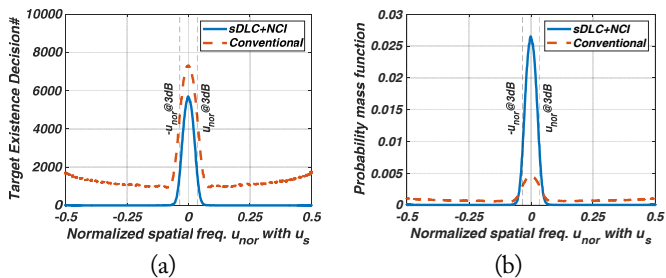


Fig. 6. Results for Case 1 (input target with $SNR_{main} = 10$ dB at u_{look}): Th 2 for the target with $SNR_{detectable} = 13$ dB. (a) number of decisions as the target in the mainlobe and (b) probability mass function of (a).

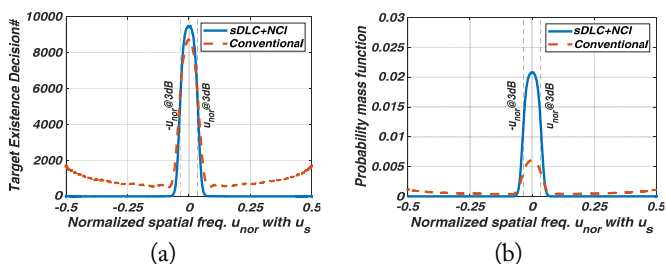


Fig. 7. Results for Case 2 (input target with $SNR_{main} = 13$ dB at u_{look}): Th 2 for the target with $SNR_{detectable} = 13$ dB. (a) number of decisions as the target in the mainlobe and (b) probability mass function of (a).

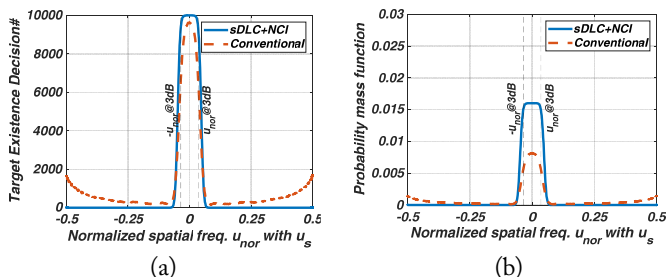


Fig. 8. Results for Case 3 (input target with $SNR_{main} = 16$ dB at u_{look}): Th 2 for the target with $SNR_{detectable} = 13$ dB. (a) number of decisions as the target in the mainlobe and (b) probability mass function of (a).

Table 3. Partial sum of $f_{tgtML}(u_i)$ within $\pm u_{3dB}$ (Th 2)

Input target	SNR_{main} at u_{look} (dB)	$\sum_i^{\pm u_{3dB}} f_{tgtML}(u_i)$	
		sDLC+NCI	Conventional
Case 1	10	0.90	0.19
Case 2	13	0.86	0.25
Case 3	16	0.75	0.35

Th 2 (dB) = 10.23 (sDLC + NCI), 6.50 (Conventional).

meaning that we have an insufficient difference between the estimated SLB ratio in Case 1 and Th 2. Therefore, as observed in Fig. 6(a), the "Target Existence Decision#" occurred slightly in both "sDLC + NCI" and "Conventional." More severely, "Conventional" increases the overall blanking error in the blanking region. However, "sDLC + NCI" still guarantees a good reliability across u in Fig. 6(b).

Specifically, in Table 3, "sDLC + NCI" of Case 3 has high reliability of 0.9 in the detection region despite the low detectability, owing to the lower SNR_{in} —meaning that almost all decisions of the target-in-mainlobe occur correctly near u_{look} . Cases 2–3 of "sDLC + NCI" guarantee the reliability of 0.75 and 0.86 near the detection region, and moreover, Case 3 has perfect decisions of 10,000 near u_{look} . On the other hand, the reliability of "Conventional" in the detection region decreases from 0.35 and 0.25 for Cases 2–3 to 0.19 for Case 1, specifically indicating the deterioration of the overall performance with the lower SNR_{in} .

Th 2 of "sDLC + NCI" has much better overall performance than Th 2 of "Conventional," and is reasonable even for a low-RCS input target due to the high reliability in the detection region. The following section indicates that having an appropriate SLB threshold for a low-RCS target can improve the results of the "sDLC + NCI."

2.2 Results of the threshold appropriate for low-RCS target with $SNR_{detectable} = 10$ dB

We reset TH_{SLB} as Th 1 appropriate for a low-RCS target in Table 2, and equally simulated the input target scenarios. The results are presented in Figs. 9–11 and Table 4. We compared the results of different SLB thresholds Th 1–2 for the identical input targets. The value of Th 1 decreases with SNR_{in} of a low-RCS target compared to the value of Th 2.

In the results of "Conventional," comparing (a) of Figs. 6–8 and (a) of Figs. 9–11, numerous errors in the SLB decisions occur outside the detection region. Since a severe low value of 5.4 dB for Th 1 frequently considers the noise to false target. Besides, across all u , the "Target Existence Decision#" increases slightly owing to the lower threshold. Thus, using Th 1 instead of Th 2 improves detectability slightly better in the detection region, but significantly reduces the blanking ability in the blanking region. We also observe that the values of the probability mass function at u_{look} decrease further in (b) of Figs. 9–11, and eventually the reliability of the detection region of Case 1 deteriorates from 0.19 to 0.17 in Tables 3–4.

In the results of "sDLC + NCI", Th 1 is significantly reduced by approximately 3 dB—from 10.23 to 7.50 dB. Therefore, comparing (a) of Figs. 6–8 and (a) of Figs. 9–11, the "Target Existence Decision#" increases remarkably across all u . Specifically, for Case 1 in Figs. 6 and 9, it increases by more than 30%:

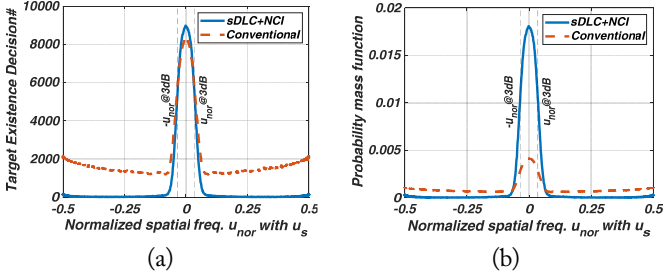


Fig. 9. Results for Case 1 (input target with $SNR_{main} = 10$ dB at u_{look}): Th 1 for the target with $SNR_{detectable} = 10$ dB. (a) number of decisions as the target in the mainlobe and (b) probability mass function of (a).

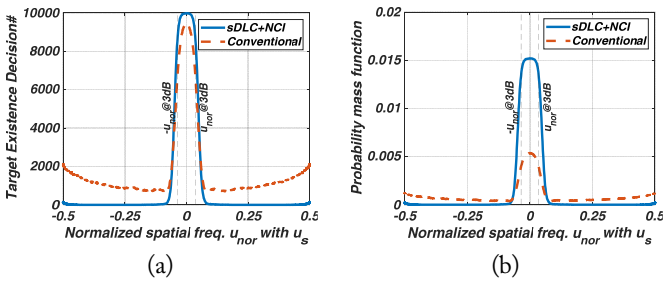


Fig. 10. Results for Case 2 (input target with $SNR_{main} = 13$ dB at u_{look}): Th 1 for the target with $SNR_{detectable} = 10$ dB. (a) number of decisions as the target in the mainlobe and (b) probability mass function of (a).

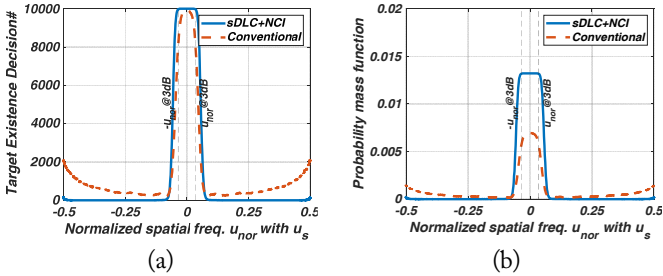


Fig. 11. Results for Case 3 (input target with $SNR_{main} = 16$ dB at u_{look}): Th 1 for the target with $SNR_{detectable} = 10$ dB. (a) number of decisions as the target in the mainlobe and (b) probability mass function of (a).

Table 4. Partial sum of $f_{tgtML}(u_i)$ within $\pm u_{3dB}$ (Th 1)

Input target	SNR_{main} at u_{look} (dB)	$\sum_i^{\pm u_{3dB}} f_{tgtML}(u_i)$	
		sDLC+NCI	Conventional
Case 1	10	0.75	0.17
Case 2	13	0.70	0.23
Case 3	16	0.62	0.31

Th 1 (dB) = 7.50 (sDLC+NCI), 5.40 (Conventional).

by 3,628 at $\pm u_{3dB}$ and by 3,259 at u_{look} . Despite the 3 dB lowered threshold of Th 1, blanking error is rare in the blanking region unlike in the results of "Conventional", thereby guaranteeing the superior reliability compared to Th 2. Furthermore, Cases 2–3 for Th 1 have perfect decisions of 10,000 within the detection region, and the distribution shapes become maximally clipped in the detection region by perfect decisions in Figs. 10 and 11. Note that the partial sums of "sDLC + NCI" decrease from the values for Th 2 in Table 3 to the values for Th 1 in Table 4. Since perfect decisions of the target-in-mainlobe are taken beyond the detection region, not within the detection region. In other words, reliability of Th 1 is only numerically low, and the performance is better than that of Th 2.

V. CONCLUSION

This study proposes the synthesis method for a robust SLB channel for low-RCS targets. This method is simply implementable to be expansible for adaptive beamforming. This method generates a distinguishable angular pattern with respect to the mainlobe and the sidelobe compared to the pattern of the main beam channel. The corresponding SLB ratio has remarkably changeable values with respect to the u domain, since it is increased at u_{look} by sDLC and decreased in the sidelobe region by the non-coherent integrator.

We also formulated an SLB-ratio function of u , SNR_{in} , and the spatial frequency response and then estimated a suitable SLB threshold for the low-RCS target. The proposed SLB provides much better overall performance than the conventional SLB for various targets scenarios, especially reliability across u . Since the difference between the SLB ratio and the SLB threshold is ensured sufficiently by sDLC.

The proposed SLB also provides appropriate threshold for a low-RCS input target, guaranteeing both superior reliability without blanking error and the high detectability of the target-in-mainlobe in the detection region. The suitable threshold for a low-RCS target improved the SLB performance by more than 30% compared to the threshold for the typical minimum-detectable target. Furthermore, it improved reliable detectability in the detection region while guaranteeing blanking ability in the blanking region with a negligible error of under 0.15.

In contrast, even for the minimum-detectable target, the conventional channel exhibited a huge error of more than 0.75 in the blanking region. The blanking error of the threshold for a low-RCS target became more severe, increasing up to 0.83. Therefore, the conventional SLB cannot provide reliable performance for a low-RCS target. As a result, we focused on the novel synthesis of an SLB channel for a low-RCS target.

We applied a cos-shaped element pattern to the actual array modeling. However, there are more considerable realistic errors,

such as errors by the Swerling target model, physical array error of mutual coupling, and inaccurate calibration. These challenges can be addressed by sufficient SLB ratio differences owing to spatial DLC, which can be easily implemented. Therefore, we can consider developing it in complex antenna systems, such as sub-arrays or planar arrays, based on the synthesis proposed in this study.

REFERENCES

- [1] L. Maisel, "Performance of sidelobe blanking systems," *IEEE Transactions on Aerospace and Electronic Systems*, vol. 4, no. 2, pp. 174-180, 1968.
- [2] A. Farina, *Antenna-Based Signal Processing Techniques for Radar Systems*. Boston, MA: Artech House, 1992.
- [3] D. E. Dudgeon, "Fundamentals of digital array processing," *Proceedings of the IEEE*, vol. 65, no. 6, pp. 898-904, 1977.
- [4] B. D. Van Veen and K. M. Buckley, "Beamforming: a versatile approach to spatial filtering," *IEEE ASSP Magazine*, vol. 5, no. 2, pp. 4-24, 1988.
- [5] D. G. Manolakis, V. K. Ingle, and S. M. Kogon, *Statistical and Adaptive Signal Processing*. Boston, MA: Artech House, 2005.
- [6] E. J. Kelly and K. Forsythe, "Adaptive detection and parameter estimation for multidimensional signal models," Lincoln Laboratory, Massachusetts Institute of Technology, Cambridge, MA, Technical Report No. 848, 1989.
- [7] C. D. Richmond, "Performance of the adaptive sidelobe blanker detection algorithm in homogeneous environments," *IEEE Transactions on Signal Processing*, vol. 48, no. 5, pp. 1235-1247, 2000.
- [8] U. Nickel, "Design of generalised 2D adaptive sidelobe blanking detectors using the detection margin," *Signal Processing*, vol. 90, no. 5, pp. 1357-1372, 2010.
- [9] U. Nickel, "Array processing for radar: achievements and challenges," *International Journal of Antennas and Propagation*, vol. 2013, article no. 261230, 2013. <https://doi.org/10.1155/2013/261230>
- [10] Y. H. Jang and W. W. Kim, "Optimization of the pulse canceler-based digital beamforming for sidelobe blanking," in *Proceedings of the Summer Annual Conference of IEIE 2017*, Busan, Korea, 2017, pp. 783-785.
- [11] Y. H. Jang and W. W. Kim, "A study on the SLB channel of planar array system using the spatial DLC," presented at the Summer Annual Conference of KIESS 2017, Jeju, Korea, 2017.
- [12] Y. H. Jang and W. W. Kim, "Synthesis method for the adaptive SLB channel based on the spatial DLC," *The Journal of Korean Institute of Electromagnetic Engineering and Science*, vol. 29, no. 8, pp. 608-614, 2018.
- [13] Y. H. Jang and D. Cho, "Performance evaluation of the optimized SLB channel for small target," presented at the Summer Annual Conference of KIESS 2021, Jeju, Korea, 2021.
- [14] A. V. Oppenheim, J. R. Buck, and R. W. Schaffer, *Discrete-Time Signal Processing*, 2nd ed. Upper Saddle River, NJ: Prentice Hall, 1999.
- [15] A. V. Oppenheim, A. S. Willsky, and S. H. Nawab, *Signals and Systems*, 2nd ed. Upper Saddle River, NJ: Prentice Hall, 1997.
- [16] J. G. Proakis and D. G. Monolakis, *Digital Signal Processing: Principles, Algorithms and Applications*, 3rd ed. Upper Saddle River, NJ: Prentice-Hall, 1995.
- [17] S. W. Smith, *The Scientist and Engineer's Guide to Digital Signal Processing*. San Diego, CA: California Technical Publishing, 1997.
- [18] D. Brandwood, *Fourier Transforms in Radar and Signal Processing*. Boston, MA: Artech House, 2003.
- [19] M. A. Richards, *Fundamentals of Radar Signal Processing*. New York, NY: McGraw-Hill, 2005.
- [20] D. K. Barton, *Radar System Analysis and Modeling*. Boston, MA: Artech House, 2005.
- [21] Wikipedia, "Probability mass function," 2022 [Online]. Available: https://en.wikipedia.org/wiki/Probability_mass_function.

Youn-Hui Jang



received her B.S. and M.S. degrees in Electronic Engineering from Chung-Ang University, Seoul, Korea, in 1999 and 2002. Since January 2002, she has been working as a researcher at the Agency for Defense Development, Daejeon, Republic of Korea. She is currently pursuing her Ph.D. degree in the Department of Electronics Engineering, Chungnam National University, Daejeon, Republic of Korea.

Her research interests include radar signal processing, array processing, cognitive radar, and deep learning.

Donghyeon Cho



received his Ph.D. degree from the Electrical and Electronics Engineering Department, KAIST, Daejeon, Republic of Korea, in 2019. He was a full-time student intern with Microsoft Research Asia and a researcher at the AI Center, SK-Telecom. He is currently an assistant professor in the Department of Electronics Engineering, Chungnam National University, Daejeon, Republic of Korea. His research

interests include computer vision and deep learning.

GPR Image Recovery Effect on Faster R-CNN- Based Buried Target Detection

Deniz Kumlu*

Abstract

Measurements acquired through ground-penetrating radar (GPR) may contain missing information that needs to be recovered before the implementation of any post-processing method, such as target detection, since buried target detection methods fail and cannot produce desired results if the input GPR image contains missing information. This study proves that the recovery of missing information in a GPR image has a direct influence on the performance of subsequent target detection methods. Thus, state-of-the-art matrix completion methods are applied to the GPR image with missing information in both pixel- and column-wise cases with different missing rates, such as 30% and 50%. After the GPR image is successfully recovered, the faster region-based convolutional neural network (Faster R-CNN) target detection method is applied. The performance correlation between matrix completion accuracy and the target detection method's confidence score is analyzed using both quantitative and visual results. The obtained results demonstrate the importance of GPR image recovery prior to any post-processing implementation, such as target detection.

Key Words: Buried Target Detection, Deep Learning, Faster R-CNN, Low Rank Data Recovery, Matrix Completion.

I. INTRODUCTION

Ground-penetrating radar (GPR) is a non-destructive electromagnetic system that allows the imaging of subsurface objects. The advantage of GPR is that it senses any kind of material based on variations in its dielectric permittivity and electrical conductivity. As long as the aforementioned responses of buried materials are different from their surroundings, the measured GPR image will contain enough information to distinguish the buried material signature, namely the target, from its surrounding environment [1].

The basic principle of GPR is based on sending and receiving electromagnetic pulses. In one iteration, a 1D signal containing many numbers is obtained, which varies with respect to the die-

lectric permittivity and electrical conductivity of the penetrated environment. This 1D signal is called an A-scan. When the GPR antenna is used to scan a certain area, many A-scans are collected and concatenated next to each other to construct a 2D signal, which is called the B-scan or the GPR image. Generally, missing data recovery and target detection methods are implemented on GPR images [1].

However, the GPR-based buried target detection concept also faces various challenges. The GPR measurement procedure is highly vulnerable to cases such as difficulty accessing some regions (because of obstacles or other inhibitory factors), highly damaged or corrupted A-scans during data collection, data with clutter that makes buried objects less visible, failures during measurements, or other instrumental problems.

Manuscript received February 19, 2022 ; Revised May 8, 2022 ; Accepted June 28, 2022. (ID No. 20220219-018J)

Department of Electronics and Communication, Istanbul Technical University, Istanbul, Turkey.

*Corresponding Author: Deniz Kumlu (e-mail: kumlud@itu.edu.tr)

This is an Open-Access article distributed under the terms of the Creative Commons Attribution Non-Commercial License (<http://creativecommons.org/licenses/by-nc/4.0>) which permits unrestricted non-commercial use, distribution, and reproduction in any medium, provided the original work is properly cited.

© Copyright The Korean Institute of Electromagnetic Engineering and Science.

As a result of these issues, partial missing information is a very likely characteristic of GPR measurements [2].

Moreover, missing information leads to poor identification, detection, and analysis of the measured GPR image [3]. Various matrix completion methods have been introduced in the literature, especially in the image processing domain as inpainting methods. They have also been successfully implemented for seismic data recovery issues [3–6]. Generally, these methods are based on interpolation [4], low-rank matrix completion [5], or, more recently, on deep learning-based [6] approaches.

Among these approaches, the low-rank matrix completion-based ones are the most popular. Many techniques have been proposed for low-rank-based matrix completion, such as convex relaxation, gradient, and alternating minimization-based algorithms [7–10]. In one study [7], the available methods were applied to missing information cases in GPR images and a detailed analysis of the various cases was presented. Among the applied methods, the low-rank matrix fitting (LmaFit) [8], nuclear norm minimization (NNM) [9], and non-negative matrix completion (NMC) [10] showed better performance compared to the others and proved their superiority even in extreme cases of missing information in GPR images. Drawing on the above results, this study focused on these three best-performing methods for matrix completion on pixel- and column-wise missing cases with various missing rates.

The region-based convolutional neural network (R-CNN) is one of the most common deep learning architectures used for object detection. Over time, it evolved into Fast R-CNN and Faster R-CNN [11]. The latter integrates a region proposal network (RPN) to produce region proposals directly in the network instead of using an additional algorithm, such as edge boxes. The RPN structure utilizes anchor boxes for object detection. Using region proposals in the network is a faster and better way to converge the loss function with the training data. Because of its model accuracy and end-to-end structure, RPN is used in a wide range of object detection solutions, even in GPR images. Faster R-CNN presents higher accuracy for buried target detection in GPR images, even with a small training dataset [12]. However, in order to implement Faster R-CNN, the GPR image has to be in its proper form (no measurement failures/missing information, as previously discussed). If there are any missing regions in the GPR image because of corrupted A-scans, Faster R-CNN fails to detect the buried target, even if target signature is partially observed. Thus, some pre-processing operations are required for the purpose of presenting a reasonable confidence score for buried object detection.

In this study, we propose a novel framework using cascading matrix completion methods with deep learning-based buried target detection. In our implementation, GPR images with various pixel- and column-wise missing rates are recovered using

three different matrix completion methods—LmaFit, NNM, and NMC. After this, the results are fed into the Faster R-CNN for buried target detection purposes. The relation between the matrix completion performance and confidence score of the target detection is analyzed, and both quantitative and visual results are presented.

The rest of this paper is organized as follows: in Section II, the related research on matrix completion approaches is presented. Section III introduces Faster R-CNN-based buried target detection. Section IV is dedicated to explaining the proposed method. In Section V, the visual and quantitative results are presented. Finally, Section VI concludes the paper.

II. GPR IMAGE RECOVERY

Image recovery methods are extensively applied to image processing problems in different scenarios, such as cases of pixel-wise and column-wise missing information [3]. However, in GPR measurements, column-wise missing cases (missing A-scans) are significantly more common than pixel-wise missing cases. Thus, this study primarily focused on the column-wise missing cases, since they are more challenging. In the experimental results section of this study, two different column-wise and one pixel-wise missing cases are presented.

An important step should be followed in the case of column-wise missing information before the implementation of any matrix completion method. According to matrix completion theory, at least one observation for each row and column is necessary [3] (this is not applicable for pixel-wise missing cases). Thus, a pre-transformation step must be applied to the input GPR image with missing information to address this. One study [7] proposed dividing the GPR image into smaller patches, such as 3×3, followed by vectorizing and concatenating them to construct a new input matrix for the GPR image recovery methods, as described in Fig. 1.

Three methods are selected for the matrix completion of the GPR images based on their superior performances [7]—LmaFit [8], NNM [9], and NMC [10]. While each of these methods has its own unique theory, we briefly describe the matrix completion theory in this study. More details on the methods can be found in the literature [8–10].

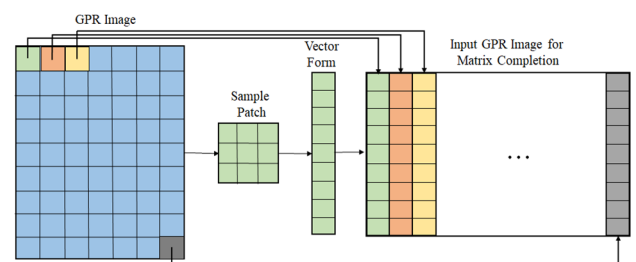


Fig. 1. Block diagram of pre-transformation for matrix completion.

$X \in \mathbb{R}^{M \times N}$ represents the raw GPR image, while $Y \in \mathbb{R}^{M \times N}$ denote the GPR image with missing entries in column-wise or pixel-wise cases, respectively. Meanwhile, M and N are the dimensions of X and Y , namely time (ns) and distance (cm) locations. Recovering the exact low-rank matrix can thus be expressed by the following minimization function:

$$\min_X \text{rank}(X), \quad s. t. \quad X_{ij} = Y_{ij}, \quad \forall (i, j) \in \Omega \quad (1)$$

Here, $\text{rank}(\cdot)$ denotes the rank of the GPR image X , while Ω stands for an index subset corresponding to the observed entries. i and j are the index values.

We define the projection operator $P_\Omega: \mathbb{R}^{M \times N} \rightarrow \mathbb{R}^{M \times N}$ as follows:

$$[P_\Omega(X)]_{ij} = \begin{cases} X_{ij}, & (i, j) \in \Omega \\ 0, & \text{otherwise} \end{cases} \quad (2)$$

Here, P_Ω represents the projection on the observation subspace of the matrices, with non-zero entries constrained to the index subset Ω .

If the GPR image Y is low-rank and its singular vectors are sufficiently spread, the missing locations can be recovered by implementing the following minimization function:

$$\min_Z \text{rank}(Z), \quad s. t. \quad \|P_\Omega(Z - Y)\|_F \leq \delta \quad (3)$$

In the above equation, Z denotes an unknown variable matrix, $\|\cdot\|_F$ stands for the Frobenius norm, and δ is the tolerance parameter. Furthermore, since the problem in Eq. (3) is NP-hard, it can be relaxed to form a convex optimization problem, expressed as follows:

$$\min_Z \|Z\|_*, \quad s. t. \quad \|P_\Omega(Z - Y)\|_F \leq \delta \quad (4)$$

Here, $\|Z\|_*$ represents the nuclear norm. The general optimization problem in Eq. (4) can be solved through a matrix completion problem. In this study, LmaFit, NNM, and NMC are used for the completion. The details of the methods are presented in Table 1.

III. FASTER R-CNN-BASED BURIED TARGET DETECTION

The R-CNN, which uses selective search strategies and creates regional proposals for each target image, is one of the most popular object detection models. After constructing the

region proposals, features from these proposals are extracted through the CNN architecture. The last step of the R-CNN model is the classification and localization of the target object. After implementing these processes, the target location is presented by the bounding box around it. The introduction of Fast R-CNN adds a new layer—the region of interest (ROI) pooling—which enables the utilization of a single feature map for all proposals extracted using selective search algorithms [11].

ROI pooling solves one of the fundamental problems of fixed image size requirement for object detection observed in previous methods. It can solve recalculating problems resulting from the different sizes of the features. With this new addition to the Fast R-CNN, similar accuracy is obtained with faster training and inference time. However, both R-CNN and Fast-RCNN use selective searches to identify the region proposals. The selective search strategy is a tedious and time-consuming process that has a negative effect on the performance of the network.

In Faster R-CNN, similar to Fast R-CNN, the image is given as an input to a convolutional network that produces a convolutional feature map. However, in Faster R-CNN, instead of using the selective search algorithm on a feature map to define region proposals, it is predicted by a separate network. It is then reshaped by the ROI pooling layer. In the final step, the image within the proposed region is classified to predict the bounding box. As a result, a much faster architecture is obtained compared to its predecessors [11].

1. Training the Faster R-CNN on Simulated GPR Data

CNNs generally consist of convolutional layers, pooling layers, and fully connected layers.

The CNN model in this study includes 3 convolutional layers with dimensions of 16, 32, and 64, with a 5×5 kernel size (rectified linear unit [ReLU] is used as the activation function and 2×2 maxpooling layer is applied in every convolutional layer). They are fed into one fully connected layer with 64 neurons. The Cifar-10 dataset is selected for pre-training. The simulated GPR images are then used to train the Faster R-CNN, which utilizes pre-trained CNN weights [12].

The simulated dataset is constructed using the gprMax simulation software [13], consisting of 55 simulated GPR images with different burial depths, soil types, object materials, and surface types. This simulated dataset is split as follows: 40 are used for training, 10 are used for validation, and the remaining 5 are used for testing purpose.

Table 1. Conventional matrix completion methods

Category	Method	Main technique
Matrix factorization [8]	LmaFit	Alternating
Rank minimization [9]	NNM	SVD
Matrix factorization [10]	NMC	Alternating

IV. PROPOSED METHOD

The block diagram of the proposed method, depicted in Fig. 2, is constructed by cascading the methods explained in Sections II and III. First, the GPR image recovery or matrix completion

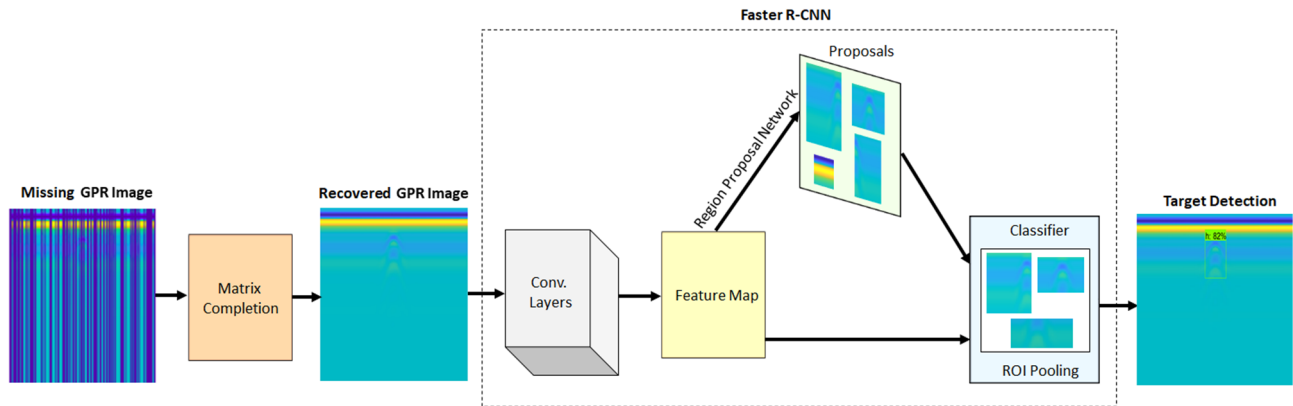


Fig. 2. Block diagram of the proposed method.

methods (LmaFit [8], NNM [9], and NMC [10]) are applied to the missing GPR image in both the pixel- and column-wise missing cases. The obtained GPR image may contain artifacts over the target region after the recovery process. If the input GPR image in Fig. 2 has no missing information, the matrix completion methods will not have any adverse effect on it (almost the same input GPR image is obtained). Since they are sufficiently fast, applying the matrix completion methods at the beginning of the target detection process does not lead to additional costs for the proposed model.

The recovered GPR image is then fed to the Faster R-CNN network, which is already trained for buried target detection in GPR images (during the training process, GPR images do not contain any missing information). At the end of the network, we obtain the bounding box around the buried target along with its confidence score. The obtained target detection score with Faster R-CNN is directly related to the input of the network, which means the quality of the recovered GPR image (especially the target signature with a hyperbolic shape) via matrix completion algorithms. This indicates that well-recovered GPR images at the input of the network eventually lead to good target detection performances.

V. EXPERIMENTAL RESULTS

In this study, simulated GPR images with missing information for both the pixel- and column-wise cases are used for matrix completion purposes. The Faster R-CNN-based buried target detection model is applied to the recovered GPR images. The simulated data are produced by using the gprMax simulation software [13]. Some of the pixels or A-scans are deleted deliberately for recovery purposes in the obtained simulated data. Since the pixels are deleted manually, the information from the original GPR image is still available for quantitative comparison. Moreover, both visual and quantitative results are analyzed during the comparison. To be more precise, the recovered target signatures are zoomed into in the case of the visual results, and both

the peak signal-to-noise ratio (PSNR) and structural similarity index measure (SSIM) are presented in the quantitative comparisons.

The simulated data are constructed as follows: the buried target is a single aluminum with a dielectric constant (F/m) of 3.1 and conductivity (S/m) of 2.3×10^7 . Additionally, the surface and soil types are considered flat and dry sandy soil, respectively, with the latter having a dielectric constant (F/m) of 3.0 and conductivity (S/m) of 0.001. The experimental design of the simulated GPR images is depicted in Fig. 3, which clearly shows the aluminum disk—with dimensions $2.5 \text{ cm} \times 2 \text{ cm}$ in radius and height and a burial depth of 2 cm. Antennas are placed 5 cm above the ground and moved 1 cm in each simulation to obtain the A-scan. In each scenario, antennas are moved 80 times to obtain the GPR image; thus, there are 80 A-scans, with each A-scan containing 256 samples. Effectively, the final obtained B-scan or GPR image has a size of 256×80 . A 1.5-GHz antenna type (Model 5100; Geophysical Survey Systems Inc., Nashua, NH, USA) is selected, which is frequently used in real GPR measurements. The sample simulated GPR image obtained from gprMax is presented in Fig. 4(a). The ideal burial environment (dry sand soil) is selected for the aluminum target (highly reflective). As a result, the target signal can be clearly observed as a hyperbolic structure in the raw GPR image. The target region size is arranged as 70×40 , as noted in the shaded region in Fig. 5(b).

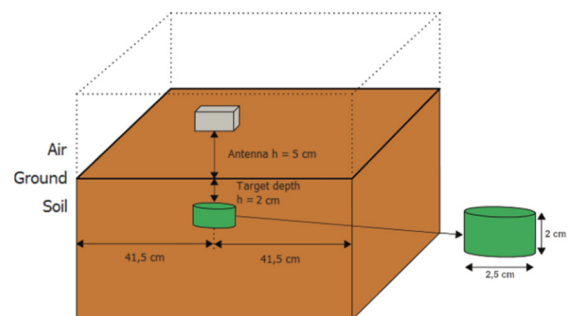


Fig. 3. Experimental design of the simulated dataset.

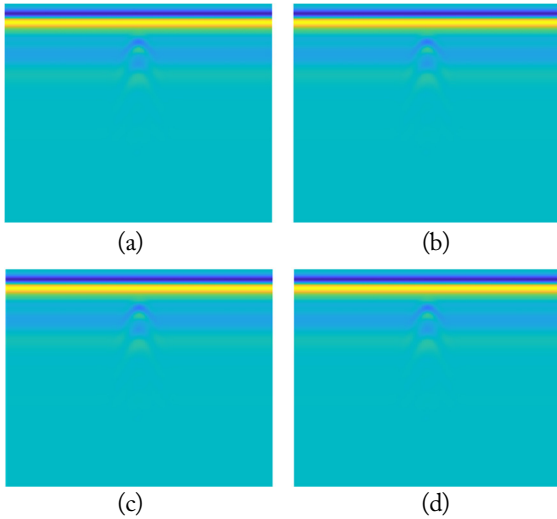


Fig. 4. (a) Simulated raw GPR data, and results for (b) LmaFit, (c) NNM, and (d) NMC.

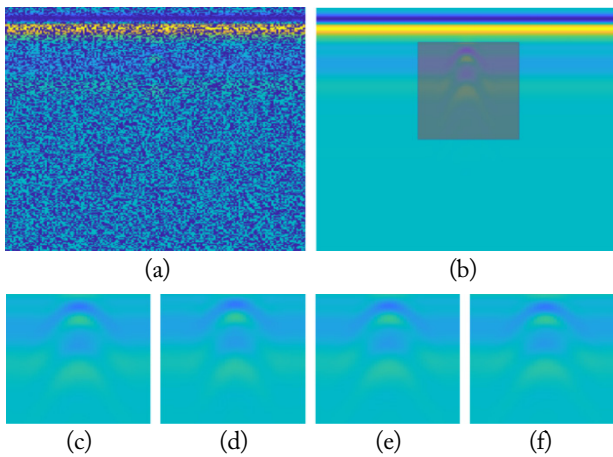


Fig. 5. (a) Raw GPR image (30% pixel-wise missing data case), (b) original raw GPR image and zoomed-in regions of the recovered target signature: (c) original target, results for (d) LmaFit, (e) NNM, and (f) NMC.

Before the matrix completion results are presented, the effects of the methods are analyzed for cases where the input image has no missing pixels or columns. The outputs of the methods for LmaFit, NNM, and NMC are shown in Fig. 4(b)–4(d). As observed in Fig. 4, if the input GPR image has no missing region, the matrix recovery methods will have no adverse effect on the image. Thus, these methods can be safely used before implementing any target detection algorithm.

As mentioned before, pixel- and column-wise missing information cases are chosen for matrix recovery methods, wherein the latter is more common and challenging. For the pixel-wise missing information case, the missing rate is arranged as 50%, as presented in Fig. 5(a). The 30% missing rate analysis is skipped for the pixel-wise case since it is a relatively simple case for the matrix completion methods [7]. For the column-wise missing

information cases, missing rates are arranged at 30% and 50%, as presented in Fig. 6(a) and Fig. 7(a), respectively. In Fig. 5(a), the target signature is not visible in the missing GPR image, and the target signature is radically corrupted. Furthermore, in Fig. 6(a), the target signature is barely visible. However, in Fig. 7(a), the effects of the missing regions are more severe, while the target signature is also not visible in the missing GPR image.

The simulated raw GPR images in Fig. 4 do not exhibit much variation in the background, with the most significant part of the images being their target signatures, which have a hyperbolic shape. For the visual results of the GPR image recovery methods, the zoomed-in areas for the target signature are presented. To avoid repetition, the GPR image recovery results for the whole GPR image are presented in Figs. 8(b)–8(d), 9(b)–9(d), and

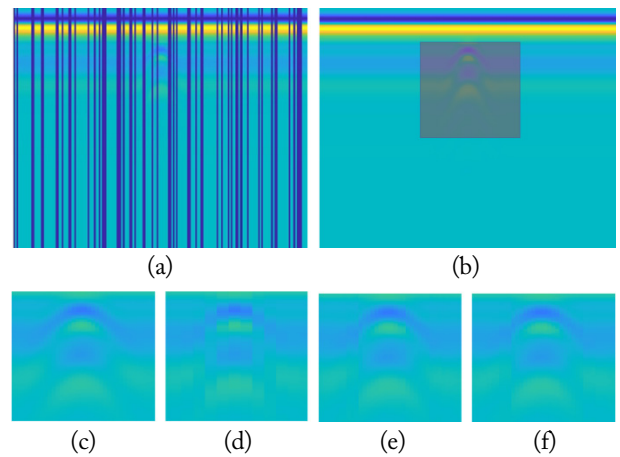


Fig. 6. (a) Raw GPR image (30% column-wise missing data case), (b) original raw GPR image and zoomed-in regions for the recovered target signature: (c) original target, results for (d) LmaFit, (e) NNM, and (f) NMC.

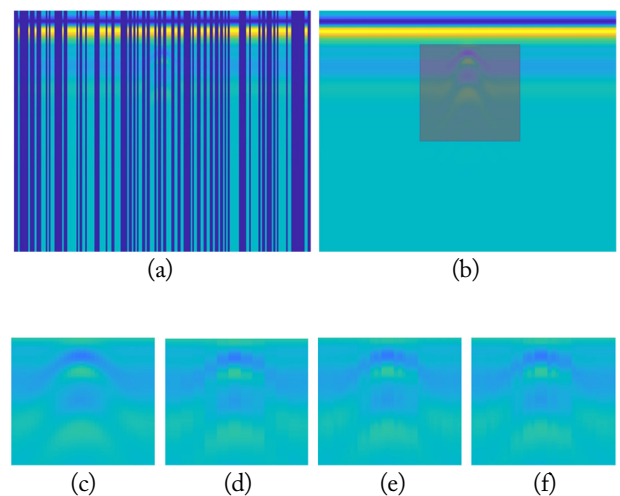


Fig. 7. (a) Raw GPR image (50% column-wise missing data case), (b) original raw GPR image and zoomed-in regions for the recovered target signature: (c) original target, results for (d) LmaFit, (e) NNM, and (f) NMC.

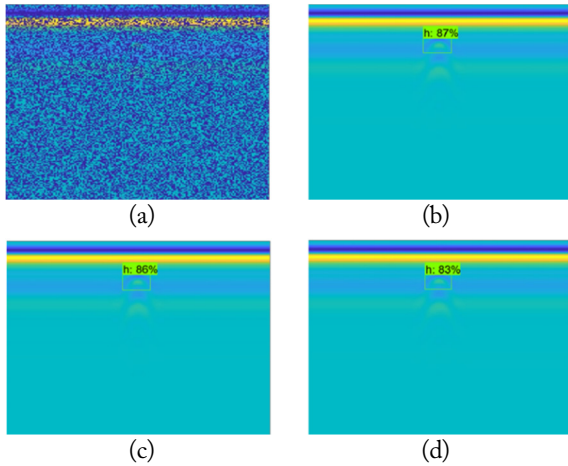


Fig. 8. Faster R-CNN-based target detection results for 50% pixel-wise missing information case: (a) missing GPR image and recovered GPR images through (b) LmaFit, (c) NNM, and (d) NMC.

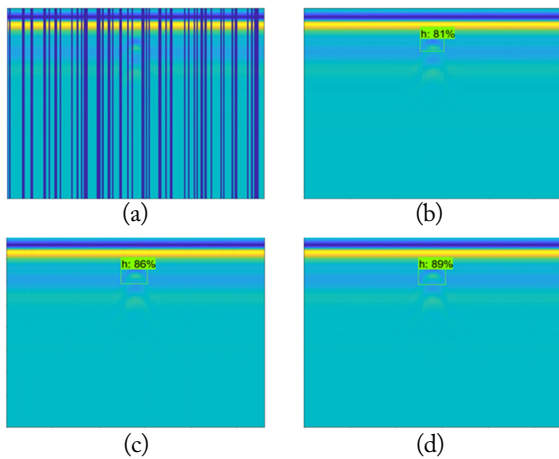


Fig. 9. Faster R-CNN-based target detection results for 30% column-wise missing information case: (a) missing GPR image and recovered GPR images through (b) LmaFit, (c) NNM, and (d) NMC.

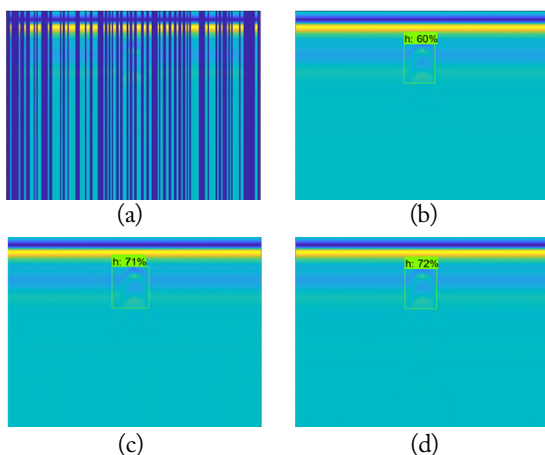


Fig. 10. Faster R-CNN-based target detection results for 50% column-wise missing information case: (a) missing GPR image and recovered GPR images through (b) LmaFit, (c) NNM, and (d) NMC.

10(b)–10(d). Fig. 5(c)–5(f) present the original and recovered target signatures. As discussed before, the pixel-wise missing case scenario is simpler than the column-wise case. Thus, all the methods recovered the GPR image sufficiently well. It is difficult to identify the performance differences from the visual results for the pixel-wise missing information case. Thus, similar performances are expected from the recovered images in the target detection section.

For the column-wise missing case, two different missing information rates are applied to identify the limitations of the methods. For the 30% missing case, as depicted in Fig. 6(a), the LmaFit presents some blocking effects while the NNM and NMC exhibit better recovery results, as observed in Fig. 6(d)–6(f). For the 50% missing case in Fig. 7(d)–7(f), all the algorithms exhibit a blocking effect. However, LmaFit encounters a more severe blocking effect compared to the others, which is not a desirable characteristic. The NNM and NMC, considering the visual aspect, show similar performances and better recoveries for the target section. However, the NMC is clearly better at recovering the target signature compared to the NNM method, as observed when the recovered signatures are sufficiently zoomed in.

The quantitative results of the pixel-wise missing information case are presented in Tables 2 and 3 for both the target signature and the whole GPR image (as discussed before, the target signature recovery score is significant for the target detection part). Both the SSIM and PSNR scores are used for the detailed quantitative analysis. As seen in Tables 2 and 3, LmaFit obtained better results compared to the NNM and NMC methods. However, all the PSNR scores are quite high—thus satisfying (compared to the column-wise recovery scores) the requirements for the target detection part. We did not expect much variation in the target detection results from the obtained quantitative results for the pixel-wise missing case, since all the values are sufficiently high and can be accepted as a reasonable input

Table 2. Matrix completion results of pixel-wise missing cases for zoomed GPR images

	Missing rate (%)	LmaFit	NNM	NMC
SSIM	50	1.0000	0.9995	0.9962
PSNR	50	74.67	59.59	50.81

Table 3. Matrix completion results of pixel-wise missing cases for overall GPR images

	Missing rate (%)	LmaFit	NNM	NMC
SSIM	50	0.9785	1.0000	0.9997
PSNR	50	72.93	69.47	62.13

for target detection.

The column-wise missing information case results are presented in Tables 4 and 5, where the PSNR scores for the target signature are higher in the 30% missing case and deteriorates in the 50% missing case, where it is far more severe. Thus, increasing the missing information rate causes a degradation in the recovered target signature. When the performance of the methods for the 30% missing case is investigated, it can be observed that the LmaFit has the worst performance among all the methods for both the target signature and the whole GPR image. Notably, the NMC clearly outperforms the NNM, with an approximately 9% better performance in the PSNR. For the 50% missing case, which is quite extreme for the column-wise case, all three methods exhibit very similar performances. However, the NMC again exhibits the best performance for both the target signature and the whole GPR image.

Target detection results based on Faster R-CNN for the 50% pixel-wise missing case are presented in Fig. 8(a)–8(d). As seen in Fig. 8(a), if the GPR image has missing regions, Faster R-CNN fails to detect the target signature (since it is not trained for different missing information cases). However, for the recovered GPR images in Fig. 8(c)–8(d), Faster R-CNN is able to locate the target signature with varying confidence scores, showing very little difference, as expected. All the methods obtained high recovery scores, considering the PSNR for the pixel-wise missing data case. The scores are 87% for LmaFit, 86% for NNM, and 83% for NMC. The comparatively highest and lowest detection scores are obtained by LmaFit and NMC, respectively. As predicted, these results coincide with the recovery results presented in Tables 2 and 3.

Fig. 9(a)–9(d) present the target detection results for the 30%

Table 4. Matrix completion results for different rates of column-wise missing cases for zoomed GPR images

	Missing rate (%)	LmaFit	NNM	NMC
SSIM	30	0.9991	0.9998	0.9998
	50	0.9989	0.9990	0.9990
PSNR	30	38.33	44.11	44.85
	50	37.25	37.70	37.78

Table 5. Matrix completion results for different rates of column-wise missing cases for overall GPR images

	Missing rate (%)	LmaFit	NNM	NMC
SSIM	30	0.9984	0.9984	0.9996
	50	0.9982	0.9969	0.9984
PSNR	30	50.38	54.43	59.61
	50	49.53	49.30	50.43

column-wise missing information case. As discussed before, the target is not detected for the missing scenario in Fig. 9(a). For the recovered GPR images in Fig. 9(b)–9(d), the confidence scores are 81% for LmaFit, 86% for NNM, and 89% for NMC. The highest and lowest detection scores are obtained by NMC and LmaFit, respectively. These detection results coincide with the GPR image recovery results presented in Tables 4 and 5.

Fig. 10(a)–10(d) depict the detection results for the extreme case of 50% column-wise missing information. Fig. 10(a) shows that the target is barely visible, indicating that Faster R-CNN cannot detect the target. The LmaFit has the lowest score of 60%, as seen in Fig. 10(b), since the target signature and background contain distortions, which affect the target detection performance. In contrast, the NNM and NMC results in Fig. 10(c) and 10(d) show similar target detection performances of 71% and 72%, respectively.

Notably, the NMC exhibits a slightly better performance than the NNM. As observed in Tables 4 and 5, the NMC also has better recovery results, thus leading to a better detection performance. The results in Tables 4 and 5 and Figs. 9 and 10 prove the strong relation between them and emphasize the importance of cascading for better and more robust target detection results. By comparing the results of the 30% and 50% missing information cases, it can be asserted that higher missing information rates cause degradation of the confidence scores of the detected buried targets under Faster R-CNN.

VI. CONCLUSION

Three conventional image recovery methods (Lmafit, NNM, and NMC) are applied to missing GPR image scenarios for 50% pixel-wise and 30% and 50% column-wise missing cases. These methods are proposed as pre-processing methods to be implemented prior to any post-processing operations, such as clutter removal or target detection. The experiments reveal that the use of recovery methods does not cause any deterioration even when the original GPR image (that has no missing regions) is considered as the input. On the other hand, if a corrupted GPR image is fed into the Faster R-CNN as input, the buried object cannot be detected. To prove this, both missing and recovered GPR images are fed to the Faster R-CNN-based target detection model. The obtained detection results from the missing and recovered GPR images demonstrate that the target can be detected in the recovered GPR image, while the target in the missing GPR image cannot be detected. The experiments also prove that better recovery leads to better target detection results in GPR.

REFERENCES

- [1] D. J. Daniels, *Ground Penetrating Radar*, 2nd ed. London,

- UK: The Institution of Engineering and Technology, 2004.
- [2] D. Kumlu and I. Erer, "Clutter removal techniques in ground penetrating radar for landmine detection: a survey," in *Operations Research for Military Organizations*. Hershey, PA: IGI Global, 2009, pp. 375-399.
- [3] O. Lopez, R. Kumar, O. Yilmaz, and F. J. Herrmann, "Off-the-grid low-rank matrix recovery and seismic data reconstruction," *IEEE Journal of Selected Topics in Signal Processing*, vol. 10, no. 4, pp. 658-671, 2016.
- [4] X. F. Li and X. F. Li, "Seismic data reconstruction with fractal interpolation," *Chinese Journal of Geophysics*, vol. 51, no. 4, pp. 855-861, 2008.
- [5] R. H. Keshavan, A. Montanari, and S. Oh, "Matrix completion from a few entries," *IEEE Transactions on Information Theory*, vol. 56, no. 6, pp. 2980-2998, 2010.
- [6] D. Kumlu, K. Tas, and I. Erer, "Missing data recovery via deep networks for limited ground penetrating radar measurements," *Remote Sensing*, vol. 14, no. 3, article no. 754, 2022. <https://doi.org/10.3390/rs14030754>
- [7] D. Kumlu, "Ground penetrating radar data reconstruction via matrix completion," *International Journal of Remote Sensing*, vol. 42, no. 12, pp. 4607-4624, 2021.
- [8] Z. Wen, W. Yin, and Y. Zhang, "Solving a low-rank factorization model for matrix completion by a nonlinear successive over-relaxation algorithm," *Mathematical Programming Computation*, vol. 4, no. 4, pp. 333-361, 2012.
- [9] G. Shabat and A. Averbuch, "Interest zone matrix approximation," *The Electronic Journal of Linear Algebra*, vol. 23, pp. 678-702, 2012.
- [10] Y. Xu, W. Yin, Z. Wen, and Y. Zhang, "An alternating direction algorithm for matrix completion with nonnegative factors," *Frontiers of Mathematics in China*, vol. 7, no. 2, pp. 365-384, 2012.
- [11] S. Ren, K. He, R. Girshick, and J. Sun, "Faster R-CNN: towards real-time object detection with region proposal networks," *Advances in Neural Information Processing Systems*, vol. 28, pp. 91-99, 2015.
- [12] M. T. Pham and S. Lefevre, "Buried object detection from B-scan ground penetrating radar data using Faster-RCNN," in *Proceedings of 2018 IEEE International Geoscience and Remote Sensing Symposium*, Valencia, Spain, 2018, pp. 6804-6807.
- [13] C. Warren, A. Giannopoulos, and I. Giannakis, "gprMax: open source software to simulate electromagnetic wave propagation for ground penetrating radar," *Computer Physics Communications*, vol. 209, pp. 163-170, 2016.

Deniz Kumlu



received his B.S. degree from the Department of Electrical and Electronics Engineering, Turkish Naval Academy, Istanbul, Turkey, in 2007 with an honors degree. He completed his M.S. degree from the Ming Hsieh Department of Electrical Engineering, Viterbi School of Engineering, University of Southern California, Los Angeles, CA, USA, in 2012, where he studied with a special fellowship granted

by the Turkish Naval Forces. He obtained his Ph.D. degree from the Department of Electronic and Communication Engineering, Istanbul Technical University, Istanbul, Turkey, in 2018, with the best thesis of the year award. He is currently serving as a senior researcher in the private sector and also participates in research projects conducted at Istanbul Technical University. His research interests include image processing, signal processing, machine learning, deep learning, and GPR applications.

A Compact Dual-Band MIMO Antenna for Sub-6 GHz 5G Terminals

Guiting Dong · Jianlin Huang · Simin Lin · Zhizhou Chen · Gui Liu*

Abstract

In this paper, a dual-band multiple-input-multiple-output (MIMO) antenna is proposed for fifth-generation (5G) wireless communication terminals. The measured -10 dB impedance bandwidths of 380 MHz (3.34–3.72 GHz) and 560 MHz (4.57–5.13 GHz) can cover the 3.4–3.6 GHz and 4.8–5 GHz 5G bands. The single antenna element of this proposed MIMO is composed of an F-shaped feed strip and an inverted L-shaped radiation strip. A defected ground structure is employed to obtain a good isolation performance, whereby the measured isolation between the antenna elements is observed to be larger than 23 dB. The measured total radiation efficiencies at 3.5 GHz and 4.9 GHz are 76.65% and 71.93%, respectively. Besides, the calculated envelope correlation coefficients (ECC) are less than 0.00125 and 0.01164 at the low-frequency and high-frequency bands, respectively. Furthermore, the specific absorption ratio (SAR) analysis of the antenna verifies that it qualifies for 5G terminals.

Key Words: Dual Band, Fifth-Generation (5G), High-Isolation, MIMO Antenna, Planar Antenna.

I. INTRODUCTION

Due to fast-growing wireless communication technologies, fifth-generation (5G) mobile communication systems have been widely rolled out and used in several different applications in recent times. Compared to 4G systems, 5G promises to provide seamless connectivity with higher data rates and lower latency [1]. Two main frequency groups have been adopted in this context—sub-6 GHz and millimeter-wave (mm-wave) bands. Due to their longer wavelength, sub-6 GHz bands have stronger penetration and travel longer distances; as a result, they receive a lot of attention in relation to 5G communication systems.

The ever-increasing data capacity requirements and miniaturization trend of wireless communication devices pose a significant challenge to antenna design in terms of achieving a com-

pact size with high data rate handling capability. An effective way to solve this problem is to adopt multiple-input-multiple-output (MIMO) antenna technology, which improves both spectrum efficiency and data rates [2–4].

For the successful implementation of spatial diversity in a MIMO antenna system, strategies to decrease mutual coupling and improve isolation between the antenna elements are crucial. Many studies have focused on enhancing the isolation of MIMO antennas. Some MIMO antennas achieve good isolation by maintaining an appropriate distance between the antenna elements. In one study [5], mirror-imaged placement of the antenna elements and insertion of a chip inductor between closely spaced antennas were able to improve isolation. Apart from this, grounding branches can generate new coupling and affect isolation [6, 7]. The application of grounded branches can

Manuscript received February 26, 2022 ; Revised May 6, 2022 ; Accepted June 28, 2022. (ID No. 20220226-020J)

College of Electrical and Electronic Engineering, Wenzhou University, Zhejiang, China.

*Corresponding Author: Gui Liu (e-mail: gliu@wzu.edu.cn)

This is an Open-Access article distributed under the terms of the Creative Commons Attribution Non-Commercial License (<http://creativecommons.org/licenses/by-nc/4.0>) which permits unrestricted non-commercial use, distribution, and reproduction in any medium, provided the original work is properly cited.

© Copyright The Korean Institute of Electromagnetic Engineering and Science.

improve isolation in the lower frequency band and provide better impedance matching for the antenna [6]. Furthermore, a neutral line is often employed to weaken mutual coupling [8–10]. Connecting adjacent orthogonal pairs of antennas with a short neutral line leads to high isolation [10].

Additionally, defected ground structures (DGS) can improve isolation by affecting the circuit substrate’s effective dielectric constant distribution—this has become a commonly used technology for overcoming undesired coupling in MIMO antenna designs [11–14]. Some MIMO antennas use unique decoupling structures to improve isolation, such as the multi-slot decoupling structure [15], the generic decoupling structure composed of an array of H-shaped parasitic structures [16], and the rectangular microstrip stub [17].

Meanwhile, the antenna proposed in another study [18] used ungrounded full-wavelength strip resonators, which effectively enhanced the isolation between the antenna elements at the cost of reducing the impedance bandwidth. Meta-surface [19, 20] and electromagnetic band gap (EBG) structures [21–23] are also effective methods for improving isolation, although they are too complex to be used in miniaturized antennas. To sum up, the design methodology for achieving good isolation in a small-size MIMO antenna system continues to be a critical issue.

This paper presents a novel decoupling structure that utilizes a DGS to achieve high isolation of more than 23 dB. The DGS includes a rectangular slot with 42 circular slots located on each side. The antenna has a compact size of 28 mm × 28 mm × 0.8 mm, which is suitable for the miniaturization of sub-6 GHz 5G terminals. The proposed MIMO antenna covers both the 3.5 GHz (3.4–3.6 GHz) and 4.9 GHz (4.8–5.0 GHz) frequency bands. Furthermore, the measured total efficiencies at 3.5 GHz and 4.9 GHz are 76.65% and 71.93%, respectively. The calculated envelope correlation coefficients (ECC) is less than 0.00328 in both the desired frequency bands. Moreover, the simulated specific absorption ratio (SAR) values are all observed to be less than 1.4 in the dual bands, thus conforming to the standard for terminal equipment.

II. ANTENNA STRUCTURE

The configuration of the proposed antenna is illustrated in Fig. 1. The antenna elements are etched on an FR4 substrate with $\epsilon_r = 4.4$ and $\tan\delta = 0.02$, with the size of the substrate being 28 mm × 28 mm × 0.8 mm. The antenna element comprises an inverted L-shaped radiation strip and an F-shaped feeding strip. These two antenna elements are distributed diagonally symmetric to the substrate. Furthermore, each antenna element is fed with a 50-Ω microstrip feedline. The DGS contributes to weakening mutual coupling and enhancing isolation. The detailed dimensions of the antenna element are illustrated in Fig. 1(b).

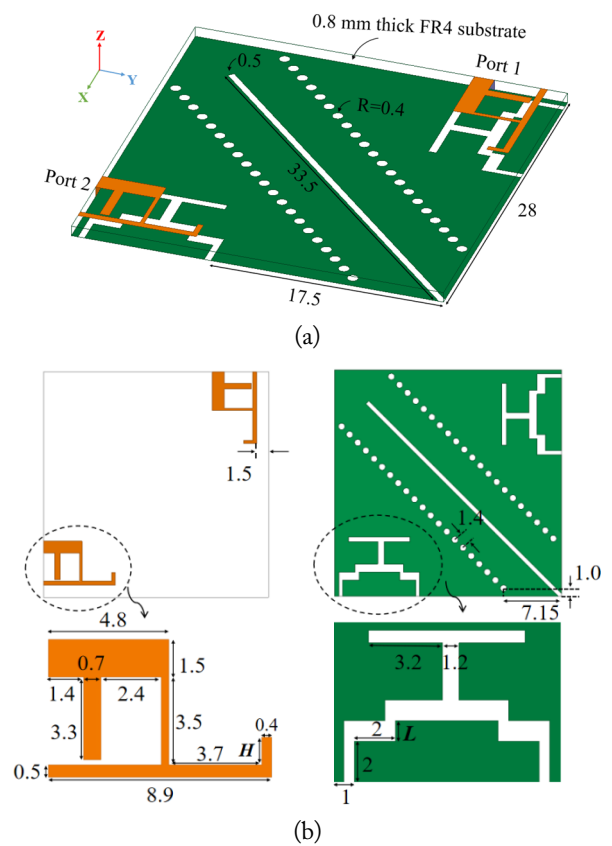


Fig. 1. The geometry of the proposed MIMO: (a) perspective view and (b) detailed dimensions of the antenna element antenna (unit: mm).

III. ANTENNA ANALYSIS

1. Design Evolution

Fig. 2 depicts the methodology for the design evolution of a

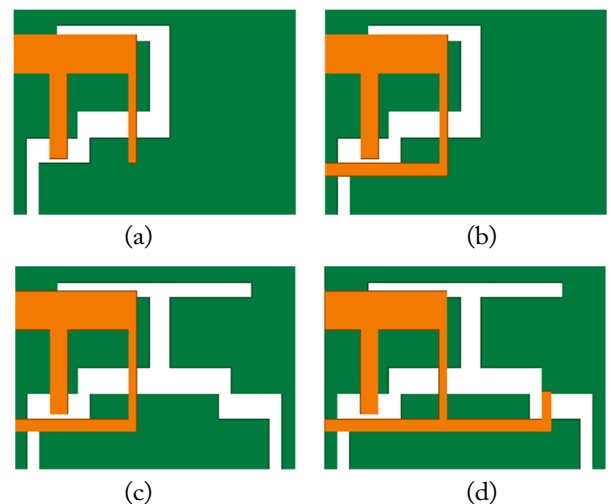


Fig. 2. The design evolution of a single MIMO antenna element: (a) Ant-1, (b) Ant-2, (c) Ant-3, and (d) Ant-4 (proposed antenna).

single MIMO antenna element. As shown in Fig. 3, the F-shaped structure of Ant-1 generates resonance in the lower frequency band. Ant-2, which is obtained by adding a rectangular patch to Ant-1, can excite two modified resonate modes. Meanwhile, Ant-3 modifies the etched slots of the ground plane and generates a symmetrical ground slot structure, which can change the antenna element's distribution parameters—reducing its distributed capacitance and resistance. Therefore, although Ant-3 enhances the resonance of the two bands, it has a negative effect on impedance matching. In Ant-4, however, the addition of the inverted L-shaped radiation strip improves the performance, enabling it to achieve qualified performance in both the desired frequency bands, which are 3.4–3.6 GHz and 4.8–5 GHz. The impedance of the different antenna structures, as shown in Fig. 4, shows the L-shaped radiation strip of Ant-4 increases resistance and achieves better impedance matching within the desired frequency bands.

2. Dimension Optimization

The surface current distributions of a single antenna element are depicted in Fig. 5. The surface current of 3.5 GHz is concentrated on the L-shaped radiation strip; hence, the resonance

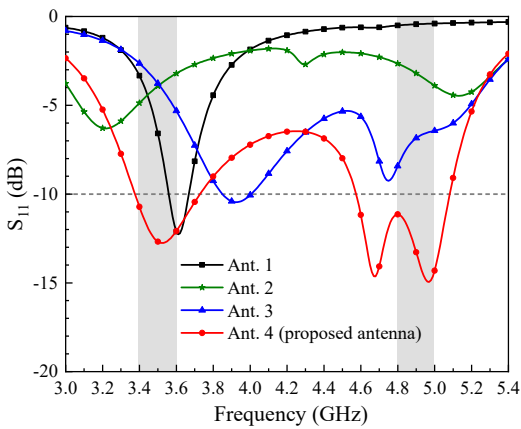


Fig. 3. S_{11} of the various antennas.

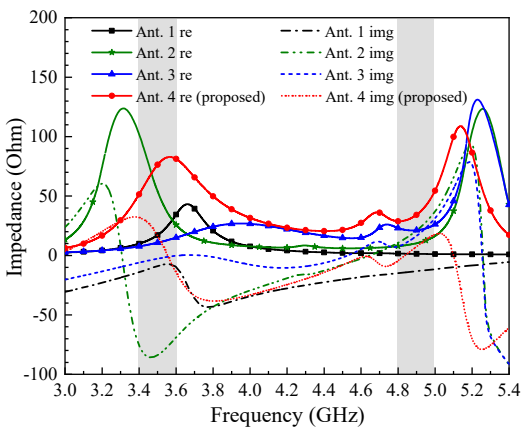


Fig. 4. Comparison of the impedance of the various antennas.

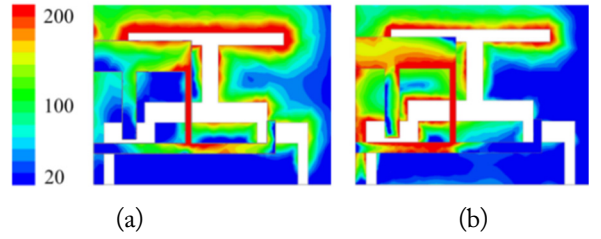


Fig. 5. The surface current distributions of the proposed antenna at (a) 3.5 GHz and (b) 4.9 GHz (unit: A/m).

of the 3.5 GHz band can be effectively adjusted by changing the length of the L-shaped radiation strip. Meanwhile, Fig. 5(b) depicts that the current at 4.9 GHz is concentrated on the F-shaped feed strip and its corresponding ground slot structure. Therefore, modifying the structure of the slot at the corresponding position can significantly affect the performance of the antenna in the higher frequency band.

The simulated S_{11} parameters of different values of H and L (as shown in Fig. 1) are depicted in Figs. 6 and 7—verifying the above analysis derived from the surface current distributions. By increasing the length H of the L-shaped radiation strip, the lower resonant frequency of the antenna can be moved to higher

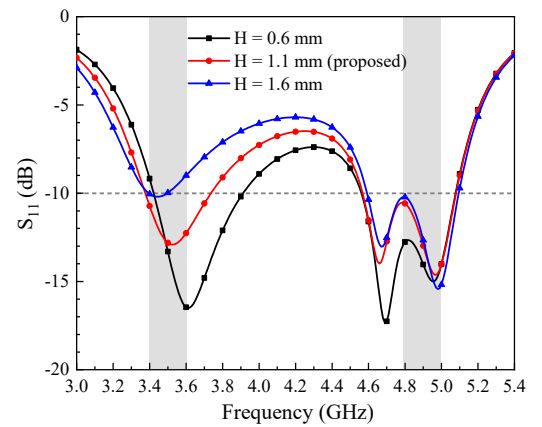


Fig. 6. Simulated S_{11} with different values of H.

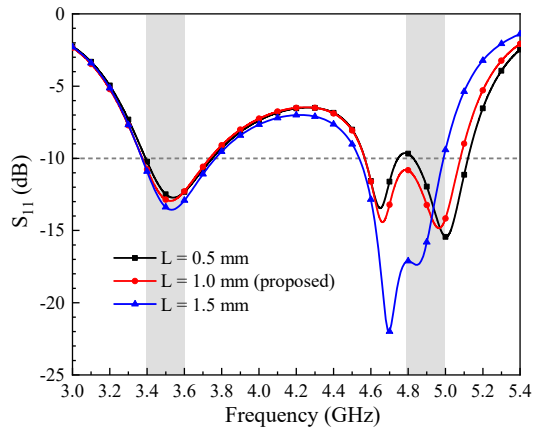


Fig. 7. Simulated S_{11} with different values of L.

frequencies. Meanwhile, when adjusting the value of L , the distribution parameters of the antenna elements will also change accordingly, effectively widening the operating band in the 4.9 GHz band. It is evident that when $L = 1.0$ mm and $H = 1.1$ mm, the desired frequency bands will be sufficiently covered.

3. Isolation Optimization

As depicted in Fig. 8, this study proposes different isolation structures—Structure 1, Structure 2, and Structure 3—to achieve better isolation performance. Compared to Structure 1, Structure 2 adds a diagonal rectangular slot, which improves antenna isolation to be more than -20 at the higher frequency band. Twenty-one circular slots are evenly distributed on both sides of the diagonal rectangular slot in Structure 3. The circular slots in the ground can improve high-frequency isolation while also broadening the bandwidth of the antenna in the higher frequency band. The slotted-dot lines broaden the -10 dB bandwidth from 4.8–5.07 GHz to 4.57–5.07 GHz, enabling the antenna to exhibit a more stable performance in the required 4.8–5.0 GHz band. The simulated S -parameters of the three isolation structures are shown in Fig. 9. Notably, the isolation of the proposed antenna is more than 22 dB in both the desired frequency bands.

4. 3D Radiation Pattern

Fig. 10 presents the 3D radiation pattern of a single antenna

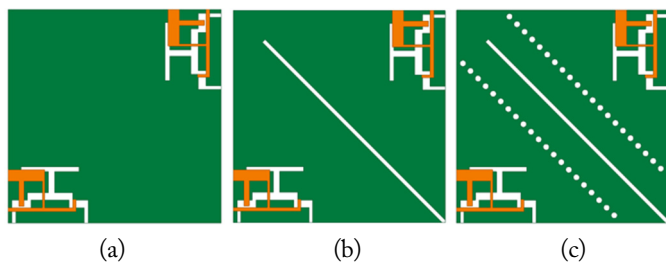


Fig. 8. Different isolation structures: (a) Structure 1, (b) Structure 2, and (c) Structure 3.

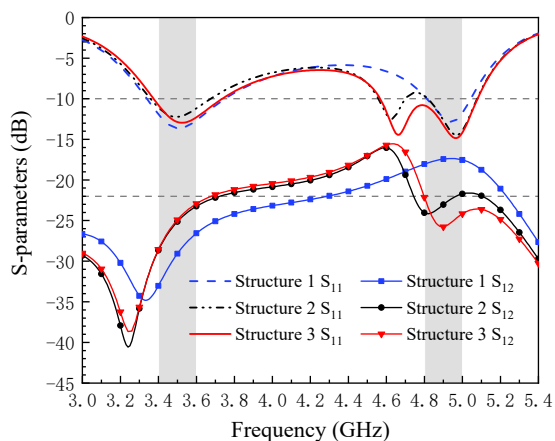


Fig. 9. Simulated S -parameters of the different isolation structures.

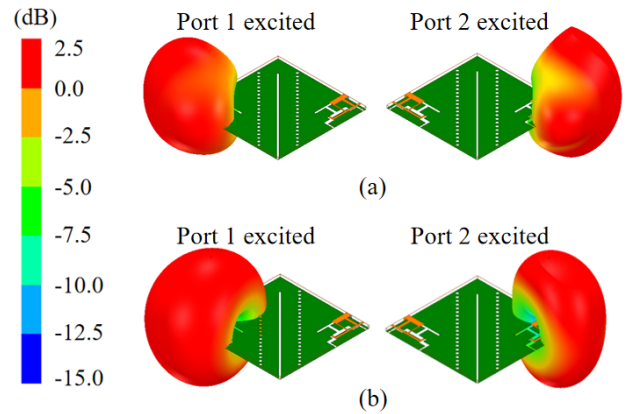


Fig. 10. The 3D radiation patterns of the single element at (a) 3.5 GHz and (b) 4.9 GHz.

element by inducing excitation at one port while keeping the other port terminated using a matching load. The simulated 3D radiation patterns show that the proposed antenna achieves a maximum gain of 1.99 dB at 3.5 GHz and 2.12 dB at 4.9 GHz.

IV. EXPERIMENTAL ANALYSIS

Following the design process, the antenna prototype was manufactured, the photograph of which is illustrated in Fig. 11. Fig. 12 shows the specific circumstances of the measured and

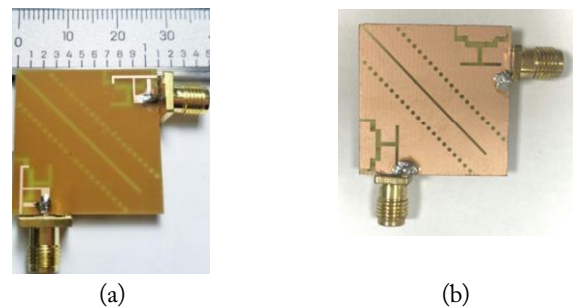


Fig. 11. Photograph of the antenna prototype: (a) top view and (b) bottom view.

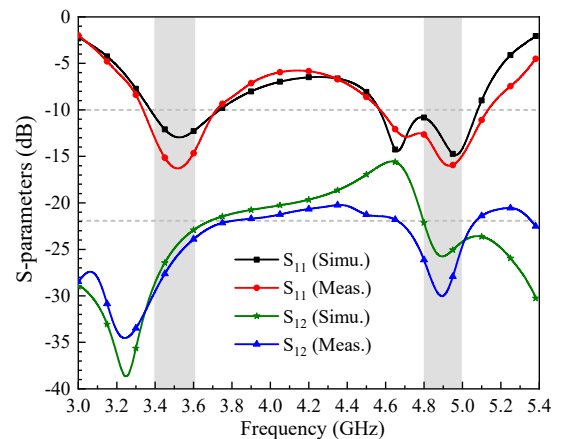


Fig. 12. Simulated and measured S -parameters of the MIMO system.

simulated S -parameters of the proposed antenna. The measured -10 dB impedance bandwidths are 380 MHz (3.34–3.72 GHz) and 560 MHz (4.57–5.13 GHz), which can sufficiently cover the 3.5 GHz (3.4–3.6 GHz) and 4.9 GHz (4.8–5 GHz) frequency bands. Furthermore, the measured and simulated isolation is also more than 23 dB and 22 dB, respectively.

The measured and simulated radiation patterns at both 3.5 GHz and 4.9 GHz are demonstrated in Fig. 13, where Port 1 is excited while Port 2 is terminated by a $50\text{-}\Omega$ matching load. The overall trend of the measured and simulated results is similar, while reasonable discrepancy is observed to be caused by the manufacturing process and proximity effect of the test setup (e.g., connectors, cables, and positioners).

Fig. 14 illustrates the simulated and measured peak gains and total radiation efficiencies. The measured peak gains at 3.5 GHz and 4.9 GHz are 2 dBi and 2.46 dBi, respectively. Meanwhile, the total efficiencies at 3.5 GHz and 4.9 GHz are 76.65% and 71.93%, respectively. The results, therefore, exhibit good consistency between the simulated and measured peak gains and

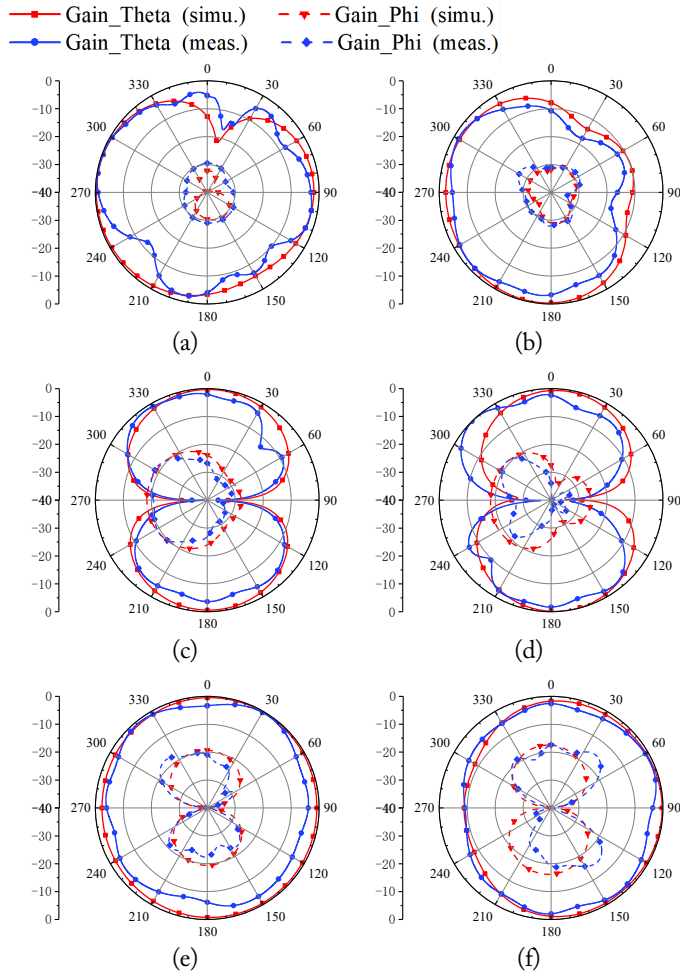


Fig. 13. Simulated and measured radiation patterns of the proposed antenna: (a) xoy plane, (c) yoz plane, (e) xoz plane at 3.5 GHz and (b) xoy plane, (d) yoz plane, (f) xoz plane at 4.9 GHz.

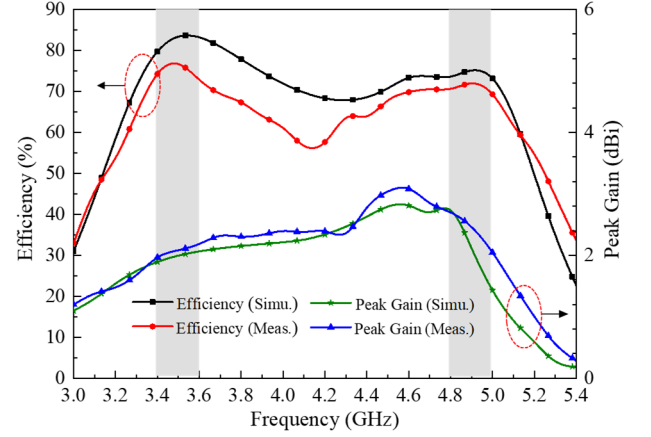


Fig. 14. Simulated and measured peak gain and total efficiencies of the proposed MIMO antenna.

total efficiencies.

To further investigate the antenna performance, the ECC is calculated according to the far-field radiation patterns—expressed by Eq. (1).

$$\rho_e = \frac{|\iint_{4\pi} [F_1(\theta, \varphi) \cdot F_2(\theta, \varphi)] d\Omega|^2}{\iint_{4\pi} |F_1(\theta, \varphi)|^2 d\Omega \iint_{4\pi} |F_2(\theta, \varphi)|^2 d\Omega} \quad (1)$$

where $F_i(\theta, \varphi)$ represents the radiation pattern when port i is excited, and Ω represents the solid angle.

The ECC calculation method using the S -parameters—a widely used process—is obtained from Eq. (2):

$$\rho_e = \frac{|S_{11}^* S'_{12} + S_{21}^* S'_{22}|^2}{(1 - |S_{11}|^2 - |S_{21}|^2)(1 - |S_{22}|^2 - |S_{12}|^2)} \quad (2)$$

where S^* represents the imaginary part of the S -parameters, while S' represents their real part.

The calculated ECC is presented in Fig. 15. Since Eq. (2) considers only the isolation between the antenna input ports and does not take the coupling between the radiation fields into account, the obtained result is not as accurate as Eq. (1). The

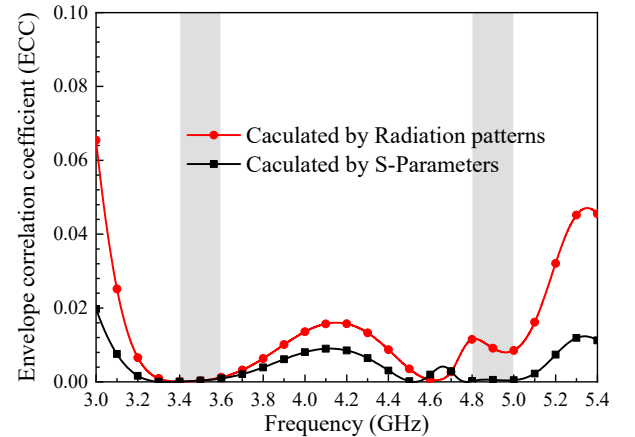


Fig. 15. Calculated ECC of the MIMO antenna system.

ECC calculated by the radiation patterns turns out to be less than 0.00125 and 0.01164 at the 3.5 GHz and 4.9 GHz bands, respectively. The calculated ECC is far smaller than the acceptable threshold of 0.3, meaning that the antenna system exhibits good diversity performance.

V. EFFECT ON USERS AND SAR INVESTIGATION

In the case of a 5G terminal antenna, it is necessary to consider the effects of the human body on the antenna. Hence, this section simulates the working conditions of the antenna on the human wrist, as shown in Fig. 16.

The simulated S_{11} values of the proposed antenna on the wrist are illustrated in Fig. 17. Although there are a few changes in the reflectance coefficients in the 3.5 GHz and 4.9 GHz bands, they still meet the requirements of the two bands. The overall trend in free space and the wrists is consistent due to the ground at the bottom. Fig. 18 shows the 3D radiation patterns of the proposed MIMO system on the wrist. The proposed MIMO antenna retains an adequate gain and a good radiation pattern.

The SAR indicates the impact of device radiation on the human body, with a low SAR value demonstrating weak absorption of radiation by the human body. Fig. 19 shows a SAR simulation of the antenna on the wrist at 3.5 GHz and 4.9 GHz. The distance between the antenna and the wrist in this

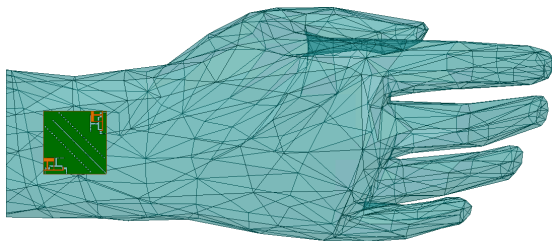


Fig. 16. The model of the proposed antenna working on the wrist.

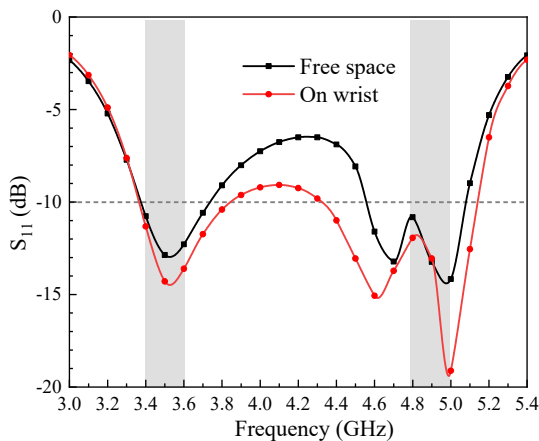


Fig. 17. Simulated S_{11} of the proposed antenna on the wrist.

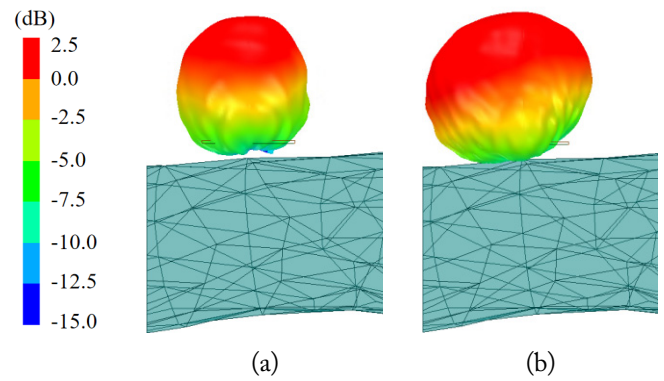


Fig. 18. The 3D radiation patterns of the proposed antenna on the wrist at (a) 3.5 GHz and (b) 4.9 GHz.

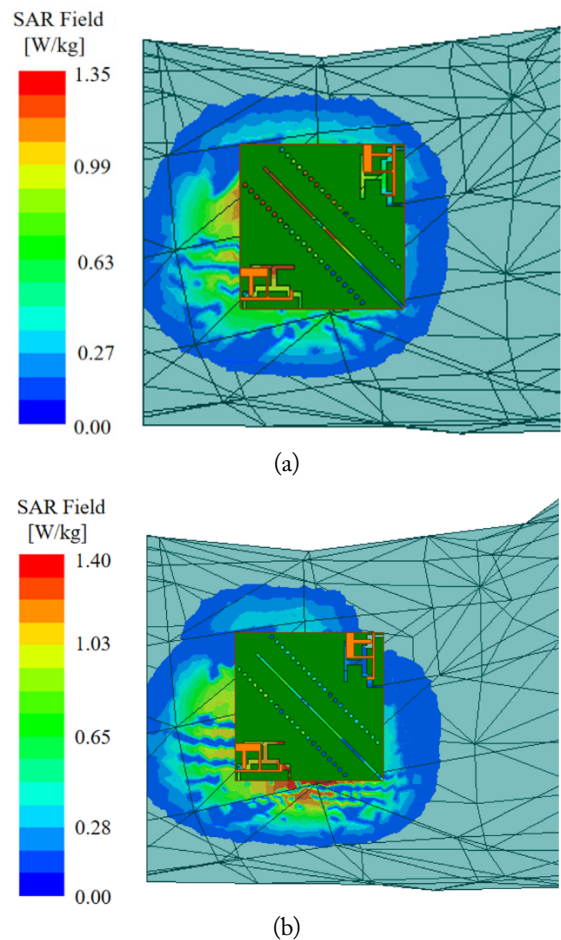


Fig. 19. Simulated SAR at (a) 3.5 GHz and (b) 4.9 GHz.

simulation is less than 4 mm. The results show that the 1 g average SAR values are less than 1.34 W/kg and 1.4 W/kg at 3.5 GHz and 4.9 GHz, respectively. Thus, the SAR level of the proposed antenna meets the standards of 1.6 W/kg per 1 g tissue in the United States.

Table 1 depicts a performance comparison of the proposed MIMO antenna and other reported antennas, highlighting the good isolation and compact structure of the former.

Table 1. Comparison of the proposed MIMO antenna and other reported antennas

Study	Operating bands (GHz)	Isolation (dB)	Peak gain (dBi)	ECC	Size
Ameen et al. [3]	3.4–3.6	−11	3.25	0.003	$0.24\lambda_0 \times 0.54\lambda_0 \times 0.019\lambda_0$ @ 3.54 GHz
	4.0–8.0	−15	3.4		
Boukarkar et al. [4]	3.471–3.529	−18.4	2.7	0.08	$0.41\lambda_0 \times 0.41\lambda_0 \times 0.04\lambda_0$ @ 3.5 GHz
	5.678–5.721	−22.7	2.85		
Wang et al. [6]	3.409–3.601	−22.3	2.45	0.005	$0.45\lambda_0 \times 0.66\lambda_0 \times 0.017\lambda_0$ @ 3.5 GHz
	4.76–5.04	−30.8	4.56		
Ren and Zhao [7]	3.4–3.6	−17.5	6.03	0.14	$1.75\lambda_0 \times 0.88\lambda_0 \times 0.009\lambda_0$ @ 3.5 GHz
	4.8–5.0	−20	8.17	0.12	
Proposed	3.34–3.72	−22	2.0	0.00125	$0.33\lambda_0 \times 0.33\lambda_0 \times 0.009\lambda_0$ @ 3.5 GHz
	4.57–5.13	−21	2.46	0.01164	

VI. CONCLUSION

A dual-band MIMO antenna operating in the 3.5 GHz band (3.4–3.6 GHz) and 4.9 GHz band (4.8–5 GHz) is presented in this study. The design evolution and dimension optimization of the single antenna element are analyzed to optimize antenna performance. The measured isolation of the antenna is observed to be more than 23 dB. The total efficiencies at 3.5 GHz and 4.9 GHz are about 76.65% and 71.93%, respectively. The results of the SAR analysis, simulated for the proposed terminal antenna, also meet the standard for terminal devices. Moreover, the measurement results are consistent with the simulation. Therefore, it can be concluded that the proposed MIMO antenna is a good candidate for use in 5G wireless communication systems.

This study was funded in part by the National Natural Science Foundation of China (No. 61671330), the Science and Technology Department of Zhejiang Province (No. LGG19F010009), and the Wenzhou Municipal Science and Technology Program (No. C20170005 and 2018ZG019).

REFERENCES

- [1] M. R. Palattella, M. Dohler, A. Grieco, G. Rizzo, J. Torsner, T. Engel, and L. Ladid, "Internet of Things in the 5G era: enablers, architecture, and business models," *IEEE Journal on Selected Areas in Communications*, vol. 34, no. 3, pp. 510–527, 2016.
- [2] M. I. Khan, M. I. Khattak, and M. M. Al-Hasan, "Miniaturized MIMO antenna with low inter-radiator transmittance and band rejection features," *Journal of Electromagnetic Engineering and Science*, vol. 21, no. 4, pp. 307–315, 2021.
- [3] M. Ameen, O. Ahmad, and R. K. Chaudhary, "Single splitting resonator loaded self-decoupled dual-polarized MIMO antenna for mid-band 5G and C-band applications," *AEU-International Journal of Electronics and Communications*, vol. 124, article no. 153336, 2020. <https://doi.org/10.1016/j.aeue.2020.153336>
- [4] A. Boukarkar, X. Q. Lin, Y. Jiang, L. Y. Nie, P. Mei, and Y. Q. Yu, "A miniaturized extremely close-spaced four-element dual-band MIMO antenna system with polarization and pattern diversity," *IEEE Antennas and Wireless Propagation Letters*, vol. 17, no. 1, pp. 134–137, 2018.
- [5] S. C. Chen, C. W. Chiang, and C. I. G. Hsu, "Compact four-element MIMO antenna system for 5G laptops," *IEEE Access*, vol. 7, pp. 186056–186064, 2019.
- [6] W. Wang, Y. Wu, W. Wang, and Y. Yang, "Isolation enhancement in dual-band monopole antenna for 5G applications," *IEEE Transactions on Circuits and Systems II: Express Briefs*, vol. 68, no. 6, pp. 1867–1871, 2021.
- [7] Z. Ren and A. Zhao, "Dual-band MIMO antenna with compact self-decoupled antenna pairs for 5G mobile applications," *IEEE Access*, vol. 7, pp. 82288–82296, 2019.
- [8] M. Li, L. Jiang, and K. L. Yeung, "A general and systematic method to design neutralization lines for isolation enhancement in MIMO antenna arrays," *IEEE Transactions on Vehicular Technology*, vol. 69, no. 6, pp. 6242–6253, 2020.
- [9] S. Wang and Z. Du, "Decoupled dual-antenna system using crossed neutralization lines for LTE/WWAN smartphone applications," *IEEE Antennas and Wireless Propagation Letters*, vol. 14, pp. 523–526, 2014.
- [10] D. Serghiou, M. Khalily, V. Singh, A. Araghi, and R. Tafazolli, "Sub-6 GHz dual-band 8×8 MIMO antenna for 5G smartphones," *IEEE Antennas and Wireless Propagation Letters*, vol. 17, no. 1, pp. 134–137, 2018.

- gation Letters*, vol. 19, no. 9, pp. 1546-1550, 2020.
- [11] P. Ramanujam, P. R. Venkatesan, C. Arumugam, and M. Ponnusamy, "Design of miniaturized super wideband printed monopole antenna operating from 0.7 to 18.5 GHz," *AEU-International Journal of Electronics and Communications*, vol. 123, article no. 153273, 2020. <https://doi.org/10.1016/j.aeue.2020.153273>
- [12] C. Y. Chiu, F. Xu, S. Shen, and R. D. Murch, "Mutual coupling reduction of rotationally symmetric multiport antennas," *IEEE Transactions on Antennas and Propagation*, vol. 66, no. 10, pp. 5013-5021, 2018.
- [13] R. Yang, S. Xi, Q. Cai, Z. Chen, X. Wang, and G. Liu, "A compact planar dual-band multiple-input and multiple-output antenna with high isolation for 5G and 4G applications," *Micromachines*, vol. 12, no. 5, article no. 544, 2021. <https://doi.org/10.3390/mi12050544>
- [14] H. Peng, R. Zhi, Q. Yang, J. Cai, Y. Wan, and G. Liu, "Design of a MIMO antenna with high gain and enhanced isolation for WLAN applications," *Electronics*, vol. 10, no. 14, article no. 1659, 2021. <https://doi.org/10.3390/electronics10141659>
- [15] W. Hu, L. Qian, S. Gao, L. H. Wen, Q. Luo, H. Xu, X. Liu, Y. Liu, and W. Wang, "Dual-band eight-element MIMO array using multi-slot decoupling technique for 5G terminals," *IEEE Access*, vol. 7, pp. 153910-153920, 2019.
- [16] M. Abdullah and S. Koziel, "A novel versatile decoupling structure and expedited inverse-model-based re-design procedure for compact single-and dual-band MIMO antennas," *IEEE Access*, vol. 9, pp. 37656-37667, 2021.
- [17] Y. Dou, Z. Chen, J. Bai, Q. Cai, and G. Liu, "Two-port CPW-fed dual-band MIMO antenna for IEEE 802.11 a/b/g applications," *International Journal of Antennas and Propagation*, vol. 2021, article no. 5575887, 2021. <https://doi.org/10.1155/2021/5572887>
- [18] S. C. Chen, L. C. Chou, C. I. Hsu, and S. M. Li, "Compact sub-6-GHz four-element MIMO slot antenna system for 5G tablet devices," *IEEE Access*, vol. 8, pp. 154652-154662, 2020.
- [19] R. Mark, N. Rajak, K. Mandal, and S. Das, "Metamaterial based superstrate towards the isolation and gain enhancement of MIMO antenna for WLAN application," *AEU-International Journal of Electronics and Communications*, vol. 100, pp. 144-152, 2019.
- [20] F. Liu, J. Guo, L. Zhao, G. L. Huang, Y. Li, and Y. Yin, "Dual-band metasurface-based decoupling method for two closely packed dual-band antennas," *IEEE Transactions on Antennas and Propagation*, vol. 68, no. 1, pp. 552-557, 2020.
- [21] K. S. Parvathi and S. R. Gupta, "Novel dual-band EBG structure to reduce mutual coupling of air gap based MIMO antenna for 5G application," *AEU-International Journal of Electronics and Communications*, vol. 138, article no. 153902, 2021. <https://doi.org/10.1016/j.aeue.2021.153902>
- [22] J. P. Shinde and P. N. Shinde, "M-shape electromagnetic-bandgap structures for enhancement in antenna performance," *AEU-International Journal of Electronics and Communications*, vol. 70, no. 6, pp. 842-849, 2016.
- [23] P. P. Bhavarthe, S. S. Rathod, and K. T. V. Reddy, "A compact dual band gap electromagnetic band gap structure," *IEEE Transactions on Antennas and Propagation*, vol. 67, no. 1, pp. 596-600, 2019.

Guiting Dong

was born in Sichuan, China, in 1997. She received her B.S. degree in Electrical Engineering from Shanghai University of Electric Power in 2019. She is currently pursuing her M.S. degree at Wenzhou University. Her research interests include multiband antennas, MIMO technologies, and RFIC design.

Zhi-Zhou Chen

received his B.S. degree in Integrated Circuit Design and Integration System from Hangzhou Dianzi University, Hangzhou, China, in 2010, and his M.S. and Ph.D. degrees in Circuits and Systems from Shanghai Institute of Technical Physics, Chinese Academy of Sciences, in 2015 and 2017, respectively. Since 2017, he has been a lecturer at the College of Electrical and Electronic Engineering at Wenzhou

University. His research interests include antenna design and photoelectric sensing methods and systems.

Jianlin Huang

was born in Zhejiang, China, in 1995. He received his B.S. degree in Electrical Engineering from Wenzhou University in 2018. He is currently pursuing his M.S. degree at Wenzhou University. His research interests include antenna and RFIC design.

Gui Liu

was born in Wenzhou, Zhejiang, China, in 1975. He received his B.S. degree in Communication Engineering from South China University of Technology, Guangdong, China, in 1997, and his M.S. degree in Electrical Engineering from Sun Yat-Sen University, Guangdong, China, in 2003. In 2011, he received his Ph.D. degree in Electrical Engineering from the Illinois Institute of Technology, Chicago,

IL, USA. Since September 2011, he has been a professor at Wenzhou University in China. He is currently a full professor and Oujian Distinguished Professor at the College of Electrical and Electronic Engineering at Wenzhou University. His research interests include antennas, millimeter-wave on-chip passive components, and RFIC design. He serves as an active reviewer for numerous IEEE, Elsevier, IOP Science, and other international journals.

Simin Lin

was born in Fujian, China, in 2001. She is currently pursuing her B.S. degree at Wenzhou University. Her research interests include multiband antenna and MIMO antenna design.

Instructions for Authors

Journal of Electromagnetic Engineering and Science (J. Electromagn. Eng. Sci.; JEES) is an official English journal of the Korean Institute of Electromagnetic and Engineering Science (KIEES). The objective of *JEES* is to publish academic as well as industrial research results and findings on electromagnetic engineering and science. The journal covers all aspects of researches and technology related to electromagnetics: Electromagnetic Compatibility/Electromagnetic Interference, Microwave and Millimeter-Wave Engineering, Antenna and Propagation, Electromagnetic Theory, Wireless Communication, Lightwave and Electro-Optics, Materials and Components, Software Defined Radar, Radar, Bioelectromagnetics, and etc.

I. Copyright and Creative Commons Attribution Licensing

The copyright and the transfer rights of the digital content of published papers and the journal is owned by the KIEES. All published materials are also assigned a Creative Commons Attribution License (<http://creativecommons.org/licenses/by-nc/4.0/>). The journal accepts manuscripts for consideration with the understanding that the manuscript has not been published previously and is not currently under consideration for publication elsewhere, and in addition, that the authors (or their employer, if it holds the copyright) are authorizing the transfer of the copyright to the Institute when the manuscript is submitted. Author should check the copyright transfer conditions and forms at <http://www.jees.kr>.

II. Research and Publication Ethics

Research published in *JEES* must have followed institutional, national, and international guidelines. For policies on research and publication ethics that are not stated in these instructions, please refer to the *Committee on Publication Ethics (COPE) Guidelines* (<http://publicationethics.org/resources/code-conduct>).

1. Originality and Duplicate Publication

A manuscript submitted for publication in *JEES* should be an original work with technical values. It must not have been previously published and is not under consideration for publication elsewhere. *JEES* assumes that the materials submitted for its publications are properly available for general dissemination for the readership of those publications. It is the responsibility of the authors, not *JEES*, to determine whether disclosure of their materials requires prior consent of other parties and, if so, to obtain it. If an author uses charts, photographs, or other graphics from any previously printed materials, he/she is responsible for obtaining written permissions from the publisher to use them in his/her manuscript. Responsibility for the contents of published papers rests upon the authors, not *JEES*.

2. Conflict of Interest

Authors are required to complete a declaration of conflict of interests. All conflict of interests that are declared will be listed at the end of published articles.

3. Authorship

Authorship should be restricted to those individuals who have met each of the following three criteria:

1) made a significant contribution to the conception and design of the project, or the analysis and interpretation of the data, or other substantial scholarly effort; 2) participated in drafting, reviewing and/or revising the work; and 3) approved the final version for publication. After the initial submission of a manuscript, any changes whatsoever in authorship (adding author(s), deleting author(s), or re-arranging the order of authors) must be explained by a letter to the editor from the authors concerned. The content of this

letter must be acknowledged and agreed upon by all of the authors of the paper.

If you accept the policies on research and publication issued by KIEES, authors must click the response of “The Code of Research Ethics” through online.

III. Submission of Manuscripts

Authors are expected to be members of the KIEES except for some special cases approved by the Editorial Board of KIEES. All manuscripts should be submitted electronically through the online submission and review site (<https://mc03.manuscriptcentral.com/jees>). For the first submission, you may be required to create an account on the submission site. A manuscript can be submitted at any time of the year. When submitting a manuscript, authors need to make sure that their manuscripts do not provide any of their identities such as authors' names and affiliations as the review is double-blinded. More detailed submission instruction is available in the upper right corner of the submission site. All manuscripts submitted to the Journal must comply with the instruction and the standard format of the Journal. Otherwise, it will result in return of the manuscript and possible delay in publication. For assistance, please contact us via e-mail (admin-jees@kiees.or.kr).

IV. Peer Review Process

The manuscript will be forwarded to three reviewers selected for their expertise in the field of the submitted manuscript. The acceptance criteria for all papers are based on the quality and originality of the research and its clinical and scientific significance. During the review process, the author is often asked to expand, rewrite, or clearly explain the specific contents of his/her paper. It is not uncommon that an author is asked to provide another draft with the suggested changes for further review. A revised manuscript should be submitted to the homepage within a month from the date on which any change of the manuscript is requested to the author. Once a manuscript has received the final approval of the reviewers and Editor-in-Chief, the author will be notified and asked to prepare the manuscript for final publication and to possibly complete an additional information form.

V. Publication Type

The papers are classified into five categories.

Regular Paper should be an original work that contributes to the academic interests of the KIEES members with technical values. The paper should also be written within 12 pages with A4 size including figures, charts, and tables (The main body of text consists of two columns).

Letter consists of reports of preliminary results or short reports on completed work that are of current interest to many researchers in the field. Comments on material previously published in the journal, suggestions for new directions, and errata could be included. Their length must be less than 3 pages (with a two-column format) including paper title, author affiliation, reference, etc.

Review Paper will be published by direct submission as well as from invited experts. In both cases, the work will be subject to editorial review. Review papers should critically review topics not only to inform the reader of the background, but also to communicate the state of the art and outstanding research problems.

Technical Report is on innovative technical achievements of interest to the community and usually a report of an extensive series of measurements. Report is often involving display in the form of tables or graphs, with text describing the conditions and procedures of measurement.

Editorial is a brief report of research findings adequate for the journal's scope and of particular interest to the community.

VI. Manuscript Preparation

All manuscripts must be written in MS-Word and adhere to the following guidelines:

1. A cover of each paper manuscript should include a title, authors' names (main author and co-authors), author's organizations, contact information (e-mail and phone number), and the author's area of expertise.

2. The first page of a main text should only contain title, abstract with a length of about 150 words, and key words with around five words.
3. The contents of the manuscript should be arranged in the order of abstract, main text, acknowledgments, references, and appendix.
4. The numbers corresponding to chapters in the manuscript should be written in Roman numerals (I, II, III, IV...) and the numbers corresponding to sections should be written in Arabic numerals (1, 2, 3, 4...).
5. Equation numbers should be given in Arabic numerals enclosed in parentheses on the right-hand margin. They should be cited in the text as, for example Eq. (1) or Eqs. (1)-(3).
6. All tables should be numbered consecutively with Arabic numerals. They should be referred to in the text and should be numbered according to their order of mention in the text. In addition, all tables should, not only list all abbreviations in the table in footnotes at the end, but also have a title that is concise and describes the table's contents. Vertical lines are not used. The table should be self-explanatory and supplement, not duplicate, the text. If the table or any data therein have been published, a footnote to the table must give permission information to the original source. The structure should be clear, with simple column headings giving all units. A table should not exceed one page when printed. Use lowercase letters in superscripts ^{a,b,c...} for special remarks.
7. All figures should be of high quality meeting with the publishing requirement with legible symbols and legends. In preparing the figures, authors should consider a size reduction during the printing process to have acceptable line clarity and character sizes. Use only figures that are necessary to illustrate the meaning of the text. Figures must be black and white of high contrast. All figures should be referred to in the text as, for example, Fig. 1, Fig. 2(a), or Figs. 1-3.
8. Only those references cited in the text should be listed in the references. Authors are responsible for the accuracy and completeness of their references and the correct text citations. In the text the reference should be numbered in bracket in ascending order (e.g., [1, 3], or [4-6]; Lee [2] and Kim and Park [5]; Jang et al. [7]). In case of the paper title, only the first letter is to be capitalized. However, in case of journal and book titles, the first letter of each word should be capitalized and all of the letters should be italicized. See the example below.

Books

- [1] F. Giannini and G. Leuzzi, *Nonlinear Microwave Circuit Design*. NewYork, NY: John Wiley & Sons Inc., 2004.

Journals

- [2] H. Ahn and B. Kim, "Equivalent transmission-line sections for very high impedances and their application to branch-line hybrids with very weak coupling power," *Journal of Electromagnetic Engineering and Science*, vol. 9, no. 2, pp. 85-97, 2009.

Report

- [3] E. E. Reber, R. L. Michell, and C. J. Carter, "Oxygen absorption in the earth's atmosphere," Aerospace Corp., Los Angeles, CA, Tech. Rep. TR-0200 (4230-46)-3, Nov. 1988.

Conference Proceedings

- [4] S. P. Bingulac, "On the compatibility of adaptive controllers," in *Proceedings of the 4th Annual Allerton Conference on Circuit and System Theory*, NewYork, pp. 8-16, 1994.

Papers Presented at Conferences

- [5] J. G. Kreifeldt, "An analysis of surface-detected EMG as an amplitude-modulated noise," presented at the 8th International Conference on Medical and Biological Engineering, Chicago, IL, 1969.
- [6] J. Arrillaga and B. Giessner, "Limitation of short-circuit levels by means of HVDC links," presented at the IEEE Summer Power Meeting, Los Angeles, CA, Jul. 1990.

Theses (M.S.) and Dissertations (Ph.D.)

- [7] N. Kawasaki, "Parametric study of thermal and chemical nonequilibrium nozzle flow," M.S. thesis, Department of Electronic Engineering, Osaka University, Osaka, Japan, 1993.

[8] J. O. Williams, "Narrow-band analyzer," Ph.D. dissertation, Department of Electronic Engineering, Harvard University, Cambridge, MA, 1993.

Standards

[9] *IEEE Criteria for Class IE Electric Systems*, IEEE Standard 308, 1969.

Online Sources

[10] R. Bartle, "Early MUD History," Nov. 1990; www.ludd.luth.se/aber/mud-history.html.

9. When citing any paper published in JEES, it should be indicated the name of the journal as *Journal of Electromagnetic Engineering and Science* or *J. Electromagn. Eng. Sci.*

10. Acknowledgment, if needed, appears before the reference. Sponsorship or financial support acknowledgment should be included here.

11. Unit and Abbreviation: If the authors describe length, height, weight, and volume, they should use standard metric units. Temperature should be given in degrees Celsius. All other units should follow the International System of Units (SI). All units must be preceded by one space except percentages (%) and temperatures (°C).

Abbreviations must be used as an aid to the reader, rather than as a convenience of the author, and therefore their use should be limited. Generally, abbreviations that are used less than 3 times in the text, including tables and figure legends, should be avoided. Standard SI abbreviations are recommended. Other common abbreviations are as follows (the same abbreviations are used for plural forms): h (hour), min (minute), s (second), d (day), wk (week), mo (month), y (year), L (liter), mL (milliliter), μ L (microliter), g (gram), kg (kilogram), mg (milligram), μ g (microgram), ng (nanogram), pg (picogram), *g* (gravity; not g), nm (nanometer), μ m (micrometer), mV (millivolt), mA (milliampere), mW (milliwatt), C (coulomb), μ F (microfarad), mH (millihenry), n (samplesize), SD (standard deviation of the mean), and SE (standard error of the mean).

VII. Accepted Manuscript

Once the review process has been completed with a decision of acceptance, the final manuscript accommodating all of the reviewers' comments should be submitted along with photos of the authors and their brief biographies (including major research areas). The accepted papers will be published, in principle, in the order of initially submitted dates subject to decision of the Editorial Board.

1. Page Proofs

Authors will be given an opportunity to review the laser printed version of their manuscripts before printing. One set of page proofs in PDF format will be sent by e-mail to the corresponding author. The review should be solely dedicated to detecting typographical errors.

2. Publishing Charge

The publishing charge for general publishing is KRW 450,000 (USD 450) for up to the first 6 pages. For 7 to 8 pages, an extra charge of KRW 120,000 (USD 120) per page is applied. For 9 pages or more, an extra charge of KRW 160,000 (USD 160) per page is applied. Twenty reprints without a cover will be supplied without an additional charge. With a corresponding author who is non-member of the KIEES, an additional charge of KRW 100,000 (USD 100) will be applied to the total charge. The guidance of the KIEES membership enrollment can be found in the link below.

(<https://www.kiees.or.kr/html/?pmode=MemberInfo#>)

Contact Us

Editorial office of the Korean Institute of Electromagnetic Engineering and Science

217, Saechang-ro, Yongsan-gu, Seoul, 04376, Korea

Tel: +82-2-337-9666/332-9665 Fax: +82-2-6390-7550

<http://www.jees.kr>, E-mail: admin-jees@kiees.or.kr

AUTHOR CHECKLIST

Title : _____

General

- This paper has not been and will not be published in any other journal.
- This paper follows the format of the KIEES paper submission guideline, is less than 12 pages long, including figures and tables (3 pages for a letter), and has a two-column layout.
- This paper includes a cover page, an abstract, keywords, main text, appendix, and references in the correct order. Each page has a consecutive page number.

Cover page

- The cover page includes the title, authors, affiliation of all authors, identifier of the corresponding author, and provides contact information for the corresponding author (phone number, e-mail address, and mobile number).

Abstract and key words

- An abstract is provided and is less than 500 words long.
- Fewer than 5 keywords are provided.

Main text

- The reference number is written next to the quote.
- The chapter numbers are written in Roman numerals (I, II, III, IV...) and subheading numbers are written in Arabic numerals (1, 2, 3, 4...).

References

- Sufficient Korean as well as international literature is referenced in the paper.
- Only the references used in the main text are included in the reference list and these are numbered according to their order of appearance.
- All reference citations follow the correct format indicated in the submission regulations.

Figures and tables

- For the figures and tables, the first letter of the very first word is capitalized.
- All figure legends include both a title and a detailed explanation to help in understanding what the figure depicts.
- All tables are self-explanatory and do not repeat the content from figures or sources included in the main text.

* Check each box after confirming that the statement is true.

The authors of this paper have confirmed the above items, following the paper submission regulations of *the Korean Institute of Electromagnetic Engineering and Science (KIEES)*, and are requesting publication of this paper.

_____ / _____ / 2022

Representative author: _____ (signature)

Journal of Electromagnetic Engineering and Science

<http://www.jees.kr>

JEES
Volume 22, Number 5,
September, 2022

REGULAR PAPERS

- Conical Ground Helical Antenna with Feed-Through Insulator for High-Power Microwave Applications
Seung Hun Cha · Jin Soo Choi · Jiheon Ryu · Hae-ok Kwon · Sang-min Lee · Dong-Hee Son · Young Joong Yoon ----- 537
- Development of a Numerical Tablet Model in WLAN Band for SAR Study
Jisu Lee · Ae-Kyoung Lee · Seon-Eui Hong · Hyung-Do Choi · Kyung-Young Jung ----- 544
- A Wideband Doherty Combiner with Phase Variation Compensation Using LTCC Applicable for High Power Transmission
Youna Jang · Kwanhun Jeong · Jiwon Kim · Daeung Lee · Dal Ahn ----- 550
- Free-Space Unknown Thru Measurement Using Planar Offset Short for Material Characterization
Jin-Seob Kang ----- 555
- Reduced-Size Series-Fed Two-Dipole Endfire Antenna
Heesu Wang · Yong Bae Park · Ikmo Park ----- 563
- Omega-K Algorithm Using Plane Wave Approximation for Forward-Looking Imaging Radar
Byunglae Cho · Sungwon Hong · Kichul Yoon ----- 571
- A Neural Network-Based Microwave Imaging Method for Object Localization
Wonhyung Son · Won-Kwang Park · Seong-Ho Son ----- 576
- Spatial Delay Line Canceler-Based Sidelobe Blanking for Low Radar-Cross-Section Target
Youn-Hui Jang · Donghyeon Cho ----- 580
- GPR Image Recovery Effect on Faster R-CNN-Based Buried Target Detection
Deniz Kumlu ----- 591
- A Compact Dual-Band MIMO Antenna for Sub-6 GHz 5G Terminals
Guiting Dong · Jianlin Huang · Simin Lin · Zhizhou Chen · Gui Liu ----- 599